



Overview of carbon nanostructures and nanocomposites for electromagnetic wave shielding

Chao Wang^{a, b, c, *, 1}, Vignesh Murugadoss^{c, d, 1}, Jie Kong^{e, **}, Zhenfeng He^{a, f},
Xianmin Mai^{g, ***}, Qian Shao^h, Yanjun Chen^{a, b}, Li Guo^a, Chuntai Liuⁱ,
Subramania Angaiah^{d, ****}, Zhanhu Guo^{c, *****}

^a Advanced Energy Materials and Systems Institute, North University of China, Taiyuan 030051, China

^b College of Materials Science and Engineering, North University of China, Taiyuan 030051, China

^c Integrated Composites Laboratory (ICL), Department of Chemical and Biomolecular Engineering, University of Tennessee, Knoxville, TN 37996, USA

^d Electrochemical Energy Research Lab, Centre for Nanoscience and Technology, Pondicherry University, Puducherry, 605 014, India

^e MOE Key Laboratory of Space Applied Physics and Chemistry, School of Science, Northwestern Polytechnical University, Xi'an, 710072, China

^f School of Chemical Engineering and Technology, North University of China, Taiyuan, 030051, China

^g School of Urban Planning and Architecture, Southwest Minzu University, Chengdu, 610041, China

^h College of Chemical and Environmental Engineering, Shandong University of Science and Technology, Qingdao, 266590, China

ⁱ Key Laboratory of Materials Processing and Mold (Zhengzhou University), Ministry of Education; National Engineering Research Center for Advanced Polymer Processing Technology, Zhengzhou University, Zhengzhou, 450002, China

ARTICLE INFO

Article history:

Received 9 July 2018

Received in revised form

25 August 2018

Accepted 1 September 2018

Available online 7 September 2018

Keywords:

Carbon nanostructures

Electromagnetic interference shielding

Carbon nanocomposites

Multi-layer structures

3D architectures

Lightweight materials

ABSTRACT

Based on the contributions of carbon nanostructures and their composited species, great advances in electromagnetic wave interference shielding have been achieved. In this article, recent progress in electromagnetic wave shielding enabled by the synergism of carbon nanostructures and their corresponding composites is discussed encompassing the factors of microstructural defects, filler concentration, filler alignment, filler inherent conductivity and the surrounding temperature. Carbon nanostructures and their composites would energize the advanced electromagnetic wave shielding because of their light weight, high corrosion resistance, excellent thermal, mechanical, and electrical properties, broad absorption frequency bandwidth and cost-effectiveness. In this context of identifying suitable carbon composites that can enhance electromagnetic wave absorption. This review provides updated electromagnetic wave shielding knowledge of carbon nanostructures and their composites as well as their prospects and challenges.

© 2018 Elsevier Ltd. All rights reserved.

Contents

1. Introduction	697
2. Preparation of carbon nanostructures and their nanocomposites	699
3. Concept of electromagnetic interference (EMI) and shielding	702
3.1. Shielding effectiveness (SE)	705
3.2. Experimental evaluation of EMI shielding property	706
3.3. Design consideration for EMI shielding materials	707

* Corresponding author. Advanced Energy Materials and Systems Institute, North University of China, Taiyuan 030051, China.

** Corresponding author.

*** Corresponding author.

**** Corresponding author.

***** Corresponding author.

E-mail addresses: wangchao_nuc@126.com (C. Wang), kongjie@nwpu.edu.cn (J. Kong), maixianmin@foxmail.com (X. Mai), asubramania@gmail.com (S. Angaiah), zguo10@utk.edu (Z. Guo).

¹ These two authors contributed equally and should be treated as the co-first authors.

3.4.	Microwave absorption property of EMI shielding material	707
3.4.1.	Impedance matching conditions	707
3.5.	Dielectric properties	708
3.6.	Magnetic properties	709
3.7.	Skin depth	709
4.	Electronic transport properties of carbon nanostructures	709
5.	Pristine carbon nanostructures as EMI shielding materials	710
5.1.	Three-dimensional architecture of carbon materials	712
6.	Temperature-dependent EMI performance of carbon nanostructures	714
7.	Nanostructured carbon composites	716
7.1.	Carbon/magnetic material nanostructures	716
7.2.	Carbon/Metal oxide nanostructures	720
7.3.	Carbon/metal chalcogenide (MC) nanostructures	721
8.	Carbon-based multi-layered nanostructures	723
9.	Carbon-based multicomponent nanostructures	725
10.	Conclusion and perspective	727
	Acknowledgments	728
	References	728

1. Introduction

The electromagnetic interference (EMI) affects almost entire electrical and electronic systems from everyday life, military activities to space exploration. There have been many aspects such as proliferation of electronic equipment, miniaturization of electronic systems and their components, development in interconnection technology, electronic discharge due to the obliteration of microchips during handling, need for secure data, protection of military equipment from electromagnetic pulse (EMP), potential health risk to human beings, etc. that proliferate the concerns about EMI [1]. Electromagnetic compatibility (EMC) is the ability of electrical and electronic equipment and systems to operate in the recommended electromagnetic wave environment, without detrimental deterioration in their performance due to EMI. EMC can be achieved by attenuating EMI and protecting the systems and equipment from the exposure of electromagnetic radiation. EMC addresses the reduction of EMI by the following ways; (i) reducing the EM wave generation at its source, (ii) reducing or elimination coupling paths by proper layout, (iii) shielding, (iv) designing hardware with an intrinsic protection to EMI, and (v) developing software with a high level of resistance to EMI. Among these approaches, EMI shielding is an important and effective method in EMC design [2]. For this reason, intense efforts have been made to develop materials with enhanced EMI shielding effectiveness (SE) to prevent such undesirable effects.

The history of EMI shielding dated back to as early as the 1830s when Faraday discovered Faraday cage, an enclosed conductive housing with zero electrical fields. In the 20th century, metals and metal coated lightweight materials such as plastics obtained by electroless plating, electroplating or vacuum deposition are most commonly used for achieving Faraday cage effect, in which shielding is mainly realized by reflection. However, the metal has no effect on electromagnetic wave shielding. Mu-metal (a nickel-iron soft ferromagnetic alloy) with high magnetic permeability is used to shield magnetic field [3]. In spite of high EMI effect, metals suffer from heavyweight, poor wear and scratch resistance, prone oxidation and demand of surface modification and additional equipment [4]. In fact, their good SE is mostly reflection dominant, which is undesirable due to the potential secondary pollution. Recently, the absorption mechanism dominant EM materials will normally convert the absorbed EM waves to thermal energy, which have drawn increasing attention. The desirable EM shielding

materials are strong absorption, broadband width of operation, less thickness, flexibility, high dimensional and thermal stability, easy processability, low cost and long cycle (Fig. 1).

Traditional microwave absorbing materials, such as ferrites, magnetic metals, intrinsically conducting polymers, etc. cannot meet the absorption demand due to high density and narrow bandwidth. Magnetic materials have shortcoming due to their high density and decreased absorption efficiency in GHz range and beyond [5], whereas intrinsically conducting polymers suffer from lack of environmental stability and poor processing [6–8]. Thus, there exists a quest for lightweight and highly efficient materials for EMI shielding applications. Recently, carbon-based materials gained good popularity for their unique properties such as lightweight, processing benefits, flexibility, resistance to corrosion, extraordinary electrical, mechanical and thermal properties in various fields [9–12]. Carbon materials for EMI shielding mainly include carbon black (CB), carbon fibers (CF), carbon nanotubes (CNT), flexible graphite, graphene nanosheets, graphene oxide (GO) and reduced graphene oxide (RGO) [13–19]. Fig. 2 demonstrates the potential of different carbon nanostructures and their composites in EMI shielding applications.

The history of carbon materials in EMI shielding research dated back to 1936 when Naamlooze Vennootschap Machinerieen reported quarter wave resonant absorber for the 2 GHz region containing CB and TiO₂ [20]. Fig. 3 shows the timeline for the use of carbon materials for EMI applications. During World War II, camouflaging of submarine snorkels and periscopes have been achieved by absorbers containing CB. Materials known as “HARP” (Halpern-anti-radar-paint) containing CB and Al flakes filled rubber resulted from U.S. project Halpern in the period 1941–1945, which exhibited an absorption of 15–20 decibel (dB) at the X-band [21]. Graphite and CB are widely used as absorber until the invention of carbon nanotubes in the 1990s [22–24]. The metallic CNT may exhibit low-frequency plasmons, which differ from that of π -plasmon and thus pave the way for new type of EMI shielding materials [25,26]. Since 2010, graphene has been used as emerging EMI shielding materials [27–29].

With the advancement of science and technology, researchers and scientists can find new hybrids or composites that meet existing requirements while taking into account of the disadvantages facing the metallic shielding materials. All features of EMI shielding cannot be solved by a single material. Carbon materials can be used as both conductive fillers for insulating matrices such

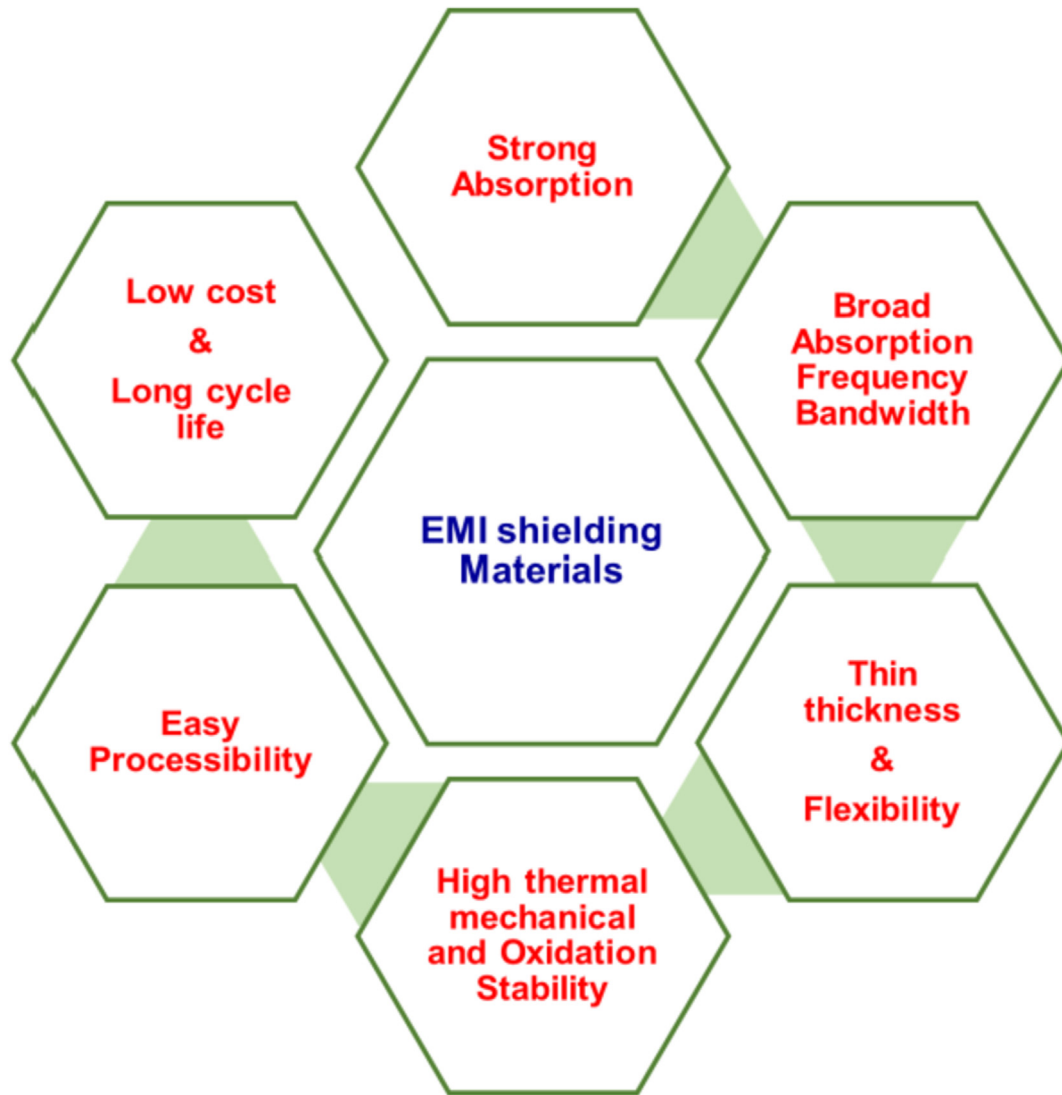


Fig. 1. Desired properties of ideal EMI shielding materials. (A colour version of this figure can be viewed online.)

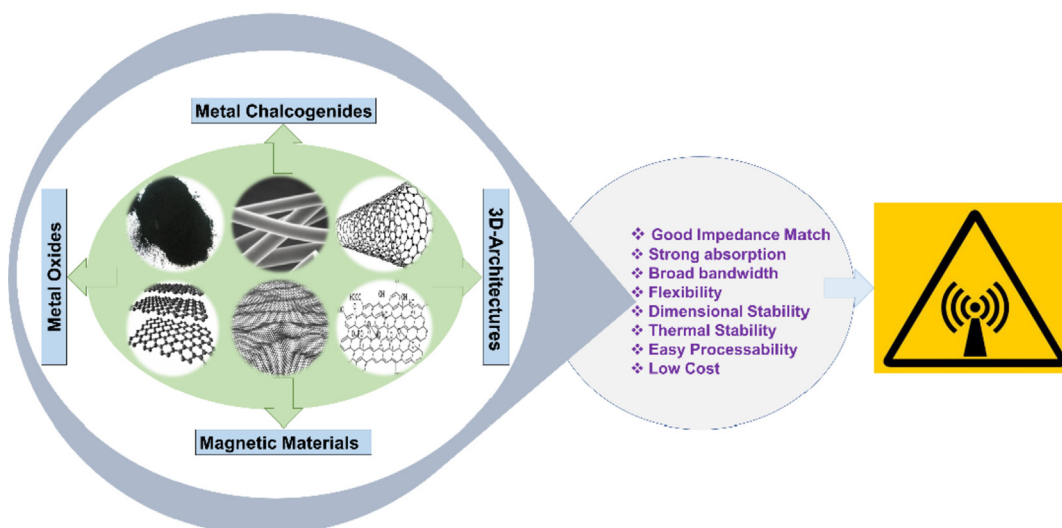


Fig. 2. Demonstration of efficacy of carbon-based nanostructures for EMI shielding applications. (A colour version of this figure can be viewed online.)

as polymers and ceramics as well as an electrically conducting matrix for additives such as conducting materials, dielectric material, and magnetic materials. The ability to form different architectures on nanoscale makes carbon as a versatile and unique element.

Owing to these benefits, a rapidly increasing trend for using carbon-based nanostructures in EMI research has emerged. Fig. 4 shows the number of publications on EMI shielding and carbon materials for EMI shielding. The number of publications on carbon materials for electromagnetic interference shielding exceeds nearly half the number of publications on electromagnetic interference shielding in the last five years from 2010, implying the importance of carbon materials as a potential candidate for EMI shielding applications.

In consideration of these new developments, to provide the scientific community with a critical assessment and a critical vision on the carbon-based materials and their applications for EMI shielding is timely need. So far, most of the reviews outlined the EMI shielding performance of polymers incorporated with the carbon materials and single carbon nanostructures such as graphene [30–34]. This review article focuses on the most advanced carbon nanostructures such as three dimensional systems, multi-layer nanostructures and their nanostructured composites as emerging EMI shielding materials. We summarize the effects of the morphology, functionalization and the ratio between the components in the nanostructured carbon composites on the dielectric, magnetic and EMI shielding properties along with the corresponding EMI shielding mechanisms. The advantages and limitations of various carbon nanostructures and their nanostructured composites along with the strategies that are reported to overcome these limitations and tune the EMI shielding properties are presented. In the following sections, we will follow the brief outline to present the synthesis of carbon nanostructures and their composites and basic theory to EMI shielding and discuss both design consideration and fundamental properties in the context of EMI shielding applications. We then focus on recent advances in the carbon nanostructures and their composites and a new concept of self-tunable EMI materials using carbon nanostructures. Finally, the challenges and perspective in the EMI shielding materials and design are outlined.

2. Preparation of carbon nanostructures and their nanocomposites

Various synthesis methods have been used for the preparation of carbon nanostructures and their composites. Both single-walled carbon nanotube (SWCNT) and multi-walled carbon nanotube (MWCNT) can be prepared by arc discharge of graphite rods [35–37], laser vaporization of graphite under inert atmosphere [38], electrolysis of graphite rods in molten salt under inert

atmosphere [39], pyrolysis (also known as chemical vapor deposition (CVD)) of hydrocarbons such as acetylene, benzene, naphthalene, methane, organic compounds (poly-furfuryl-alcohol, polyacrylonitrile), etc. using metals such as cobalt, nickel, iron, platinum and palladium as catalysts [40], solar energy based production of CNT which includes direct vaporization of carbon and metal catalyst mixture in the inert atmosphere with solar flux obtained by concentrating the solar energy [41] or producing high temperature using solar furnace [42], etc. Commercially available CNT are normally synthesized using CVD.

Similar to CNT, several methods have been used to prepare graphene. All the preparation methods are broadly divided into top-down methods, including micromechanical exfoliation [43,44], ultrasonic exfoliation [45], microwave exfoliation [46], chemical reduction of exfoliated GO [47] and arc discharge [48], and bottom-up methods, including CVD [49] and organic synthesis (e.g. acetylene coupling, alkyne-metathesis reaction, cyclohydrogenation) [50]. Other techniques such as CNT unzipping and thermal decomposition of SiC growth have also been used to obtain graphene [51]. Brodie et al. [52] reported the preparation of GO at first, by treating graphite with a strong acid (nitric acid) and oxidation agent (KClO₃). Later Staudenmaier et al. [53] and Schniepp et al. [54] reported an improved method by using sulfuric acid and nitric acid as solvents. The most popular method was reported by Hummer et al. [55] (known as Hummers method), in which sodium nitrate, concentrated sulfuric acid, potassium permanganate (oxidizing agent), 30% hydrogen peroxide were used to obtain GO. Fig. 5 elucidates the exfoliation of graphite to obtain graphene nanosheets (GN), GO and RGO [56].

In addition, carbon materials with other morphologies such as nano-onion like micro-coiled carbon structures prepared by annealing of nano-diamond powders in vacuum at high temperature [59], CVD [60] and arc discharge method [61] have been reported for EMI shielding applications. For example, Bi et al. reported that Ni nanoparticle film coated carbon microcoils by electroless plating and demonstrated that the dielectric loss tangent ($\tan \delta_E$) and magnetic loss tangent ($\tan \delta_M$) can be controlled by depositing a film of nickel nanoparticles on the microcoil surfaces [62]. Fig. 6 shows the SEM images of the carbon micro coils and nickel coated carbon micro coils. It can be seen that carbon micro coils have 3-dimensional helical structure. The unique intricate helical structure of carbon micro/nano coil allows them to be cross-polarized, increase absorption and substantially increase the microwave loss.

HRTEM images of the nano-onion like carbon (OLC) (shown in Fig. 7) demonstrated that the OLC composed of inner multi-shell fullerene with stable defects protected by the outer defect-free shell [59]. These shells interact with the EM waves and attenuate them. However, the detailed mechanism for EM wave attenuation is still unclear. Moreover, their morphology, size, degree of

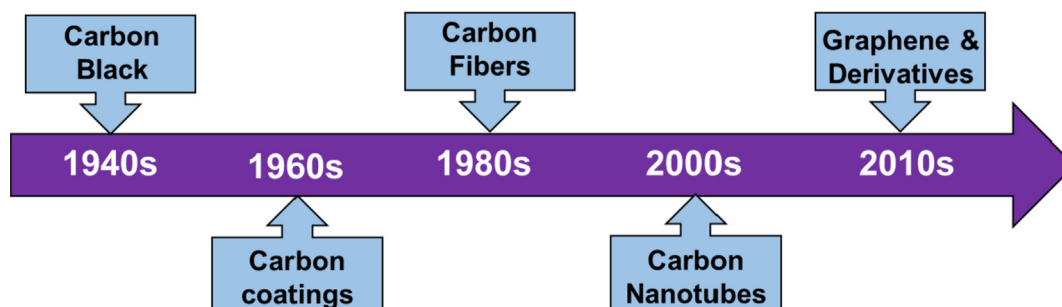


Fig. 3. Historical background of the carbon material used in EMI applications. (A colour version of this figure can be viewed online.)

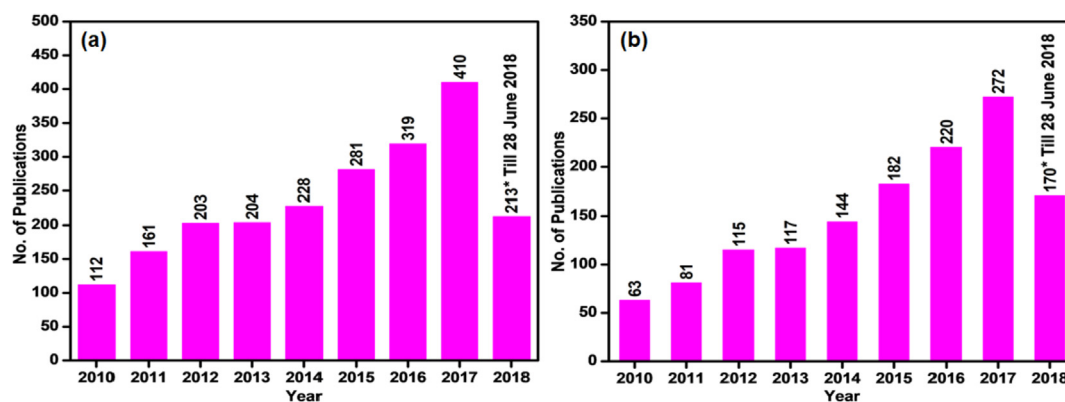


Fig. 4. (a) Number of the publications containing the string “Electromagnetic interference shielding” and (b) Number of the publications containing the strings “Electromagnetic interference shielding” and “Carbon” in article title, abstract and keywords. Data Source: Scopus, Elsevier. (A colour version of this figure can be viewed online.)

graphitization, physical and chemical properties, yield and cost depend on the reaction parameters, reactants, reaction medium, catalyst, energy source, etc. For example, Arjmand et al. investigated the effects of the catalysts such as Co, Ni, and Fe used for CNT preparation on the EMI performance. It has been observed that CNT obtained from CVD technique using Co as catalyst exhibited higher EMI shielding effectiveness (SE) values than the Fe and Ni catalysts [63].

Besides the pristine carbon nanostructures, their 3D structures such as foams, aerogel, and hydrogel have been prepared for EMI shielding applications. For example, Zhou et al. prepared graphene-CNT hydrogel films by a simple bar casting method, in which the solution containing GO and carboxylic CNT in deionized water was bar cast on polymethyl methacrylate (PMMA) substrate. Subsequently, the GO was reduced by chemical reduction. Finally, the resultant film was annealed at 2800 °C and mechanically pressed to

get 3 mm graphene-CNT hydrogel films [64]. Liu et al. prepared integrated graphene aerogels (IGA) containing highly conductive graphene sheets and graphitized carbon by graphitization of RGO sheets and polyimide (PI) component. The RGO/PI was obtained by thermally annealing the RGO/poly (amic acid) (PAA) aerogel at 300 °C in the argon atmosphere (Fig. 8).

The electric conductivity (σ) of carbon nanostructures can be adjusted by governing the carbonization temperatures. The carbonization temperature affects the graphitization degree and hence their σ [66]. Doping of carbon nanostructures with heteroatoms such as sulfur, nitrogen, and boron are reported to improve the σ as well as the EMI shielding properties. Fig. 9 (a and b) shows the TEM and SEM images of RGO doped with sulfur atom using H_2S gas at 1000 °C in the inert atmosphere [67]. The graphene possesses wrinkled and folded features. The optical image of the prepared GO and S-doped RGO is shown in Fig. 9c. The EDX analysis and

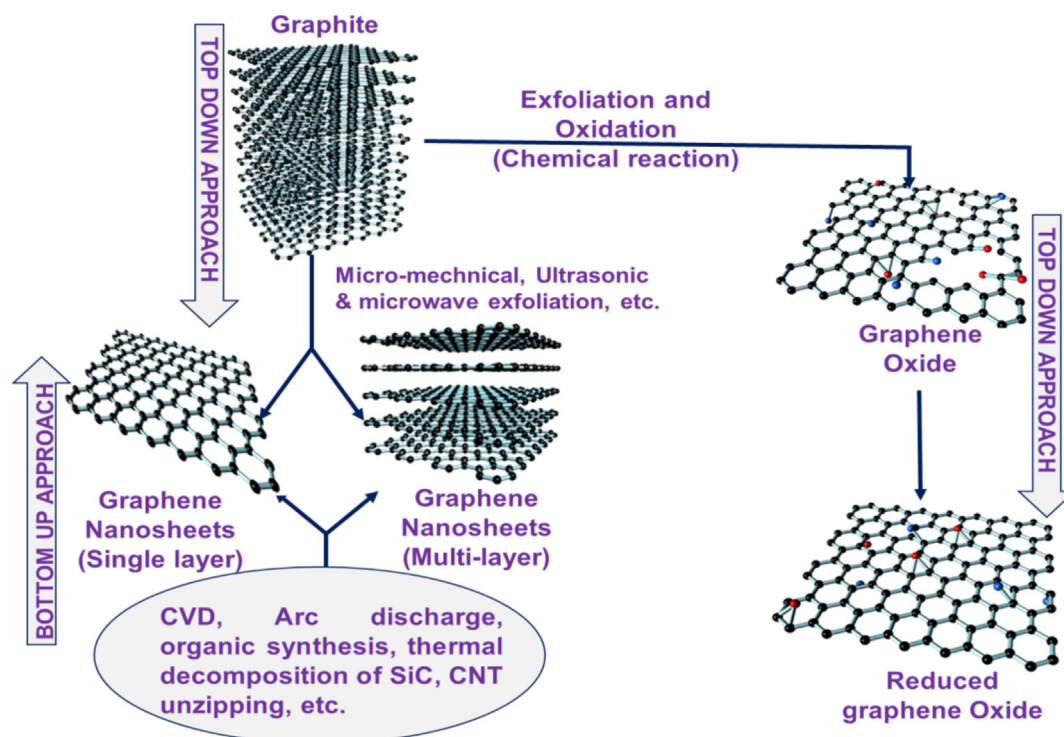


Fig. 5. Schematic representation of the methods for the synthesis of GN and RGO from graphite. Modified from Refs. [57,58]. (A colour version of this figure can be viewed online.)

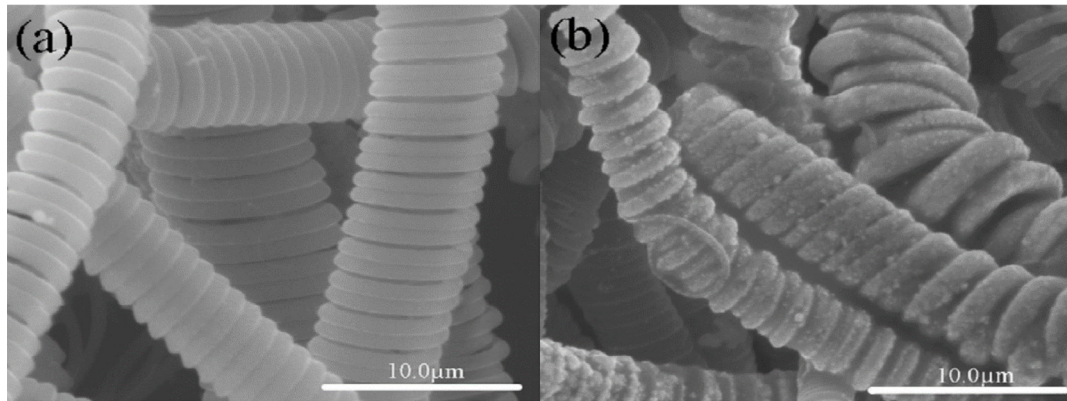


Fig. 6. SEM images of the (a) carbon micro coils (CMC) and (b) nickel coated carbon micro coils (Ni-CMC). Reproduced with permission from Ref. [62]. Copyright © 2008 Elsevier B.V.

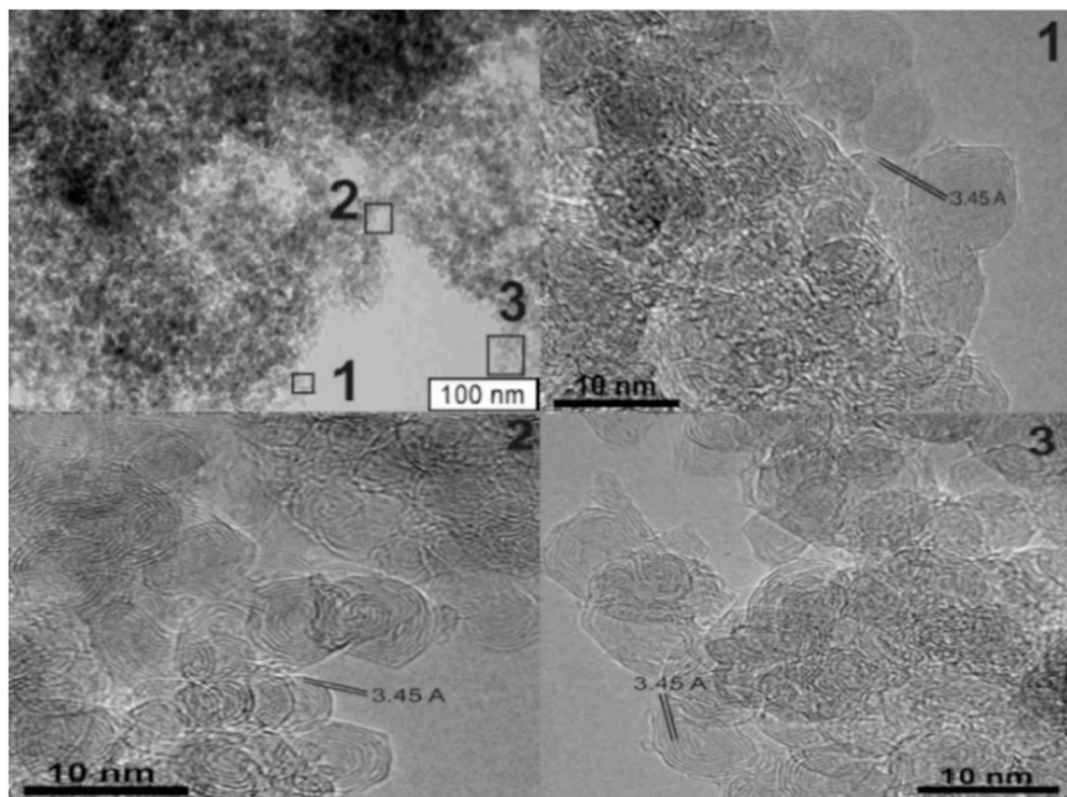


Fig. 7. HRTEM image of onion-like carbon powder. Reproduced with permission from Ref. [59]. Copyright © 2009 Elsevier B.V.

elemental mapping (Fig. 9d&e, respectively) confirmed the uniform doping of sulfur throughout the graphene. Fig. 9f shows the fracture surface of the laminated sample prepared for the measurements with longitudinally compacted graphene sheets (inset shows the digital image of the samples). Further, the doped sulfur atoms provide free carriers to the graphene because of excess valence electrons that shift the Fermi level towards the conduction band (CB) and thereby improve the σ . It has been observed that the doping of sulfur atom increases the σ of graphene by 47%.

There are several synthetic methods that have been adopted for the preparation of carbon nanostructured composites. The most extensively used technique for the hybridization of carbon materials with other materials such as magnetic materials, metal oxides, metal chalcogenides for their use as EMI shielding material is the hydrothermal/solvothermal method [68–70]. In a typical synthesis,

the metal precursors will be added to the dispersion of carbon nanostructures such as CNT, graphene, etc. followed by the reduction in a Teflon-lined autoclave at a certain temperature. The oxygen-containing functional groups such as hydroxyl, carboxyl, epoxy on the edge and basal plane of carbon nanostructures act as the preferential sites for the adsorption of metal ions. During the hydrothermal reaction, the metal ions nucleate at these sites and result in the desired product. Hence, a uniform distribution of nanoparticles on the carbon nanostructures can be achieved. The detailed mechanism of the above described synthesis procedure is illustrated in Fig. 10.

Several reducing agents, such as hydrazine hydrate, sodium citrate, polyol and sodium borohydride, are commonly used to reduce the metal ions and GO present in the solution to obtain carbon nanocomposites. This technique is able to control the

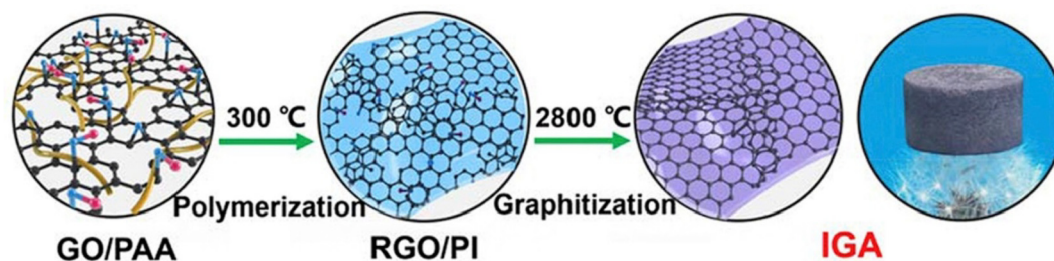


Fig. 8. Schematic illustration for fabricating IGA from GO/PAA and RGO/PI aerogels. Reproduced with permission from Ref. [65]. Copyright © 2018 Elsevier Ltd. (A colour version of this figure can be viewed online.)

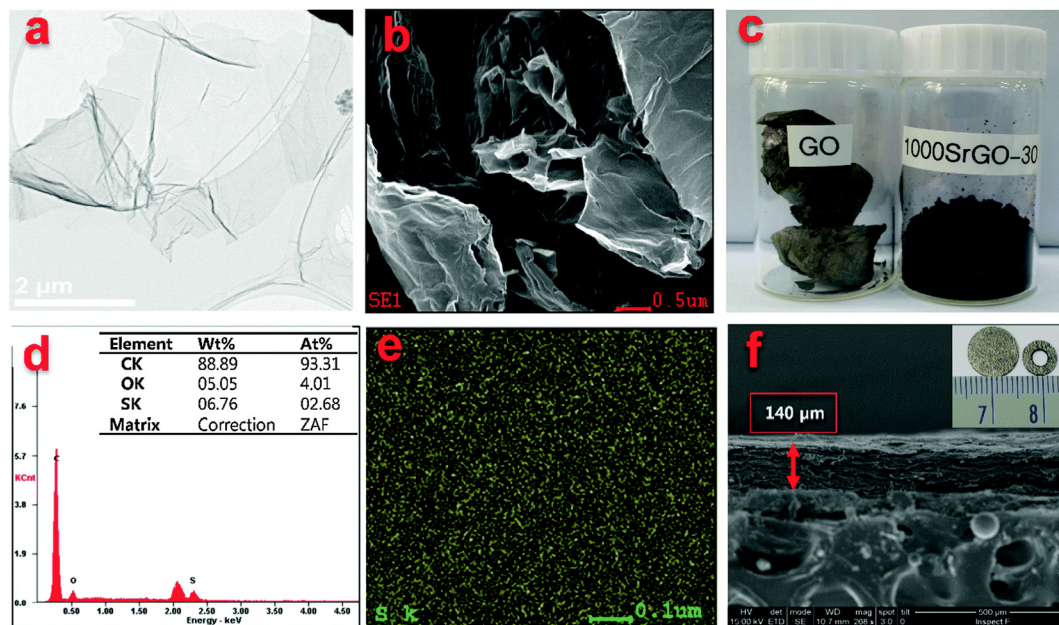


Fig. 9. (a) TEM and (b) SEM image of S doped RGO; (c) digital images of GO and S doped RGO (d and e) EDX analysis and elemental mapping of S doped RGO; (f) cross-sectional view of S doped RGO laminate (inset: samples prepared for measurements). Reproduced with permission from Ref. [67]. Copyright © The Royal Society of Chemistry 2015. (A colour version of this figure can be viewed online.)

morphology of the nanostructures and also has advantages such as low cost, environmental friendliness, and high product yield. Fig. 11 shows the TEM microstructure of Fe_3O_4 -Graphene hybrid prepared by a simple hydrothermal reaction. It depicts that the Fe_3O_4 nanocrystals are homogeneously dispersed and strongly anchored on the graphene nanosheets with no obvious agglomeration or large vacancies [71].

Besides the hydrothermal/solvothermal method, arc discharge, pyrolysis, CVD, template-assisted synthesis, etc. [73–76], are utilized for the preparation of carbon nanostructured composites. For example, Li et al. prepared sulfur-doped Fe@C nanocapsules by arc discharge method with methane as a gaseous carbon source, a mixture of iron and sulfur as the anode and carbon rod as cathode [77]. Chen et al. prepared α -MnS hollow spheres-RGO hybrid (MHS-RGO) by a solvothermal method using dimethylformamide (DMF) [72]. Hollow MnS spheres are formed by the time-dependent decomposition of amorphous MnS nanoparticles and Ostwald ripening as illustrated in Fig. 12. The corresponding TEM image (inset of Fig. 12) depicts that the α -MnS spheres with well-defined hollow structures are obtained by this approach.

Su et al. in-situ grew $\text{Ni}_{17}\text{S}_{18}/\text{Fe}_7\text{S}_8$ /encapsulated CNT by a one-step CVD process using dimethyl sulfide (liquid) as the sulfur source. Fig. 13 shows the HRTEM images, SAED pattern and EDX

spectrum of Fe_7S_8 -filled and $\text{Fe}_7\text{S}_8/\text{Ni}_{17}\text{S}_{18}$ -filled CNT. The results demonstrated that the $\text{Fe}_7\text{S}_8/\text{Ni}_{17}\text{S}_{18}$ nanostructures are encapsulated within the CNT. These $\text{Fe}_7\text{S}_8/\text{Ni}_{17}\text{S}_{18}$ nanostructures filled CNT resulted from the concurrent sulfurization of metal catalysts and CNT growth [78].

3. Concept of electromagnetic interference (EMI) and shielding

Electromagnetic interference (EMI) is the process by which disruptive electromagnetic energy is transmitted from one electronic device to another via radiated or conducted paths or both. EMI can be dominated by radiation or conduction, depending on the type of coupling or propagation path involved. However, conduction always accompanies some radiation and vice versa. Radiated interference occurs when the electromagnetic energy emitted by an equipment is transferred to the receptor through space. Conducted interference happens when the electromagnetic energy emitted by an equipment is transferred to the receptor through the cables (external connections). If the conducted emissions are reduced, the relative radiated emissions are also often reduced. However, the dominant radiated interference can affect any signal path within and outside the system/device and is much more

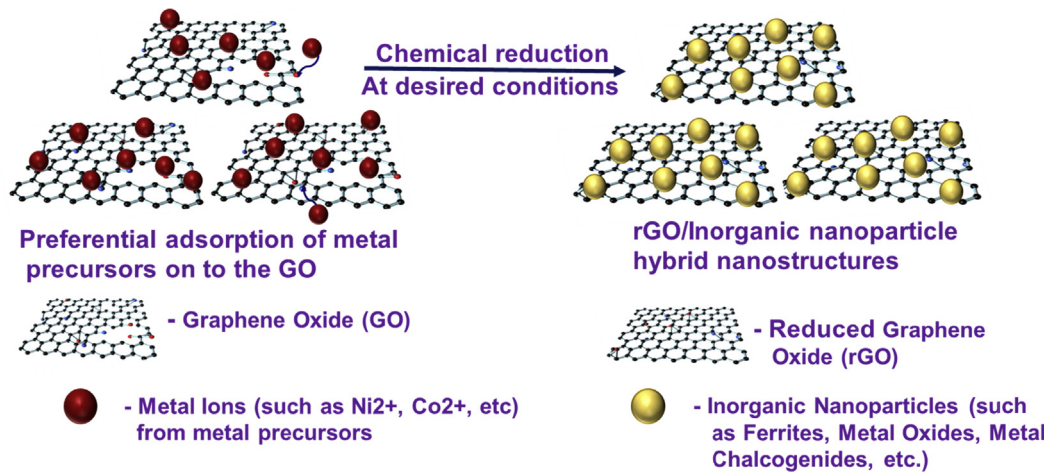


Fig. 10. Schematic illustration for the formation of nanostructured carbon composites by hydrothermal/solvothermal synthesis. (A colour version of this figure can be viewed online.)

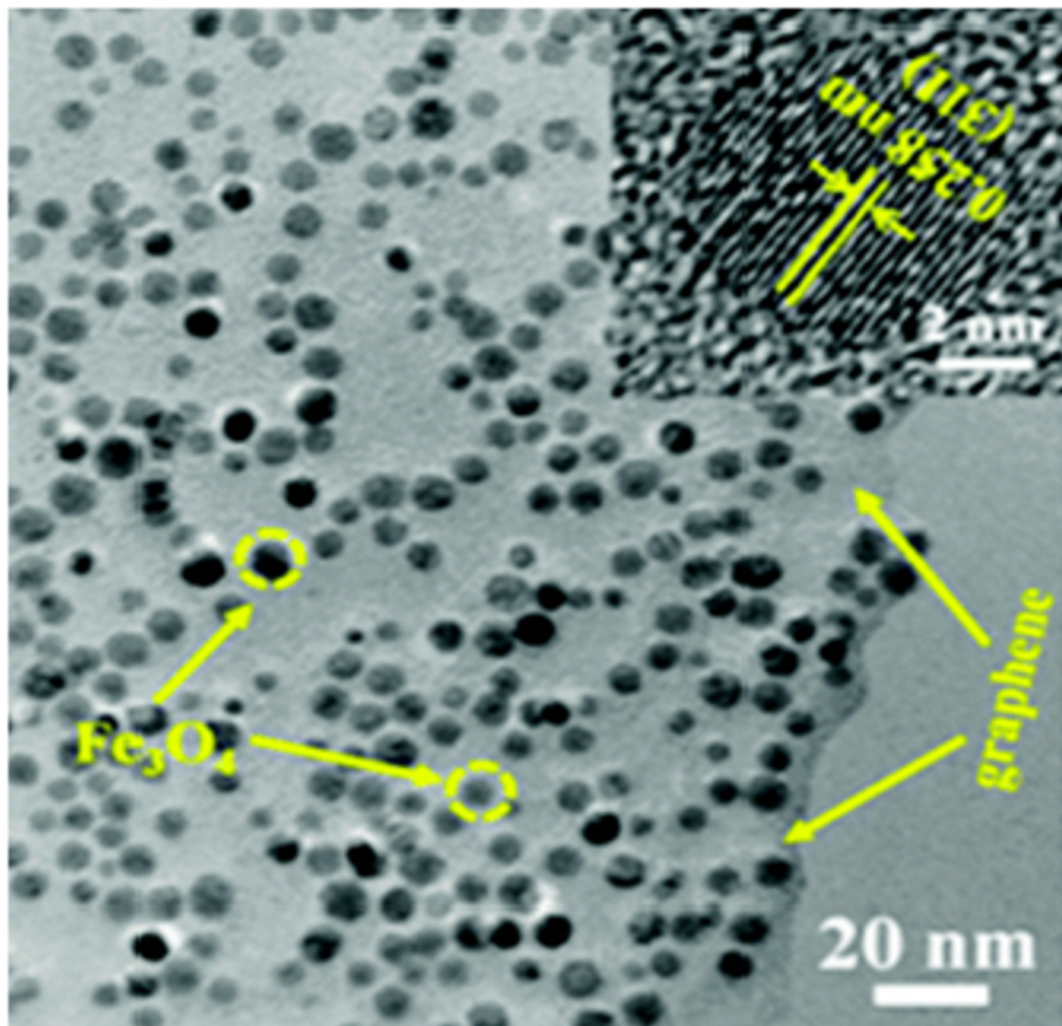


Fig. 11. TEM image of Fe₃O₄-Graphene hybrid. Reproduced with permission from Ref. [71]. © The Royal Society of Chemistry 2015. (A colour version of this figure can be viewed online.)

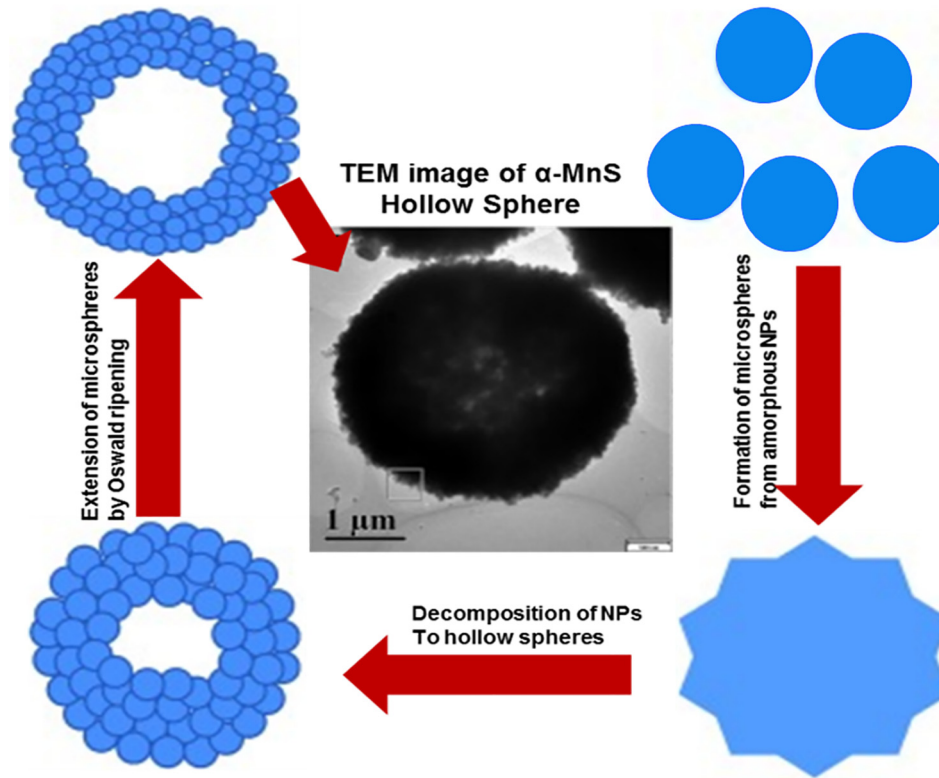


Fig. 12. Time evolution mechanism describing the formation of α -MnS hollow sphere and TEM images of the α -MnS hollow sphere after time evolution of 4 h. Reproduced with permission from Ref. [72]. Copyright © 2013 Wiley-VCH Verlag GmbH & Co. KGaA, Weinheim.

difficult to be shielded [79]. Suppression is the process of reducing or eliminating EMI energy. It may include shielding and filtering. Shielding can be specified in terms of reduction in magnetic (and electric) field or plane-wave strength [2]. The EM spectrum can be classified either by frequency of oscillation or by wavelength. All electromagnetic waves consist of two essential components, a

magnetic field (H) and an electric field (E) as shown in Fig. 14.

These two fields are perpendicular to each other and the direction of wave propagation is at right angles to the plane containing these two components. The relative magnitude depends on the waveform and its source. The ratio of E to H is called wave impedance. The intrinsic impedance of free space is 377 Ω [80]. EMI

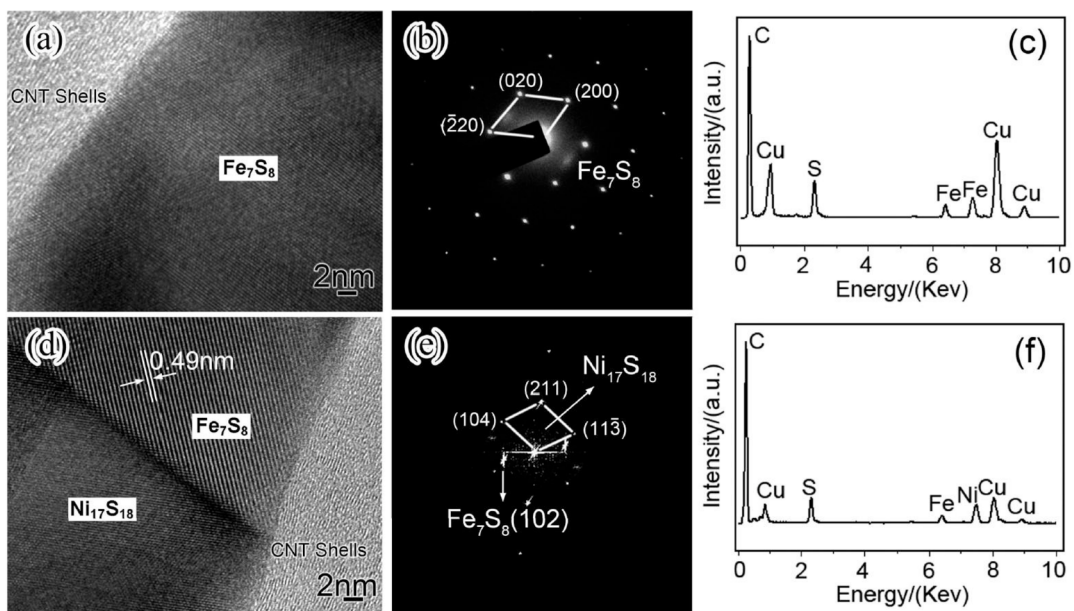


Fig. 13. HRTEM image (a) of a Fe_7S_8 -filled CNT and its corresponding SAED pattern (b) and EDX spectrum (c); HRTEM image (d) of a $\text{Fe}_7\text{S}_8/\text{Ni}_{17}\text{S}_{18}$ -filled CNT and its corresponding Fast Fourier transform (FFT) pattern (e) and EDX spectrum (f). Reproduced with permission from Ref. [78]. Copyright © 2011 American Chemical Society.

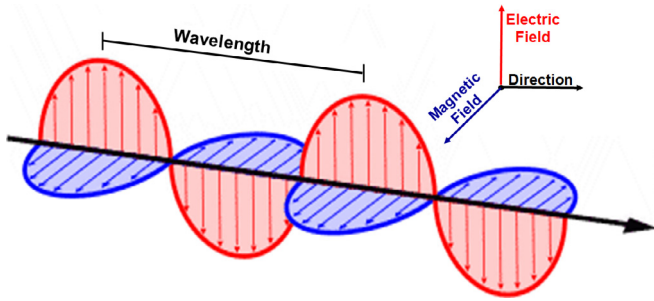


Fig. 14. Schematic representation of EM wave. (A colour version of this figure can be viewed online.)

shielding is typically measured in terms of insertion loss, that is, the reduction in the fields coupled between a transmitter and a receiver due to the insertion of the shielding material.

An electromagnetic shielding material is a material that attenuates radiated electromagnetic energy. With respect to the wavelength of the electromagnetic radiation (λ), the distance between the electromagnetic radiation source and shielding material (r) can be divided into three regions, namely, near field region (Reactive Field or Fresnel Zone), transition region and far-field region (Radiation Field or Fraunhofer Zone), as shown in Fig. 15. In near field ($r < \lambda/2\pi$), the electromagnetic signal can be predominantly an electric vector or a magnetic vector depending on the nature of the source. In the far field ($r > \lambda/2\pi$), plane waves exist, the electric and magnetic vectors have an equal ratio in phase and are orthogonal to each other. Between these two regions, there exist the transition

region at $r \approx \lambda/2\pi$ [82]. The plane radiation (far field) is generally used in evaluating SE. The SE is a number that quantifies the amount of attenuation typical of a particular EMI shielding material. The effectiveness of a shield and its resulting EMI attenuation are based on the frequency, the distance of the shield from the source, the thickness of the shield, and the shield material.

3.1. Shielding effectiveness (SE)

SE is the ratio of the impinging energy to the residual energy. SE is normally expressed in decibel (dB) as a function of the logarithm of the ratio of the incident to transmitted electric (E), magnetic (H), or plane-wave (P) field intensities: $SE(dB) = 20 \log\left(\frac{E_i}{E_t}\right)$, $SE(dB) = 20 \log\left(\frac{H_i}{H_t}\right)$, or $SE(dB) = 20 \log\left(\frac{P_i}{P_t}\right)$, respectively, where E, H and P represent the electric field intensity, magnetic field intensity and plane-wave field intensity, respectively. The subscripts T represents the transmitted wave and I represent the incident wave.

For any kind of EMI, three mechanisms contribute to the effectiveness of the shielding. Part of incident radiation is reflected from the front part of the shield, part is absorbed within the shielding material, and the left is reflected from the shield rear surface to the front (multiple internal reflections) where it can aid or hinder the effectiveness of shielding depending on its phase relationship with incident wave, as shown in Fig. 16.

Therefore, the total shielding effectiveness (SE) of shielding material equals to the sum of the absorption factor (A), the reflection factor (R), and the correction factor to account for multiple reflections (B) in thin shields as shown in equation (1) [83]:

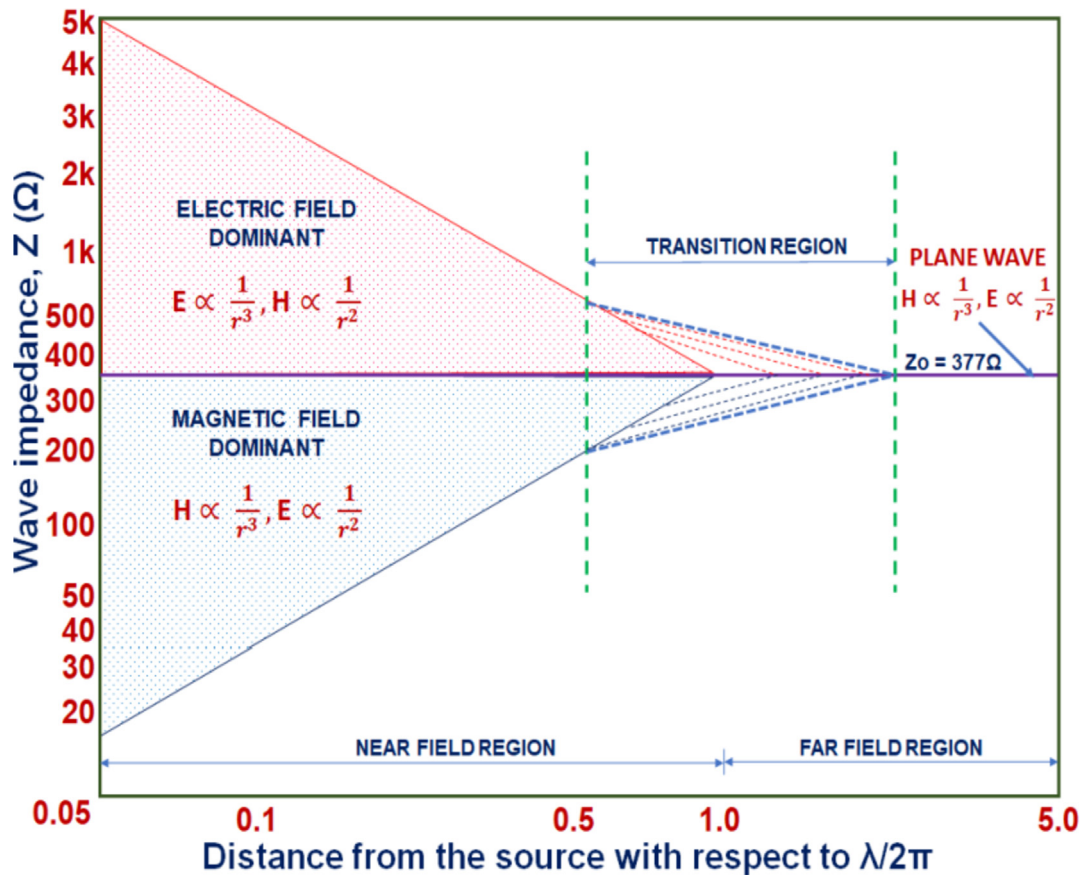


Fig. 15. Dependence of wave impedance on distance from source normalized to $\lambda/2\pi$. Modified from Ref. [81].

$$SE = R + A + B \quad (1)$$

All the terms in Equation (1) are expressed in dB.

The multiple reflection factor B can be neglected if the A is greater than 10 dB. In the practical calculation, B can also be neglected for electric fields and plane waves. The amount of reflection loss depends on the impedance of the electromagnetic wave and the shield. When an electromagnetic wave encounters a shield, the wave is partially reflected back. Conversely, if the wave impedance and the shield impedance are closely matched, the EMI energy will pass through the shield with a minimal reflection.

Generally, an increase in SE_R represents an enhanced impedance mismatch between the air and the shielding materials when frequency varies and SE_A scales by increasing the attenuation of EM energy. The impedance matching conditions and the factors governing the impedance matching are briefly explained later in the following sections.

3.2. Experimental evaluation of EMI shielding property

Experimentally, EMI SE of an EMI shielding material is measured using instruments called network analyzer. A **scalar network**

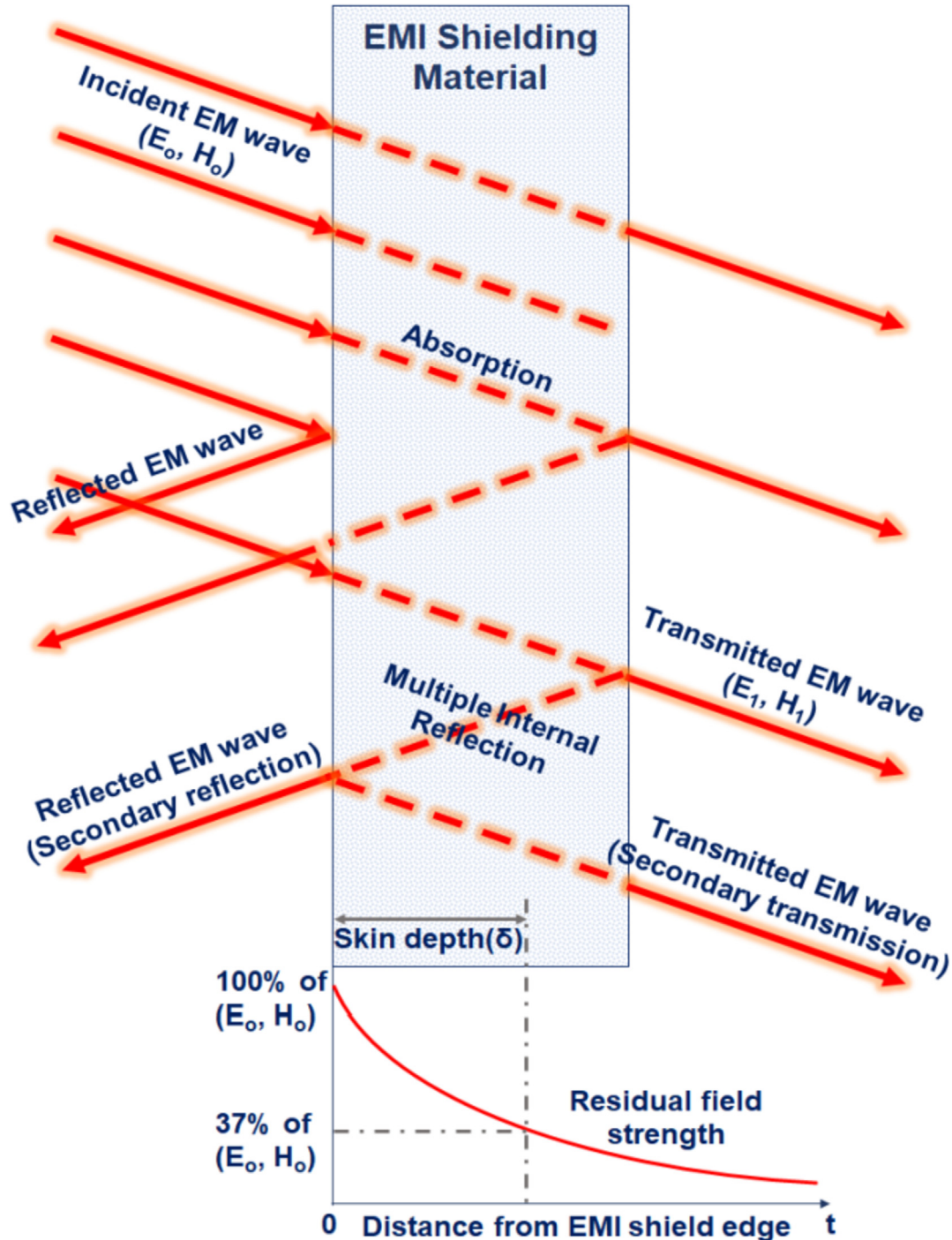


Fig. 16. Schematic representation of EMI shielding mechanism. (A colour version of this figure can be viewed online.)

analyzer (SNA) measures only the amplitude properties of signals whereas **vector network analyzer (VNA)** measures amplitude response as well as phases of signals. Consequently, SNA cannot be used to measure complex signals (e.g. complex permittivity (ϵ_r) or complex permeability (μ_r)) and therefore, despite its higher cost, VNA is the most widely used instrument.

The incident and transmitted waves in two-port VNA (Fig. 17) can be mathematically represented by complex scattering parameters (or S-parameters), S_{11} and S_{12} . These parameters can be correlated with the reflection coefficient (R), and transmission coefficient (T), as $R = |S_{11}|^2$ and $T = |S_{12}|^2$, respectively. The absorption coefficient (A) can be obtained using the relation $A + R + T = 1$, from the values of R and T. According to the ratio of the incident wave P_I to the transmitted wave P_T , the EMI SE can be calculated by Equation (2):

$$SE = 10 \log \left(\frac{P_I}{P_T} \right) \quad (2)$$

3.3. Design consideration for EMI shielding materials

The basic shielding mechanism for an EMI shielding material mainly depends on its complex permittivity ($\epsilon_r = \epsilon' - j\epsilon''$), complex permeability ($\mu_r = \mu' - j\mu''$), thickness, structure and the nature of the incident radiation. Parameter ϵ' (real permittivity) represents the charge storage (or dielectric constant) whereas ϵ'' (imaginary permittivity) is a measure of dielectric dissipation or losses. Similarly, μ' and μ'' represent magnetic storage and losses, respectively. The extent of losses can be assessed by calculating dielectric/magnetic loss tangent ($\tan \delta_E = \frac{\epsilon''}{\epsilon'}$ / $\tan \delta_M = \frac{\mu''}{\mu'}$). The SE of an EMI shielding material strongly depends on ϵ_r and μ_r , and SE_R and SE_A can be expressed as in Equations (3) and (4), respectively [84]:

$$SE_R \approx 10 \log[\sigma_{ac}/16\omega\epsilon_0\mu_r] \quad (3)$$

$$SE_A = 20\{t/\delta\} \log e = 20t\sqrt{\omega\sigma_{ac}\mu_r/2} \quad (4)$$

where σ_{ac} depends on the dielectric properties of the material, ω is

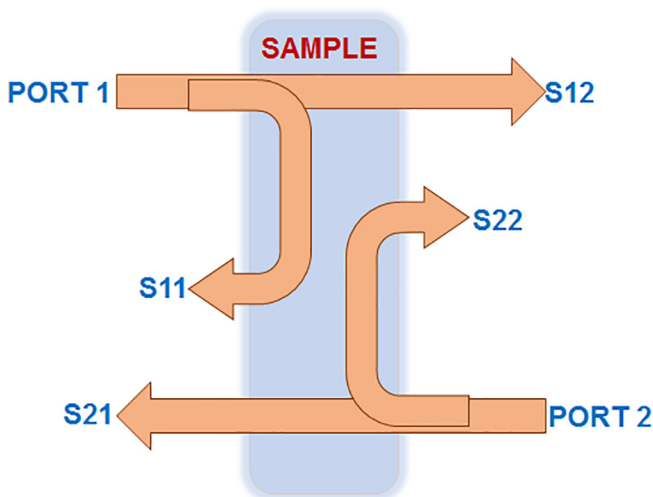


Fig. 17. Schematic illustration of scattering parameter in two-port VNA. (A colour version of this figure can be viewed online.)

the angular frequency, ϵ_0 , μ_r , δ and t are free space permittivity, complex permeability, skin depth and thickness of the shield material, respectively.

Thus, SE_R has a relationship with the value of σ_{ac}/μ_r , implying that the SE_R decreases with increasing the μ_r . On the other hand, SE_A is caused by the heat loss under the action between electric dipole and/or magnetic dipole in the electromagnetic field so that the absorption loss is proportional to the value of $\sigma_{ac}\mu_r$. This indicates that a higher μ_r leads to a higher absorption loss. In the absence of magnetic permeability, the absorption and reflection loss depend on the dielectric properties.

3.4. Microwave absorption property of EMI shielding material

Microwave absorption (MA) of EMI shielding material is reflected by the reflection loss (RL). Based on transmission line theory, RL can be calculated using Equation (5) [85]:

$$RL = 20 \log_{10} \frac{|Z_{in} - Z_0|}{|Z_{in} + Z_0|} \quad (5)$$

where Z_{in} is the normalized input impedance of the absorber, Z_0 is the impedance of free space.

The normalized input impedance (Z_{in}) of an absorber backed by a metallic reflector can be expressed as Equation (6):

$$Z_{in} = \sqrt{\frac{\mu_r}{\epsilon_r}} \tanh \left[j \frac{2\pi}{c} \sqrt{\mu_r \epsilon_r} fd \right] \quad (6)$$

where ϵ_r and μ_r are the complex permittivity and permeability of the absorber, respectively, c is the velocity of light and d is the thickness of the EM absorber.

When the RL is lower than -10 dB, more than 90% of the EM wave energy is absorbed. When RL is lower than -20 dB, more than 99% of the EM wave energy is absorbed, which means that these areas can be seen as an effective EM wave bandwidth.

3.4.1. Impedance matching conditions

Microwave absorption of the EMI shielding material can be tuned by impedance matching. The increasing microwave absorption (achieved by good impedance matching) can be attributed to a good balance between the dielectric loss ($\tan \delta_E$) and magnetic loss ($\tan \delta_M$). Fig. 18 shows the relationship between the impedance matching and EM wave absorption performance.

From Equations (5) and (6), it is well known that the best electromagnetic matching for zero reflection of EM wave should be $\tan \delta_M = \tan \delta_E$ [86]. However, the existing materials could not be $\tan \delta_M = \tan \delta_E$ at the whole frequency, and thus microwave absorption of absorbers is frequency-dependent. The minimum RL can be expressed as follows:

$$\frac{\mu_r}{\epsilon_r} \tanh j \frac{2\pi f}{c} \sqrt{\mu_r \epsilon_r} d = 1 \quad (7)$$

In the case of the magnetic/dielectric component, Equation (7) is usually divided into two equations as,

$$\mu'' = \frac{c}{2\pi f_m d} \quad (8)$$

$$\epsilon'' = \frac{c}{2\pi f_m d} \quad (9)$$

where f_m is the best matching peak frequency of microwave absorption and related to the thickness of the absorber and the μ''/ϵ'' is affected by the fundamental magnetic/dielectric properties.

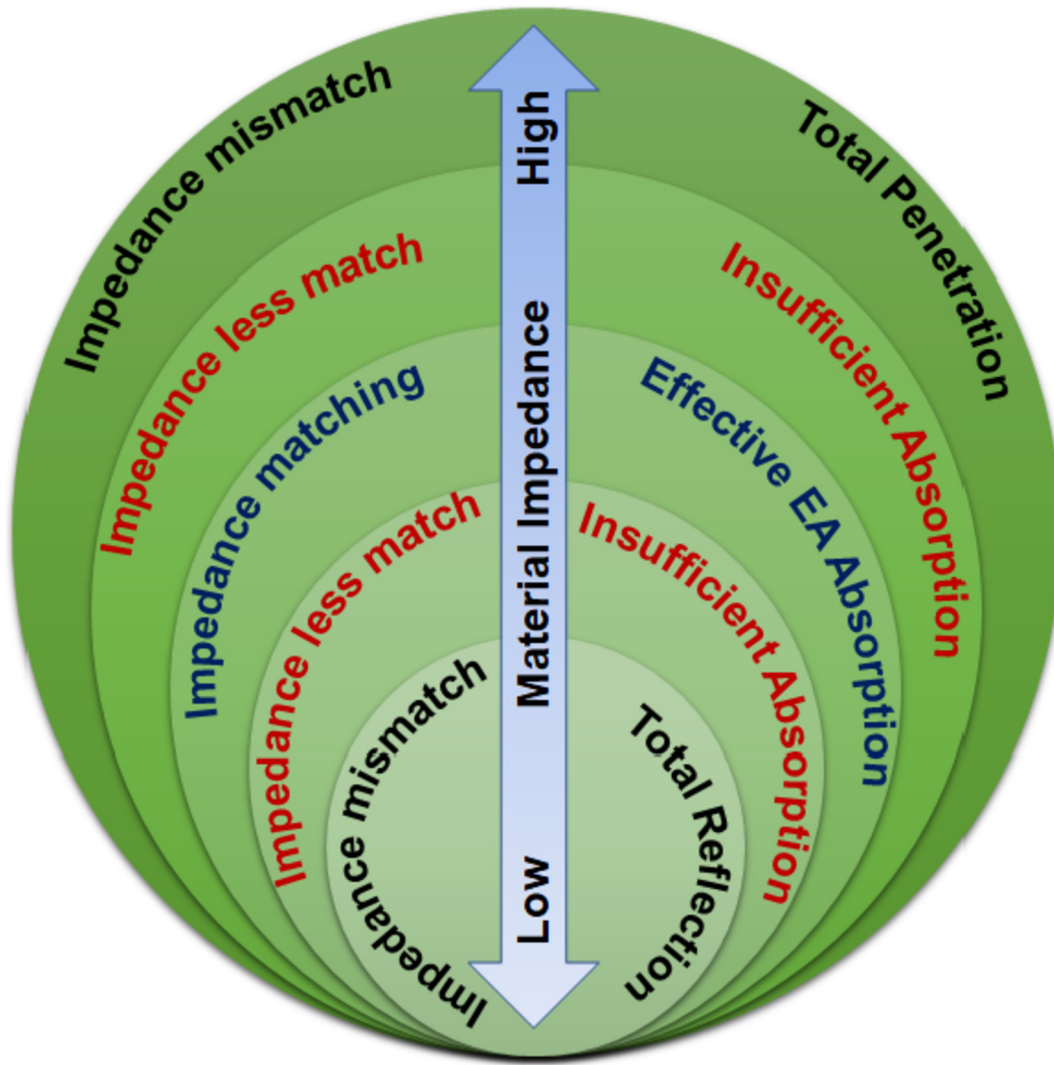


Fig. 18. Relationship between the impedance matching and EM wave absorption performance. (A colour version of this figure can be viewed online.)

Meanwhile, the attenuation constant α is another essential factor for an outstanding absorber. The α can be defined as,

$$\alpha = \frac{\sqrt{2\pi f}}{c} \times \sqrt{(\mu''\epsilon'' - \mu'\epsilon') + \sqrt{(\mu''\epsilon'' - \mu'\epsilon')^2 + (\mu''\epsilon'' + \mu'\epsilon')^2}} \quad (10)$$

where f is the frequency of electromagnetic wave propagation and c is the velocity of light. It is obvious that higher values of ϵ'' and μ'' could induce a higher α .

3.5. Dielectric properties

According to Debye theory, the ϵ'' stands for the loss of capability of electromagnetic energy. The $\tan \delta_E$ consists of both polarization loss and conduction loss, as clarified by equations (11) and (12), respectively [87]:

$$\epsilon' = \epsilon_\infty + \frac{\epsilon_s - \epsilon_\infty}{1 + \omega^2\tau^2} \quad (11)$$

$$\epsilon'' = \frac{\epsilon_s - \epsilon_\infty}{1 + \omega^2\tau^2} \omega\tau + \frac{\sigma}{\omega\epsilon_0} \quad (12)$$

where ϵ_s is the static dielectric constant, ϵ_∞ is the relative dielectric constant at the high-frequency limit, ω is the angular frequency, σ is the electrical conductivity, and τ is the polarization relaxation time, which has a connection with frequency and temperature.

According to Equations (11) and (12), the Cole-Cole equation gives the relationship between ϵ' and ϵ'' as follows:

$$\left(\epsilon' - \frac{\epsilon_s + \epsilon_\infty}{2}\right)^2 + (\epsilon'')^2 = \left(\frac{\epsilon_s - \epsilon_\infty}{2}\right)^2 \quad (13)$$

In the plot of ϵ'' vs ϵ' (Cole-Cole plot), a semicircle corresponds to one Debye relaxation process. If more than one superimposed Cole-Cole semicircles are found, each semicircle corresponds to a Debye dipolar relaxation [88]. If the Cole-Cole semicircle is distorted, besides the dielectric relaxation, other mechanisms such as the motion of conducting electrons and the heterogeneous interface polarization contribute to the permittivity spectra [89]. In the

absence of obvious semicircles, dielectric loss results mainly from the conduction loss, which can be expressed according to the free electron theory as,

$$\epsilon'' = \frac{\sigma}{2\pi\epsilon_0} \cdot \frac{1}{f} \quad (14)$$

The dielectric constant decreases with increasing the frequency. The frequency-dependent dielectric response can be explained by the presence of electric dipoles. When the frequency of the applied field is increased, the dipoles present in the system cannot reorient themselves fast enough to respond to the applied electric field and as a result, dielectric constant decreases.

3.6. Magnetic properties

Magnetic loss generally derives from natural resonance, exchange resonance, and eddy current loss. Natural resonance usually appears at a lower frequency, the low-frequency resonance peak may be attributed to “exchange mode” resonance and the nanometer-sized particles will enhance the resonance [73,90,91]. According to the ferromagnetic resonance theory, the natural resonance frequency (f_r) can be expressed by equations (15&16) [92]:

$$f_r = \frac{\gamma}{2\pi} H_{eff} \quad (15)$$

$$H_{eff} = \frac{4|K_1|}{3\mu_0 M_s} \quad (16)$$

where $\frac{\gamma}{2\pi}$ is the gyromagnetic ratio (28 GHz T^{-1}), H_{eff} is the effective magnetic field, K_1 is the magneto-crystalline anisotropic coefficient for magnetic material, and $\mu_0 M_s$ is the saturation magnetization.

The loss due to eddy current effect can be expressed as:

$$C_o = \mu'' (\mu')^{-2} f^{-1} = 2\pi\mu_0\sigma d^2/3 \quad (17)$$

where σ is the electrical conductivity, d is the diameter of nanoparticles and μ_0 is the vacuum permeability. If the magnetic loss results from the eddy current loss effect, the values of C_o are constant when the frequency is changing (which is called the skin-effect criterion). The loss in eddy current of a magnetic particle with diameter, D , less than the skin depth can be expressed by,

$$\frac{\mu''}{\mu'} \propto \frac{\mu'' f D^2}{\rho} \quad (18)$$

where f is the applied frequency, ρ is the electrical resistivity of the particle.

3.7. Skin depth

Electromagnetic radiation at high frequencies penetrates only near the surface region of an electrical conductor. This is known as the skin effect. The electric field of a plane wave penetrating a conductor drops exponentially with increasing the depth into the conductor. The depth at which the field drops to 1/e or 37% of the incident value is called the **skin depth** (δ) (illustrated in Fig. 16). Mathematically, the skin depth can be calculated using the following expression,

$$\delta = (\pi f \mu_o \mu_R \sigma)^{-1} \quad (19)$$

where δ is the skin depth, f is the frequency, μ_o is equal to $4\pi \times 10^{-7} \text{ Hm}^{-1}$, and μ_R is the relative permeability of EMI shielding material. Hence, the δ will decrease inversely with increasing the frequency and conductivity/permeability of EMI shielding material. Based on the transmission line theory and plane wave theory, shielding mechanism of an EMI shielding material can be inferred with respect to δ and thickness as follows:

- When the thickness of an EMI shielding material is much less than the skin depth ($t \ll \delta$), the attenuation occurs exclusively by reflection. This condition occurs either at low frequencies or in case of the electrically conductive thin sample. In this case, the total shielding phenomena is independent of frequency.
- When the thickness of an EMI shielding material is much greater than the skin depth ($t \gg \delta$), attenuations take place by reflection, absorption and multiple internal sub-phenomenon for the good conductors, whose $\sigma_T/\omega\epsilon \gg 1$. In this case, the total shielding phenomenon depends on frequency. This condition occurs either at high frequencies or in case of the electrically conductive thick sample [81].

Apart from the $\tan \delta_E$ and $\tan \delta_M$, the microwave can also be absorbed by means of the “geometrical effect”. According to the quarter wave principle,

$$t_m = \frac{n\lambda}{4} = \frac{nc}{4f_m \sqrt{|\epsilon_r| |\mu_r|}} \quad (n = 1, 3, 5, \dots) \quad (20)$$

where t_m is the matching thickness of maximum microwave absorption, λ is the wavelength in the materials, f_m is the peak frequency, ϵ_r and μ_r are the complex permittivity and complex permeability of the EMI shielding materials at f_m , respectively, and c is the velocity of light. If the above equation is satisfied, the incident and reflected waves in the absorbers are out of phase by 180° , resulting in the disappearance of each other at the air-absorber interface. Interference hardening loss is another important dissipation factor other than the $\tan \delta_E$ and $\tan \delta_M$. Interference hardening loss refers to the electromagnetic interference rejection by an EMI shielding material at its surface. The quarter-wave principle is an effective tool for offering a crucial guide in the thickness design of a microwave absorber. According to Equation (20), enhanced μ_r and ϵ_r are necessary for composite absorbers with thin matching thickness.

4. Electronic transport properties of carbon nanostructures

In case of graphene, the σ , functional groups and defects contribute to the EMI shielding. The σ determines the reflection and conduction loss, in the meantime, the functional groups and defects improve the polarization loss [33]. The σ of single-layer graphene is nearly $\sim 10^8$ and it decreases by increasing the layer as well as the defects which occur during the chemical fabrications/modifications [93–96]. Fig. 19 describes the electron transportation in the GN, GO and RGO, respectively [56]. Since the CF and CNT are composed of graphitic layers, their electronic transport will be similar to that of graphene.

In spite of lower σ , chemically synthesized graphene is usually used in EMI shielding because of the induced functional groups and defects, as they contribute to the polarization loss. In the case of graphene, both ϵ_r and EMI SE increase with decreasing the

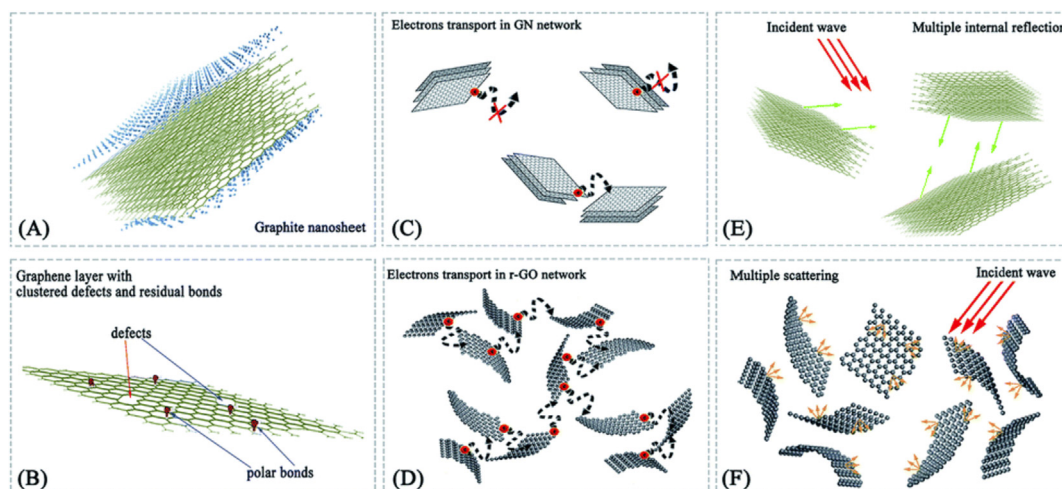


Fig. 19. (A and B) Microstructure of GN and RGO. (C and D) Electron transport network of GN and RGO. (E and F) Microwave propagation model in GN and RGO. Reproduced with permission from Ref. [56]. Copyright © The Royal Society of Chemistry 2014. (A colour version of this figure can be viewed online.)

thickness, that is, both ϵ_r and EMI SE increase from graphite to expanded graphite and GN. For example, Song et al. demonstrated that the ϵ' and ϵ'' values of GN composites were higher than those of expanded graphite composites at different frequencies (Fig. 20). As the filler content increases, both of these composites exhibit a monotonous increase in the values of ϵ' and ϵ'' irrespective of frequency (Fig. 20a–d). The increased aspect ratio achieved by decreasing the thickness of expanded graphite results in the increased ϵ' and ϵ'' and EMI SE. With the increase in aspect ratio, the GN would provide more prospects for the formation of parallel plate capacitor structure (Fig. 21a), that favors polarization attributed from the alignment of polar bonds/charges with respect to the electromagnetic field; conductive pathways (Fig. 21b) that improves σ ; and multiple internal reflections (Fig. 21c) that improves the attenuation of EM radiation. All these contributed to the improved EMI performance of GN than the expanded graphite [97].

5. Pristine carbon nanostructures as EMI shielding materials

Electromagnetic (EM) wave absorbing and interference (EMI) shielding materials, besides strong absorption capability in a broad frequency range, have also been desired for low density, high thermal stability and good mechanical properties for the applications in aviation and space flight. Carbon nanostructures display outstanding physical properties, namely, high σ , low density, and good stability, that make them superior candidates for EMI shielding.

Carbon black (CB) is used in EMI shielding applications, mainly as conductive fillers in composite materials, due to their σ , chemical resistance, and low density. Generally, CB with smaller particle size, lower particle density, higher structure and low volatility (fewer chemisorbed oxygen groups) attributed to high σ in conductive polymer nanocomposites (CPC) [98].

Carbon fibers (CF) have good electrical properties. In addition, their high abundance along with low density and high strength suit them for EMI shielding application. It is reported that activation of CF can significantly enhance the multiple reflections with a longer propagation distance inside the composites which results in higher EM absorption [99,100]. Carbon nanofibers (CNF) have the diameters of 100–200 nm located at the size boundary between CNT and CF.

The small diameter, high aspect ratio, high σ , excellent

mechanical strength along with excellent dielectric polarization properties of CNT, make them an excellent choice for EMI shielding [101]. Moreover, their high aspect ratio can contribute to the three-dimensional conducting pathway and thereby provide high σ at small filler loading. The electrical properties of SWCNT differ from their MWCNT counterparts. They exhibit either semiconducting or metallic behavior depending on the chirality and diameter. In addition, metallic SWCNT with small diameter have been found to exhibit ballistic electron transport at low temperature [102,103]. Hence, the EMI shielding properties for the MWCNT and SWCNT incorporated composites will be different for per unit wt. % added to the host. Till now, most of the EMI studies have been carried out with MWCNT. For example, Wu et al. investigated the EMI SE of CNT macro-film adhered to the common cloth using styrene-acrylic emulsion. The EMI SE of the composite film did not decrease with increasing the frequency, attributed to the higher σ and significant skin effect of the CNT macro-film. The prepared CNT macro films with $\sim 4 \mu\text{m}$ thickness exhibited EMI SE of 48–57 dB at the range of 40–60 GHz. The calculated skin depth values (~ 0.05 – $0.06 \mu\text{m}$) are lower than the film thickness [10].

Fan et al. [43] investigated the effects of mechanical milling time, ultrasonic vibration time and the weight ratio of flake graphite (FG) in phenol-formaldehyde cement (PFC) on the EMI performance (Fig. 22a–c). Fig. 22d illustrates that the EM wave reflects more time at a dihedral angle of graphite flake that results in an increased EM wave attenuation. Dihedral angle of graphite flakes is the angle between two intersecting planes of each unit of three atoms, where their intersecting line is defined by two atoms among them. The absorption performance of FG enhances with increasing the milling time because the dihedral angle can be easily formed between the milled flake graphite. 25 wt% of GF in PFC exhibited a RL of < -12 dB in the frequency range of 14.4–18 GHz.

Gongoi et al. prepared expanded graphite/novolac phenolic resin composites containing different weight ratios (30, 40 & 50 wt %) of expanded graphite and demonstrated that 50 wt% EG composite showed a maximum σ of ~ 147 S/cm with a RL of > -13 dB throughout the entire X-band [104]. Liu et al. added a small amount of flexible graphene (GE) into the expanded graphite (EG) film to improve the mechanical properties of EG by forming simulated shell structure. The flexible GE filled the gaps of the EG and introduced wrinkles that can be stretched folding or stretching, resulting in excellent flexibility compared with pure EG films. High EMI

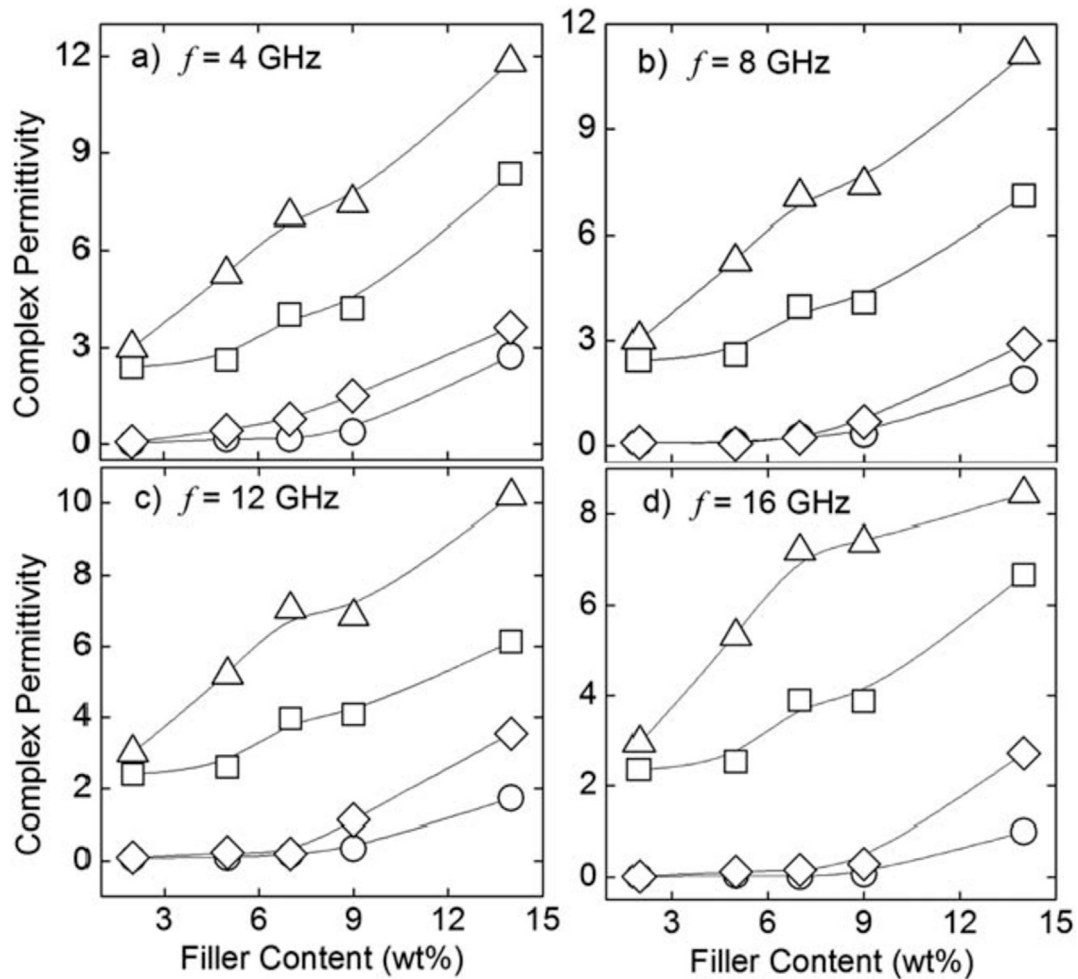


Fig. 20. Real permittivity of expanded graphite (square) and carbon nanosheets (triangle) and imaginary permittivity of expanded graphite (circle) and carbon nanosheets (diamond) loaded in the wax matrix at different frequencies. Reproduced with permission from Ref. [97]. Copyright © The Royal Society of Chemistry 2013.

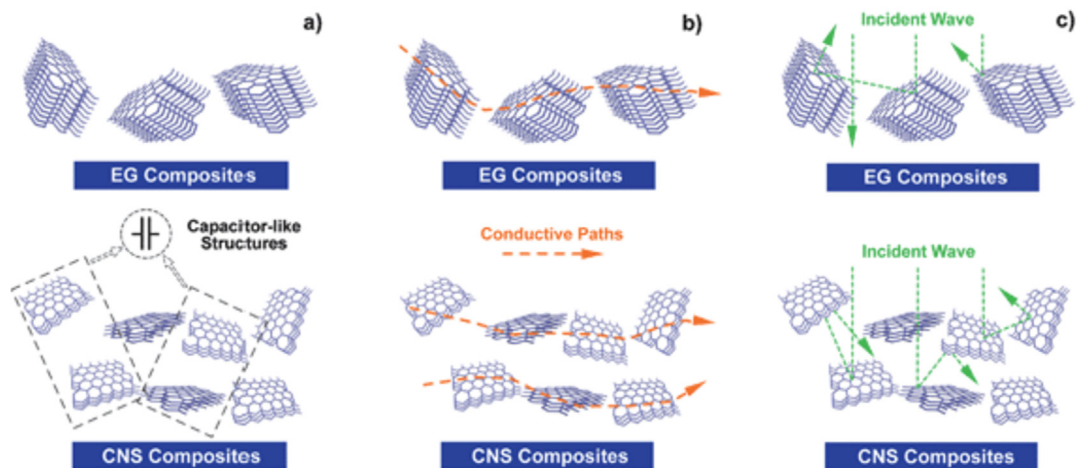


Fig. 21. Illustrations of forming capacitor-like structures (a) and electrically conductive paths (b) and producing multiple internal reflections (c) (upper: EG/wax composites; lower: CNS/wax composites). Reproduced with permission from Ref. [97]. Copyright © The Royal Society of Chemistry 2013. (A colour version of this figure can be viewed online.)

shielding of 48.3 dB was achieved for EG/GE films at a film thickness of 43 mm [105].

Zhao et al. demonstrated that chiral carbon micro coils (CMC) have a higher microwave absorption than that of long CMC because of their interfacial multipoles that contribute to strong absorption

[106]. Du et al. investigated the EMI shielding characteristics of micro-coiled carbon fibers/paraffin in the frequency range of Ku band (12.4–18 GHz) [107]. It was observed that the attenuation constant value ranges from 135 to 165.6 m^{-1} with the increase of the frequency from 12.4 to 18 GHz. Su et al. investigated the EMI

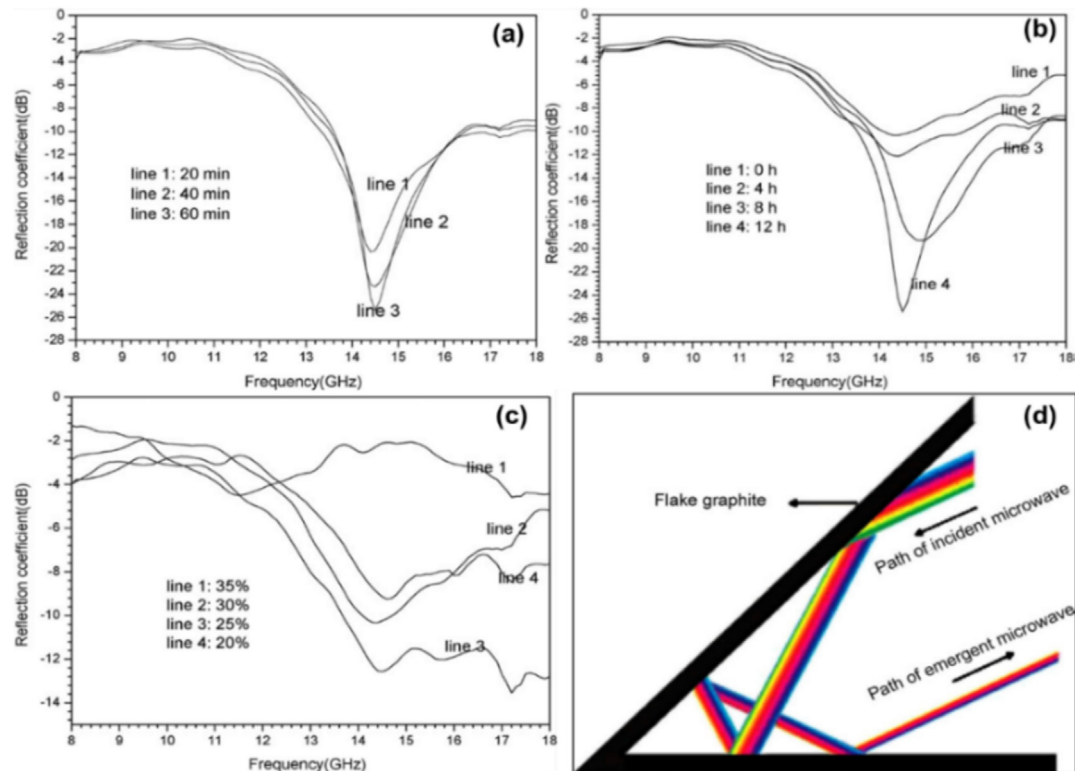


Fig. 22. (a) The absorption property of FG (weight ratio 30% and 12 h mechanical milling) with ultrasonic vibration treatment, (b) The absorption property of FG (weight ratio 30%) by mechanical milling, (c) The absorption property of FG with different weight ratios of FG and (d) A possible absorption mechanism for FG. Reproduced with permission from Ref. [43]. Copyright © 2008 Elsevier B.V. (A colour version of this figure can be viewed online.)

performance of onion-like carbon (OLC) loaded in the paraffin matrix in the frequency range of 8.2–12.4 GHz. The prepared nanocomposites exhibited a minimum RL of -42.04 dB at 9.02 GHz [60]. Jiang et al. achieved the RL exceeding -10 dB for 50% defective OLC/paraffin composites in the thickness range of 1.4–3.4 mm [61]. Maksimenko et al. investigated the EMI performance of OLC-PMMA thin films in the frequency range of 2–37 GHz [108]. Table 1 and

Table 2 summarize the EMI shielding performance and absorption properties of various carbon nanostructures and their composites, respectively.

5.1. Three-dimensional architecture of carbon materials

Besides carbon composites, three-dimensional structures such

Table 1
EMI shielding performance of nanostructured carbon materials and their composites.

Materials	Filler loading	σ (S.cm ⁻¹)	SE _T (dB)	SE _A (dB)	SE _R (dB)	d (mm)	Investigated Frequency range	Ref.
CNT macro-films	–	–	48–57	–	–	4×10^{-3}	40–60 GHz	[10]
GCF (Graphene-CNT)	20% (CNT)	2.7×10^{-3}	58–66	–	–	–	X band	[64]
NRMG-10	6.0%	0.061	42.3	–	–	1.8	X band	[174]
CNT Sponges	–	1.5–3.0 (varies with t)	54.8	54.1–54.5	0.3–0.7	1.8	X band	[175]
CNT/PDMS	1% (CNT)	–	46.3	45.8	0.5	2.0	X band	–
chitosan enriched graphene/iron pentacarbonyl flake	–	23.1	–38	–	–	0.3	8.2–59.6	[176]
Cellulose Fibre/GN aerogel	CF:GN = 2:1	0.1595	47.8	40.3	–	5.0	X band	[177]
Microcellular Polyimide (PI)/RGO/MWCNT Composite	8% (RGO&MWCNT)	18.7×10^{-3}	16.6	14.7	2.1	–	X band	[178]
CF/polyacrylamide/wood fiber (CPW) composite	7.5% (CF)	$\sim 10^{-3}$	41.03	–	–	–	X band	[179]
PVDF/PS/HDPE-MWCNT	1.6%	0.9×10^{-3} @ σ_c of 0.3%	31.7 @9.5 GHz	29.1 @9.5 GHz	2.6 @9.5 GHz	–	X band	[180]
GO-Fe ₃ O ₄	–	–	55	35	–	–	X band	[181]
GN aerogel-C texture	42 (GN)%	–	36–37	–	–	3.0	X band	[182]
MWCNT/waterborne polyurethane	10%	0.124	29	21.5	7.5	0.8	X band	[183]
Fe ₃ O ₄ /RGO ferrofluid composite	15% (RGO)	~ 0.1	41.20	34.23	~ 7	–	X band	[184]
Graphene/Fe ₃ O ₄ @PANI	–	–	–	22–26	4.7–6.3	2.5	X band	[185]
PPCP/MWCNT	4.6%	7.2×10^{-3}	47.88	42.5	5.4	2.0	X-band	[186]
Ni coated RGO/PC/SAN	3%	–	29.4	–	–	–	8–18 GHz	[187]
OMC/Silica	10%	$\sim 10^{-3}$	40.0	35	5	5.0	X-band	[188]

*X-band: 8–12 GHz.

Table 2
EMI Absorption properties of nanostructured carbon materials and their composites.

Materials	Absorber loading (wt.%)	Maximum RL (dB)	Frequency at Maximum RL (GHz)	Bandwidth range (GHz) RL < -10 dB	d @ RL Maxima (mm)	Ref.
Fe ₃ O ₄ /Graphene in paraffin	50	-40	6.8	4.6–18	4.5	[71]
Core-shell Co@C microspheres in paraffin	70	-68.7	10.6	2.7–18.0	1.65	[74]
Iron/nickel sulfide/CNT in Paraffin	20%	-29.58	14.8	–	2.0	[78]
EG in wax	14%	-27.6	–	5.6–10.4	4.0	[97]
Carbon nanosheets in wax	14%	-58	–	9.2–17.5	2.0	
BNCNT/Fe ₃ O ₄ in paraffin	–	-51.2	11.5	10.8–14.2 (<-20 dB)	5.0	[122]
GN/Fe ₃ O ₄ @Fe/ZnO	20%	-38.4	–	5.9–15.2 (<-20 dB)	5.0	[139]
CoNi/N-GN in paraffin	30%	-22 dB	10	3.6–18	2.0	[150]
Fe ₃ O ₄ /MWCNT in paraffin	50	-60.7	11	3.0–15.6	1.8	[189]
MoS ₂ /Fe ₃ O ₄ /Graphene	–	-45.8	5.9	4.6–9.7 & 15.7–18	2.5	[190]
Fe ₃ O ₄ /GNPs–NH–PANI	–	-40.31	–	7.85–17.47	2.6	[191]
GN-pFe ₃ O ₄ @ZnO in Paraffin	30%	-40.0	11.4	3.0–6.8 & 10.4–18.0	5.0	[192]
MWCNT/Fe ₃ O ₄ in Paraffin	30%	-18.22	12.05	–	2.0	[193]
yolk-shell C@C microspheres in paraffin	50%	-39.4	16.2	4.5–18.0 (<-20 dB)	2.0	[194]
N-GN/Fe ₃ O ₄ in paraffin	50%	-65.3	6.8	12–16	3.4	[195]
GN-PANI-Fe ₃ O ₄ in paraffin	50%	-43.9	11.4	5.4–16.4	2.5	[196]
RGO-Co ₃ O ₄	–	-43.7	13.8	3.6–5.4 & 12.3–15.1	3.3	[197]
Ni _{0.5} Zn _{0.5} Fe ₂ O ₄ /rGO	–	-47.8	10.7	6.6–18.0	2.8	[198]
ZnFe ₂ O ₄ /RGO in paraffin	30%	-29.3	16.7	15.4–18.0	1.6	[199]
Ni/PANI/RGO	–	-51.3	4.9	3.3 to 6.4	3.5	[200]
PANI-RGO-Co ₃ O ₄ in paraffin	50%	-32.6	6.3	3.4–11.8 & 12.9–18	3.0	[201]
PPy-RGO-Co ₃ O ₄ in paraffin	50%	-33.5	15.8	6.6–18.0	2.5	[202]
PPy-BaFe ₁₂ O ₁₉ /Ni _{0.8} Zn _{0.2} Fe ₂ O ₄ in paraffin	70%	-25.5	9.8	7.8–11.6	3.0	[203]
Ni _{0.8} Zn _{0.2} Ce _{0.06} Fe _{1.94} O ₄ /GN in paraffin	50%	-32.4	12.3	10.7–15.2	–	[204]
FeNi ₃ @SiO ₂ @RGO–PANI in paraffin	25%	-40.18	14.0	10.08–10.8 & 12.08–18.0	2.4	[205]
FeCo@SnO ₂ @GN@PANI in paraffin	30%	-39.8	6.4	4.6–7.7	3.0	[206]
RGO/CoFe ₂ O ₄ /MWCNT	–	-46.8	11.6	4.9–18	1.6	[207]
GN@Fe ₃ O ₄ @C@PANI in paraffin	25%	-44.2	11.4	9.7–15.5	3.0	[208]
N-GN@PANI nanorod in paraffin	25%	-38.8	7.3	6.5–8.8	3.0	[209]
rGO/MCNT/Fe ₃ O ₄	–	-36.0	13.44	6.5–17.9	2.0	[210]
GN@Fe ₃ O ₄ @PANI@TiO ₂ nanosheets in paraffin	50%	-41.8	14.4	7.0–8.5 & 10.2–16.2	1.4	[211]
FeCo@GNe@PPy in paraffin	30%	-40.7	5.7	3.1–6 & 12.8–15.6	2.5	[212]
rGO/ZnO in paraffin	15%	-54.2	15.2	11.4–18	2.4	[213]
Fe ₃ O ₄ /MWCNT/GN foam in paraffin	10%	-35.30	12.73	8.99–18.0	3.0	[214]
C/(C@CoFe) core–shell in paraffin	40%	-16.0	8.5	7.6–9.6	2.0	[215]
0.01 wt% of FGO and HFGO in NMP	–	-37.0	3.2	–	6.5	[216]
40%Ni/C Spheres in epoxy	–	-20.3	14.4	–	9.0	[217]
RGO–Ni _{0.5} Zn _{0.5} Fe ₂ O ₄	–	-47.8–	10.7	6.6–18.0	2.8	[218]
Cl/RGO/PVP in paraffin	50%	-27.59	6.88	4.2–18	2.5	[219]
Cl/RGO in paraffin	50%	-103.8	7.8	5.48–11.28	2.5	[219]
RGO-Flake Cl-PANI in paraffin	70%	-38.8	11.8	2.0–4.0	2.0	[220]
GN/PEDOT/CoFe ₂ O ₄ in paraffin	50%	-43.2	9.4	8.2–11.3	2.4	[221]
PPy/RGO aerogel in paraffin	15%	-54.4	12.76	10.20–16.96	3.0	[222]
ZnO NWs/RGO foam in PDMS	3.3%	-27.8	9.57	–	4.8	[223]
MnO ₂ /RGO in paraffin	50%	-37	16.8	13–18	2.0	[224]
Fe ₃ O ₄ /polypyrrole/carbon in epoxy	20%	-25.9	10.2	8.0–12.5	3.0	[225]
RGO/p-Fe ₃ O ₄ /PANI in paraffin	70%	-29.51	14.69	–	1.0	[226]
Cubic NiFe ₂ O ₄ /GN-PANI	–	-50.5	12.5	11.0–16.3	2.5	[227]
GN@CoFe ₂ O ₄ @ polyaniline in paraffin	50%	-47.7	14.9	12.3–18 (<10 dB) & 14–16 (<-20 dB)	1.6	[228]
GN/yolk shell-CoO@Co/ZnO in paraffin	20%	-51.1	11.3	9.5–14.2	2.6	[229]
Fe ₃ O ₄ /RGO in paraffin	30%	-22.7	~12	10.57–13.7	3.0	[230]
Urchin like Ni/RGO in paraffin	30%	-32.1	13.8	10.9–15.4	2.0	[231]
ALD Fe ₃ O ₄ /GN in paraffin	50%	-46.4	15.6	–	1.4	[232]
C coated Ni in paraffin	50%	-32	13	11.2–15.5	2.0	[233]
3D Fe ₃ O ₄ /CNT	–	-51	5.52	–	4.4	[234]
rGO-Tetrapod like ZnO in paraffin	15%	-59.5	14.43	11.2–18.0 (<-10 dB) & 13.2–15.6 dB (<-20 dB)	2.0	[235]

as foams, aerogel, hydrogel have attracted the attention because of their light weight and porous structure that attributes to the tuning of relative permittivity and favors impedance matching. Light-weight is very important and favorable for practical EMI shielding applications in the areas of aircraft, spacecraft, and automobiles because it would save materials and energy [109–113]. The

electrical and thermal conductivity of graphene-CNT hydrogel films increases with increasing the CNT weight percentage and reaches a maximum at 20 wt% of CNT due to the bridging of graphene by CNT. Beyond 20%, the decrease in the electrical and thermal conductivity is observed due to the CNT agglomeration. EMI shielding performance was improved from ~50 to ~60 dB for GCF with 20 wt% CNT

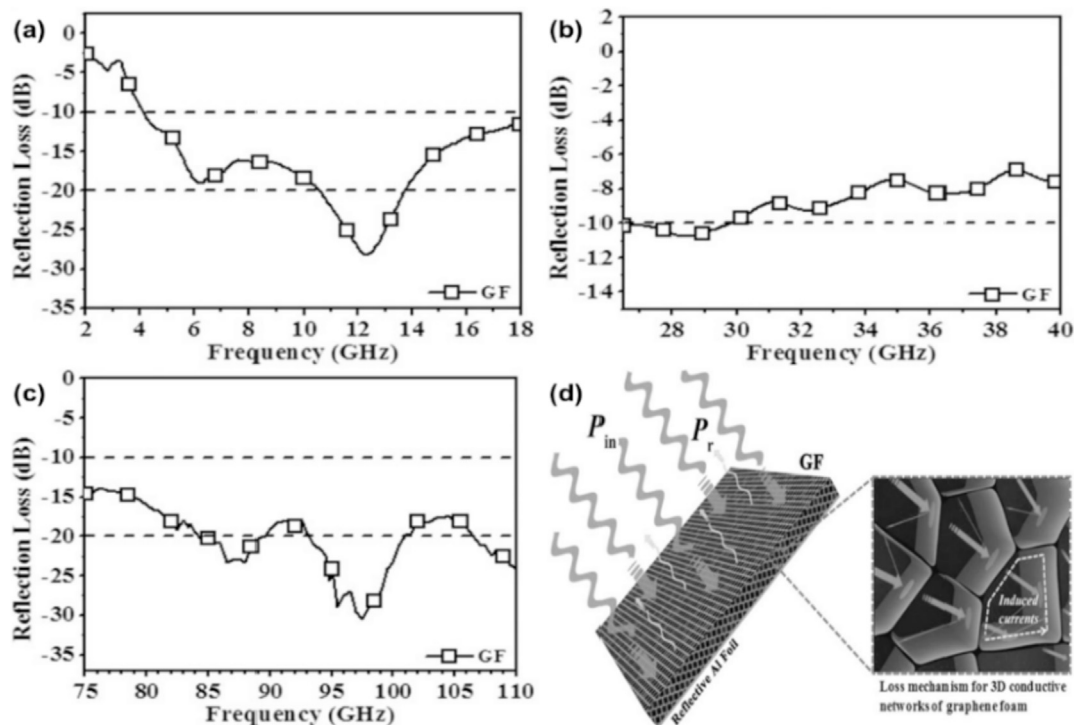


Fig. 23. The RL curves in the frequency range of (a) 2–18, (b) 26.5–40, (c) 75–110 GHz and (d) illustration of a mechanism for the improved microwave absorption for the graphene foam (GF). Reproduced with permission from Ref. [114]. Copyright © 2015 WILEY-VCH Verlag GmbH & Co. KGaA, Weinheim.

owing to the synergism of densification effect and bridge effect of the CNT [64].

Zhang et al. prepared graphene foam (GF) composed of numerous entwined graphene sheets. The total thickness of the graphene sheets is less than 5 nm [114]. The GF achieves $RL \leq -10$ dB in the frequency range of 4.1–18.0, 26.5–29.8 and 75–110 GHz (Fig. 23a–c). The higher performance of the GF results from the spontaneous and intense reaction of the entwined graphene layers of the GF towards the incoming electromagnetic radiation, as the extended resistance-inductance-capacitance circuits. The time-varying EM fields induce current on the cell walls and GF struts as shown in Fig. 23d [66,115]. These long-range stimulus currents get weakened in the resistive network and transformed into heat energy, which leads to the rapid degeneration of massive electromagnetic wave.

Integrated graphene aerogels (IGA) containing 0.22% of GO in polyamide (IDA0.22-2800), with a density of 18 mg cm^{-3} and σ of 1200 S m^{-1} presented an EMI shielding value of ~ 83 dB over the whole X-band frequency range and gave an ultrahigh specific EMI SE (SSE) of $4703 \text{ dB cm}^3 \text{ g}^{-1}$ [65]. For example, Song et al. demonstrated an excellent EMI SE of 47.5 dB in X-band for CNT-graphene hybrid foam, whose density and thickness were 0.0089 g cm^{-3} and 1.6 mm, respectively [76]. Shen et al. compared the EMI shielding performance between graphene foam and graphene film. In spite of its comparatively lower σ , graphene foam exhibited enhanced average EMI SE (~ 26.3 dB) than that of graphene film (~ 20.1 dB) in a broad frequency range of 8.2–59.6 GHz. This improved EMI shielding performance for GF was attributed from the internal multiple reflections at their cell-matrix interfaces [116]. Li et al. fabricated ultrathin carbon foams that exhibited the EMI SE of ~ 24 dB in the frequency range of 8–12 GHz at a thickness of $24 \mu\text{m}$. Also, it is demonstrated that SE values increased to 43 and 51 dB for 51 and 73 μm thick foams, respectively [117]. Wan et al. achieved good EMI shielding capacity of SE_{total} of about 58.4 dB along with

high σ of 19.1 S m^{-1} for GO/cellulose aerogel [118]. Zheng et al. achieved a higher EMI SE of 49.2 dB by preparing rGO/lignin-derived carbon (LDC) foams with thickness and density of 2.0 mm and 8.0 mg cm^{-3} , respectively [119].

Doping of heteroatoms to carbon materials has imparted a positive influence on their electronic and magnetic properties to the lightweight carbon materials [120,121]. For example, Zhang et al. demonstrated boron and nitrogen-doped CNT- Fe_3O_4 composites with a minimum RL of -51.2 dB at 11.7 GHz with a thickness of 5 mm. The RL less than -20 dB covers a wide frequency range from 3.5 to 18 GHz with the thicknesses of 1.5–5 mm for the prepared composites [122]. The chemical coupling of boron and nitrogen boosts the EM shielding activity of the prepared carbon nanostructure. Shahzad et al. [67] investigated the EMI performance of S-doped graphene laminates [112]. The EMI performance was found to be increased with increasing the annealing temperature and doping time. The maximum EMI SE of 33.2 dB was achieved at 0.14 mm. The excellent SE of the S-doped graphene results from increased σ and extra electron cloud contributed by sulfur atoms. The extra electron cloud interacts and disseminates the incoming EM radiation through the compactly piled corrugated graphene layers. Furthermore, polarization effects of the dipoles (which are formed due to the difference in electronegativity of sulfur and carbon) along with the defect polarization relaxation and group electronic dipole relaxation arise from oxygen and other residual defects in the graphene layer that enhanced the EMI SE. The above-mentioned mechanisms are illustrated in Fig. 24.

6. Temperature-dependent EMI performance of carbon nanostructures

Cao et al. investigated the high-temperature EMI performance of short carbon fiber (CF)/ SiO_2 in the frequency range of 8.3–12.4 GHz

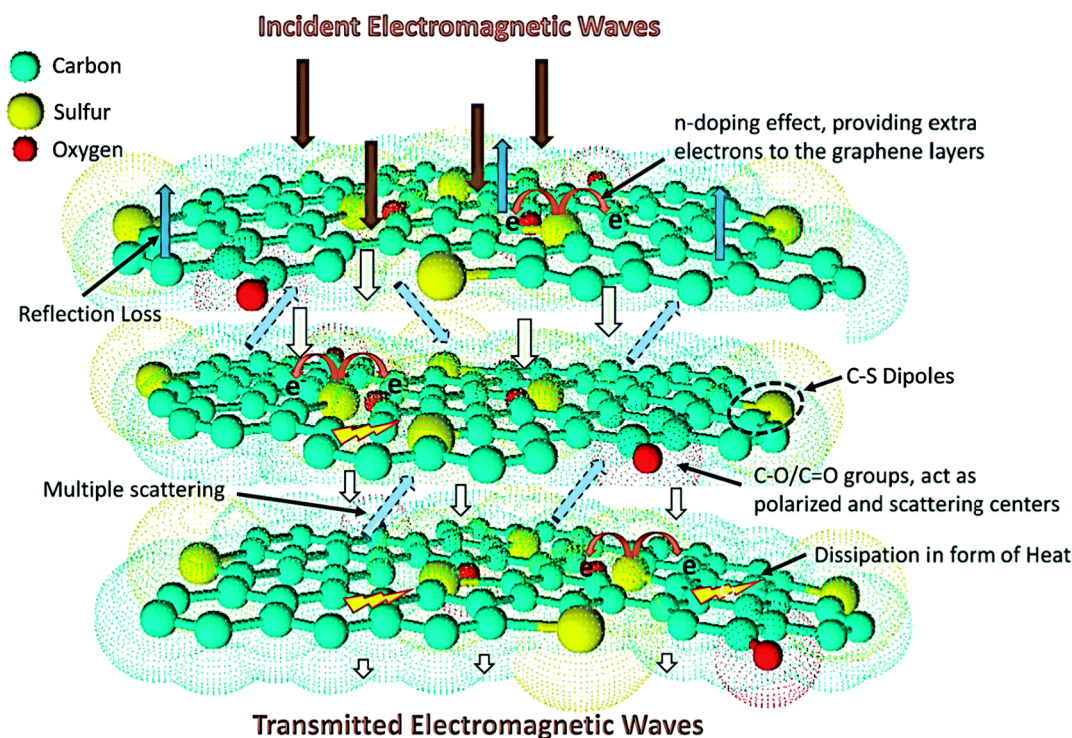


Fig. 24. Illustration for enhanced EMI shielding mechanism of S doped r-GO. Reproduced with permission from Ref. [67]. Copyright © The Royal Society of Chemistry 2015. (A colour version of this figure can be viewed online.)

[123]. To explore the temperature dependence of dielectric properties, the CF is considered to be composed of graphitic layers as illustrated in Fig. 25a, in which electronic transport took place by migration and hopping of electrons as shown in Fig. 25b [124,125]. The equivalent series circuit to explain these behaviors consists of two resistances connected in series as shown in Fig. 25c.

On the basis of the equivalent series circuit (Fig. 25c), the σ is given as [126,127];

$$\sigma^{-1} = \rho_{mig} + \rho_{hop} = \rho_o \exp \frac{E_g}{2kT} + \rho_h \exp \left[\left(\frac{T_o}{T} \right)^{\frac{1}{2}} \right] \quad (21)$$

where ρ_{mig} and ρ_{hop} are conductance of migrating and hopping electrons, respectively, ρ_o is the pre-exponential factor and ρ_h is the pre-factor of hopping electrons, respectively (influence of temperature on both the factors are negligible), E_g is the band gap, k is the Boltzmann's constant and T_o is the temperature constant. From the above equation, it is observed that the σ increases with increasing the temperature, which in turn would increase the ϵ'' of the composites. Along with the conductance loss, the increase in $\tan \delta$ owing to the skin effect also contributes to the EMI shielding. At 30 °C, the maximum absorption peak of about –10.22 dB occurs at 9.90 GHz and 600 °C, and the maximum absorption peak of about –10.22 dB occurs at 9.25 GHz. This indicates that the maximum absorbing peak slightly shifts towards lower frequency with increasing the temperature. It was observed that the values of both ϵ' and ϵ'' were enhanced with an increase in temperature which is attributed to electron polarization and σ , respectively, while decreased with increasing the frequency at each individual temperature. Cao and his co-workers also investigated the dielectric properties and EMI shielding performance of MWCNT/SiO₂ composites in the frequency range of 8.3–12.4 GHz, with respect to the temperature, frequency and filler content [128]. In this work, they proposed a circuit model for the MWCNT network and discussed the σ

dependency of temperature ($\sigma(T)$). $\sigma(T)$ depends on the concentration, geometric features and degree of the MWCNT cross-linking [129,130]. MWCNT can easily establish a conductive network in the insulator SiO₂ matrix due to their high aspect ratio. The migrating electrons (Fig. 26a) and hopping electrons (Fig. 26b) are two modes of electron propagation in MWCNT, as their layers are not parallel and imperfect [126,131,132].

The insulating silica creates the energy barrier (Fig. 26c) and it can be decreased by increasing the MWCNT content (Fig. 26d). The migrating and hopping electrons transport in the MWCNT network (Fig. 27a) can be represented as a series of parallel connection of migrating and hopping electronic transport in the MWCNT (Fig. 27b).

According to the percolation theory, the temperature dependence of σ can be written as [133]:

$$\sigma(T) \propto \sigma_1 (\phi - \phi_c)^t \quad (22)$$

which implies that $\sigma(T)$ increases with an increase in MWCNT content, which would also increase the ϵ'' of the composites. The conductivity of MWCNT (σ_{MWCNT}) increases with increasing the temperature, attributed to the thermally-assisted electron transfer between their shells at higher temperature [134]. According to the dielectric physics, contact conductivity ($\sigma_{contact}(T)$) of MWCNT is mainly decided by the hopping electrons as follows:

$$\sigma_{contact}(T) = \frac{K_h}{T} \exp - \frac{U}{k_B T} \quad (23)$$

where K_h is a pre-factor which is almost independent of temperature, U is the potential barrier and k_B is Boltzmann constant. As expressed by Equation (23), σ caused by the hopping electrons is also influenced by temperature. Since SiO₂ is an insulator matrix and transparent to EM wave, the σ of MWCNT network

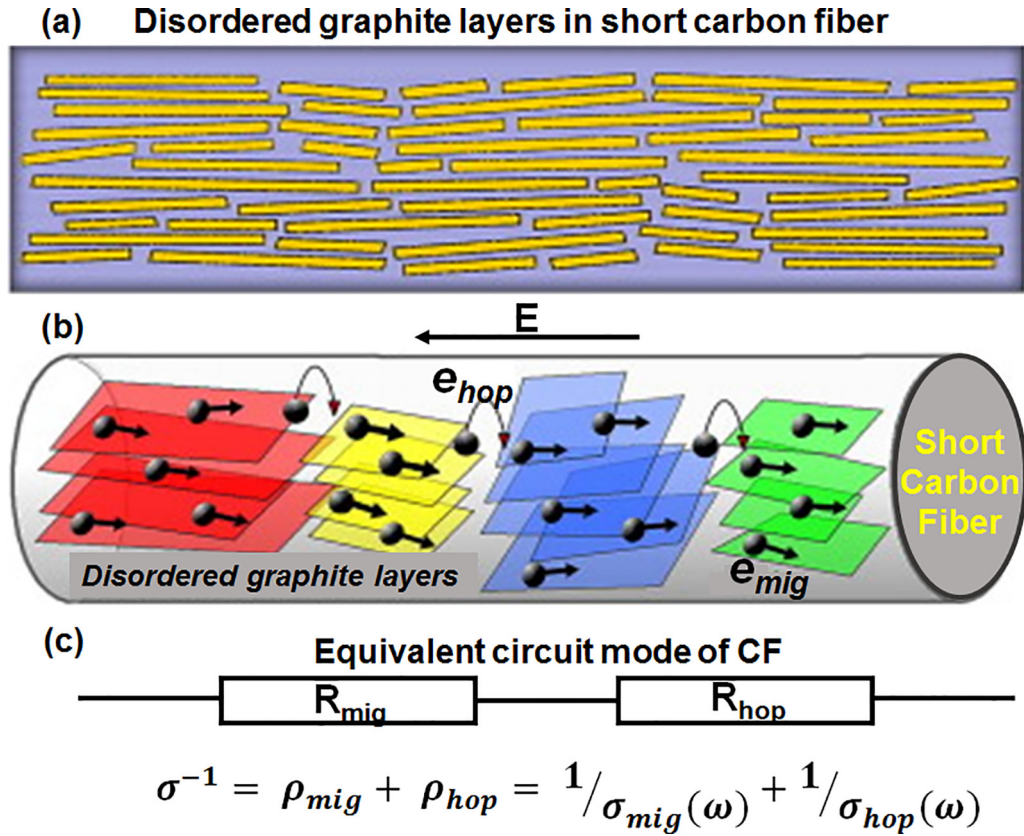


Fig. 25. Schematic illustration of (a) microstructure (b) electronic transport and (c) equivalent circuit of CF. Reproduced with permission from Ref. [123]. Copyright © 2009 Elsevier Ltd. (A colour version of this figure can be viewed online.)

($\sigma_{network}(T)$) plays the main role at higher filler concentrations. The equivalent circuit model of the selected MWCNT network (Fig. 27b) with different input/output is given as follows:

$$\sigma_{network}(T) = \frac{n \sigma_{MWCNT}(T) \times \sigma_{contact}(T)}{\kappa \sigma_{MWCNT}(T) + \sigma_{contact}(T)} \approx \frac{n}{\kappa} \sigma_{contact}(T) \quad (24)$$

where n is the number of MWCNT, κ is the selected parameter related to the input/output parameter of the MWCNT network, n/κ is in the range of $0 - n/(n-1)$. According to Equation (24), $\sigma_{MWCNT}(T)$ is much greater than $\sigma_{contact}(T)$ [135]. Thus, $\sigma_{network}(T)$ depends on the $\sigma_{contact}(T)$, which in turn depends on the hopping of electrons and temperature. The composites loaded with 10 wt% MWCNT perform an EMI SE of ~24.5 dB in the investigated range. The σ increases with increasing the MWCNT concentration which is beneficial for energy attenuation. But increasing σ increases the microwave reflection, which limits the EMI performance of composites at higher MWCNT loadings. Wen et al. demonstrated higher ϵ'' and EMI shielding performance for RGO/SiO₂ at the higher temperature. RGO/SiO₂ exhibited a maximum EMI SE of 38 dB at 473 K [136]. This higher performance is attributed to the combined effect of dipole polarizations and hopping electron transport.

7. Nanostructured carbon composites

In spite of their excellent properties, pristine carbon materials suffer from interface impedance mismatch due to insufficient σ and inadequate loss mechanisms for EM wave attenuation upon comparing with their composites [137–141]. One of the effective ways to overcome these limitations is the hybridization of carbon materials with other materials such as magnetic materials (such as

ferrites, magnetic metals and ferroelectrics), metal oxides, metal chalcogenides etc. By this way, optimal permittivity, permeability, σ , and thickness can be attained to achieve enhanced EMI performance. In this section, we discuss the carbon-based nanostructured composites.

7.1. Carbon/magnetic material nanostructures

Efficient EM impedance matching can be obtained by achieving a suitable balance between the ϵ_r and μ_r i.e. a suitable $\tan \delta_E$ and $\tan \delta_M$ is needed to obtain superior electromagnetic wave attenuation. The hybrids of magnetic materials such as ferrites, magnetic metals and ferroelectrics with carbon materials may provide a promising approach to couple the dielectric properties of carbon materials and magnetic properties of magnetic materials to tune the electromagnetic wave attenuation. In the carbon/magnetic materials-based composites, both $\tan \delta_E$ and $\tan \delta_M$ contributed to the energy consumption, resulting in an enhanced EMI shielding through absorption mechanism [142–144]. Along with dipole polarization and interfacial polarization, carbon materials with high aspect ratio and large specific surface area contributed to the $\tan \delta_E$ by creating a network to scatter the charges. The $\tan \delta_M$ was ascribed to the natural resonance, exchange resonance (usually occurs at a higher frequency relative to that of the natural resonance) and eddy current loss of the magnetic materials. Fig. 28 shows the illustration of the electron transport (Fig. 28a) in the carbon/magnetic nanocomposites and possible mechanisms which include dielectric loss (Fig. 28b) and magnetic loss (Fig. 28c&d), and multiple reflections [145]. Further, magnetic nanoparticles and carbon materials could regulate both the ϵ_r and μ_r , which is advantageous for the impedance matching [146]. The balance can be

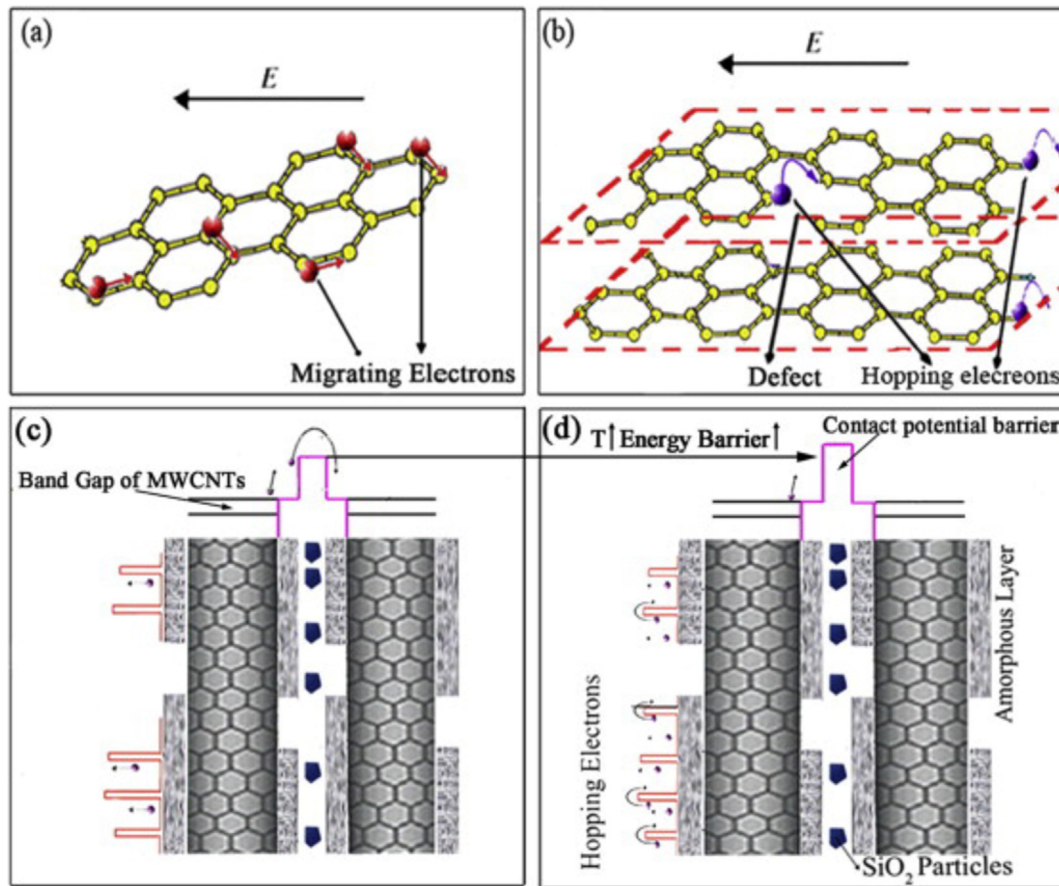


Fig. 26. Schematic illustrations of (a) migrating electrons transport in MWCNT layers, (b) hopping electrons transport in MWCNT layers; (c) hopping electrons transport in the composite and (d) hopping electrons transport in the composite at high temperature. Reproduced with permission from Ref. [128]. Copyright © 2013 Elsevier Ltd. (A colour version of this figure can be viewed online.)

obtained by varying the weight ratio between the dielectric and magnetic materials.

Hu et al. realized dielectric-magnetic coupled RGO-based EMI shielding materials with the uniform, high density and high-quality magnetic nickel ferrite (NiFe_2O_4) nanoparticles (NP) firmly anchored on graphene [148]. The $\text{NiFe}_2\text{O}_4/\text{RGO}$ exhibited S-shaped hysteresis curve which is the characteristics of superparamagnetic behavior. The $\text{NiFe}_2\text{O}_4/\text{RGO}$ were loaded into the paraffin wax and pressed into the toroidal shape of thickness ~ 2 mm to examine their microwave absorption performance. The mass ratio of $\text{NiFe}_2\text{O}_4/\text{RGO}$ was varied between 10 and 70 wt% at an interval of 10 wt%. It is demonstrated that two wide absorption bands with their peaks shifting towards lower frequency with an increase in mass ratio and thickness as shown in Fig. 29a&b. The minimum RL of -42 dB at ~ 6.6 GHz at $d = 5.0$ mm has been achieved with 70 wt% $\text{NiFe}_2\text{O}_4/\text{RGO}$ loaded samples at a thickness of 5.0 mm (Fig. 29a).

Wei et al. demonstrated the EMI SE performance of $\text{C@NiCo}_2\text{O}_4/\text{Fe}_3\text{O}_4$ composites exhibiting ferromagnetic behavior. The $\tan \delta_M$ are mainly caused by the eddy current loss in the frequency region of 4.5–18.0 GHz, C_o is not varying with the frequency (Fig. 30a). Cole-Cole plot (Fig. 30b) with four semicircles, which correspond to the multi-relaxation process, exists in the composites. The $|Z_{in}/Z_o|$ values for the $\text{C@NiCo}_2\text{O}_4/\text{Fe}_3\text{O}_4$ composites were close to 1 in the frequency range of 2.0–18.0 GHz, demonstrating good impedance matching by adding Fe_3O_4 (Fig. 30c). From Fig. 30d, it was observed that pure NiCo_2O_4 exhibited the highest attenuation constant, whereas the $\text{C@NiCo}_2\text{O}_4/\text{Fe}_3\text{O}_4$ composites

showed the lowest attenuation constant, which revealed that the impedance matching is the main contributor to the enhanced microwave absorption (MA) performance of $\text{C@NiCo}_2\text{O}_4/\text{Fe}_3\text{O}_4$ composites. The $\text{C@NiCo}_2\text{O}_4/\text{Fe}_3\text{O}_4$ exhibits a RL of -43.0 dB at 13.4 GHz with a thickness of 3.4 mm [75].

Li et al. investigated the EMI shielding performance of the $\text{FeCo}/\text{graphene}$ hybrid nanostructures obtained by chemically converting $\text{CoFe}_2\text{O}_4/\text{GO}$ hybrids because FeCo alloys exhibit large saturation magnetization, high Curie temperature and high σ than CoFe_2O_4 , which are more desirable for high-performance magnetic nanoparticle/graphene hybrid microwave absorbers [149]. Both $\text{CoFe}_2\text{O}_4/\text{GO}$ and FeCo/GO hybrids exhibit superparamagnetic behavior. The metallic nature of the FeCo alloy may also contribute to the improved permittivity of the FeCo/GN hybrids. The experimental relationship between matching thickness and frequency is shown in Fig. 31a. Fig. 31b displays the simulated plot between absorber thickness (t_m) versus peak frequency (f_m) obtained using Equation (22) (Quarter wave principle explained in section 3.7). It has been observed that the absorber thickness obtained from the simulated result matches well with experimental absorber thickness. Fig. 31c reveals the minimum RL of -40.2 dB obtained at a matching frequency of 8.9 GHz (blue solid curve), where the impedance was near to 1 (the black dashed curve) and the matching thickness was 2.5 mm on the simulated t_m vs f_m curve (Fig. 31b). These results indicate that the relationship between matching thickness and frequency for microwave absorption of FeCo/GN hybrids is in accordance with the Quarter wave principle.

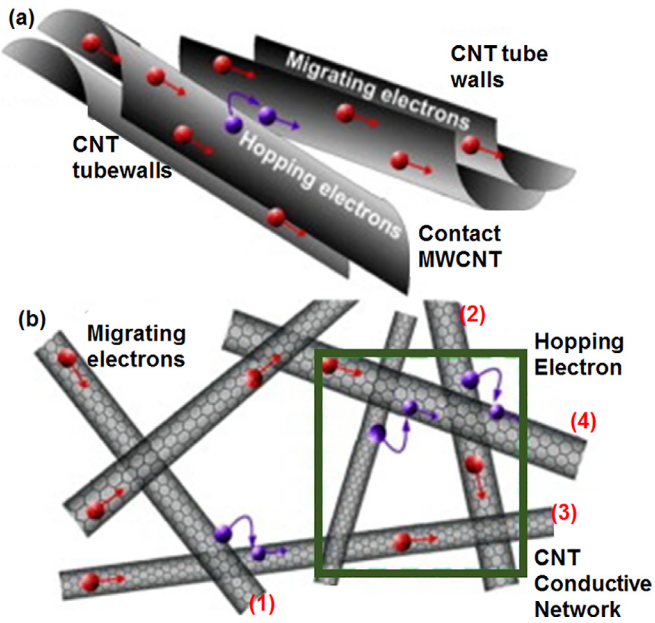


Fig. 27. Schematic illustrations of electron transport in (a) contact MWCNT and (b) MWCNT network. Reproduced with permission from Ref. [128]. Copyright © 2013 Elsevier Ltd. (A colour version of this figure can be viewed online.)

Feng et al. studied the microwave absorption performance of the CoNi/nitrogen-doped graphene hybrids loaded with paraffin wax (30 wt%:70 wt%). It was observed in Fig. 32a, that the value of C_o for CoNi nanocrystals and CoNi/NG hybrids varies with the frequency and exhibits two broadband at 5 and 12 GHz. Thus, their $\tan \delta_M$ is

mainly attributed to the natural resonance (band at 5 GHz) and exchange resonance (12 GHz), with little/no contribution from eddy current effect. It can also be observed that the $\tan \delta_M$ increased with the addition of N-doped graphene. Fig. 32b shows the Cole-Cole plot for CoNi, GO and CoNi/GO, wherein CoNi and GO exhibit only one semicircle, whereas CoNi/GO show three semicircles of Debye dipolar relaxation processes that contribute significantly to the enhanced $\tan \delta_E$. The ternary relaxation process is attributed from the relaxation at the interface between Co/Ni and N-doped graphene, relaxation of space charges accumulated at the interface, and relaxation of dipoles created from the reduction and N-doping process of GO. A maximum RL value of -22 dB was achieved for the CoNi/N-doped graphene hybrid/paraffin composites at about 10 GHz with a matching thickness of 2.0 mm [150].

Wu et al. investigated the EMI SE performance of elliptical $\text{Fe}_3\text{O}_4/\text{C}$ core-shell nanorings (NR). It has been observed from Fig. 33a–c that the values of ϵ' and ϵ'' vary monotonically with respect to carbon content. The values increase with respect to carbon content up to 17.25% and then decreases, similar to the insulating metal oxides, indicating the amorphous nature of carbon shell. But, this behavior is different from the reported $\text{Fe}_3\text{O}_4/\text{C}$ core-shell microspheres [151] and nanospindles [152], where the values of the above parameters increase with increasing the carbon content. The difference in the trend was ascribed to the differences in their graphitization degree and constrained paths for electron oscillations and the geometric area inside nanorings. The values of μ' and μ'' show a slight increase at 5–18 GHz with increasing the carbon content, whereas the $\tan \delta_M$ values decrease with increasing the carbon content (Fig. 33d–f). The $\tan \delta_M$ exhibits multi-resonance behavior at lower carbon content, which is absent at higher carbon content. In the core-shell structures, surface charges accumulated at the interfaces between two different dielectric

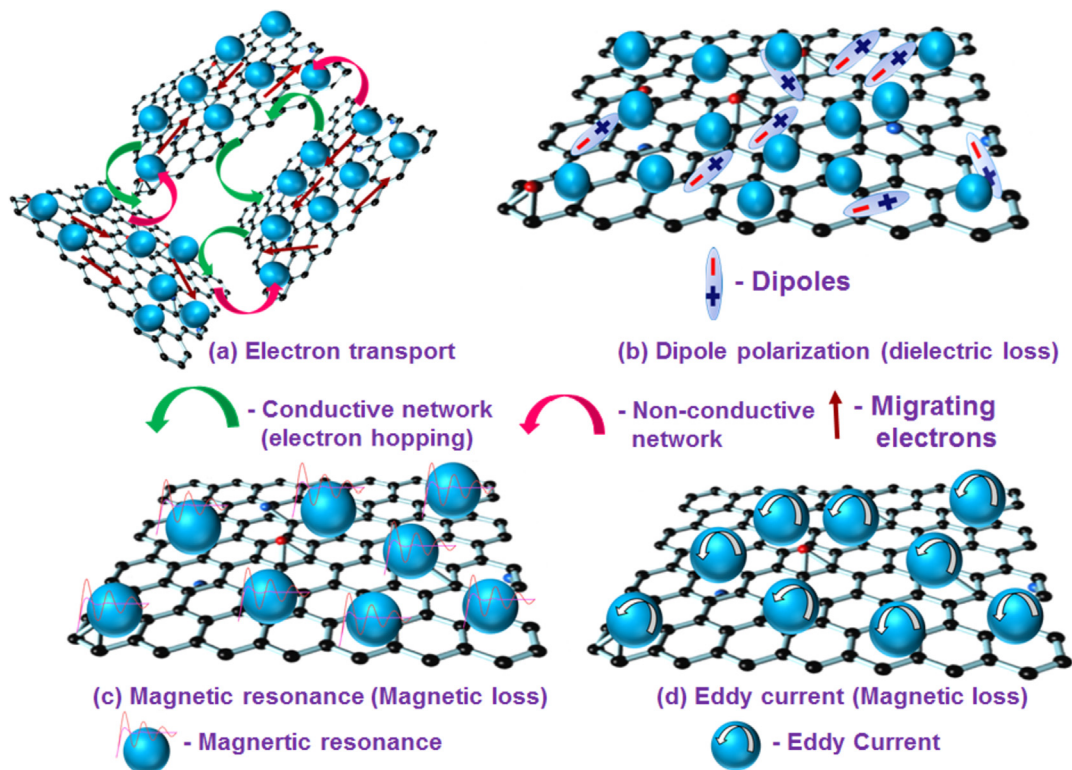


Fig. 28. Schematic illustrations of (a) electron transport, (b) dipole polarization, (c) magnetic resonance and (d) magnetic eddy current in carbon/magnetic nanocomposites. Modified from Ref. [147]. (A colour version of this figure can be viewed online.)

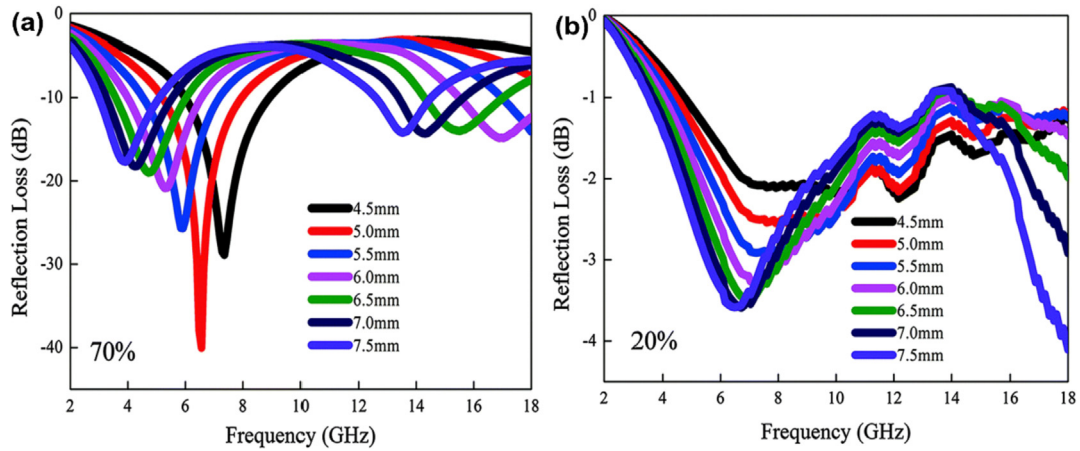


Fig. 29. Microwave absorption of NiFe₂O₄/RGO loaded paraffin as a function of mass ratio and thickness. Reproduced with permission from Ref. [148]. © The Royal Society of Chemistry 2016. (A colour version of this figure can be viewed online.)

media give rise to a Debye-like relaxation process under an alternating EM field. The lag of induced charges that counters the external applied field results in relaxation and transforms EM energy to heat energy (Fig. 34). The minimum RL of -55.68 dB is achieved by Fe₃O₄/C NR containing 11.95 wt% of carbon [73].

Fig. 35 depicts the relation between the RL and the frequency for the Co@C nanocapsules in paraffin matrix at an absorber thicknesses of 1, 2, 3, 4 and 5 mm. The absorber provides great

performances with increasing the wt.% of Co@C nanocapsules, with a minimum RL of -56.3 dB for the 50 wt% loading at 12.1 GHz [153].

Zhan et al. prepared Fe₃O₄ nanoparticles decorated polydopamine modified 3D carbon fiber mat. Its electromagnetic shielding performance was investigated at different weight ratios between 3D carbon fiber mats and iron source as 1:1, 1:3, and 1:5. The 3D carbon fiber mats/Fe₃O₄ hybrid (1:3) exhibited excellent microwave absorption with the lowest RL of -47 dB at 10.0 GHz [154].

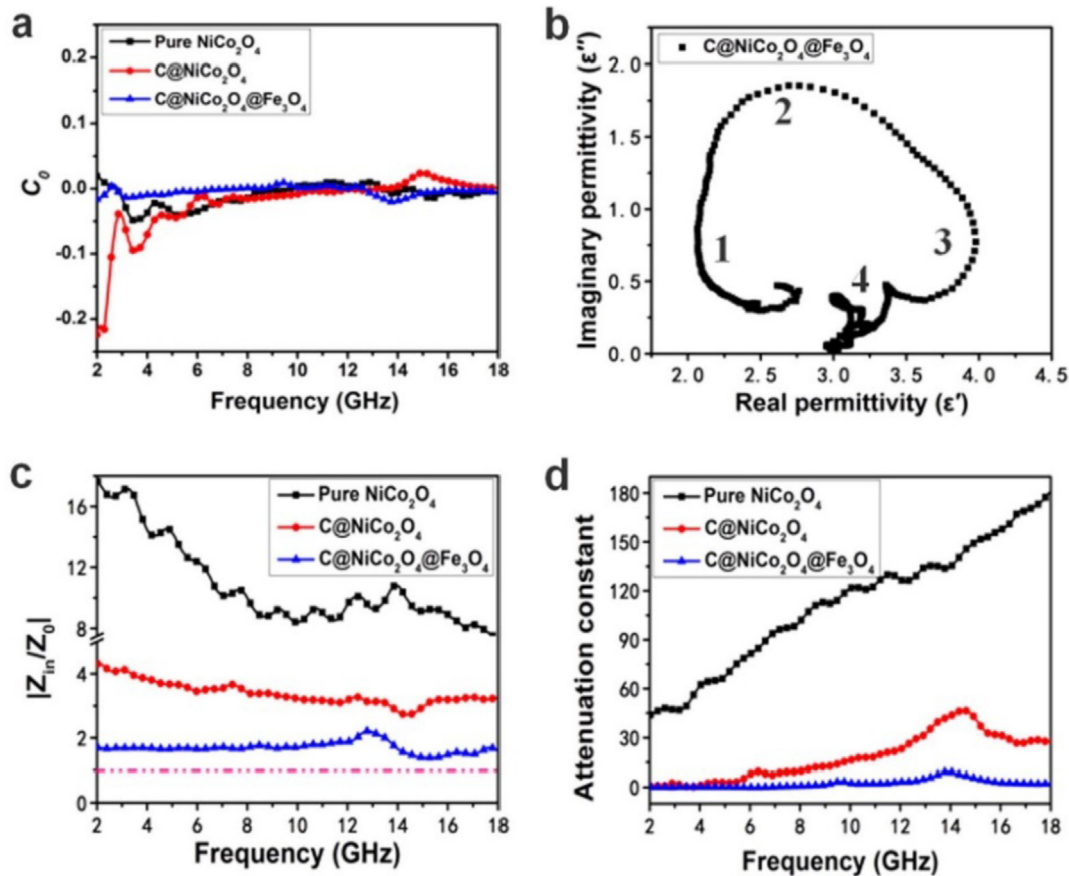


Fig. 30. (a) Values of C_0 vs frequency for pure NiCo₂O₄, C@NiCo₂O₄, and C@NiCo₂O₄@Fe₃O₄. (b) The relationship between ϵ' and ϵ'' (Cole-Cole plot) of C@NiCo₂O₄@Fe₃O₄ composites. (c) Impedance matching and (d) attenuation constant α of pure NiCo₂O₄, C@NiCo₂O₄ and C@NiCo₂O₄@Fe₃O₄. Reproduced with permission from Ref. [75]. Copyright © 2016 Elsevier B.V. (A colour version of this figure can be viewed online.)

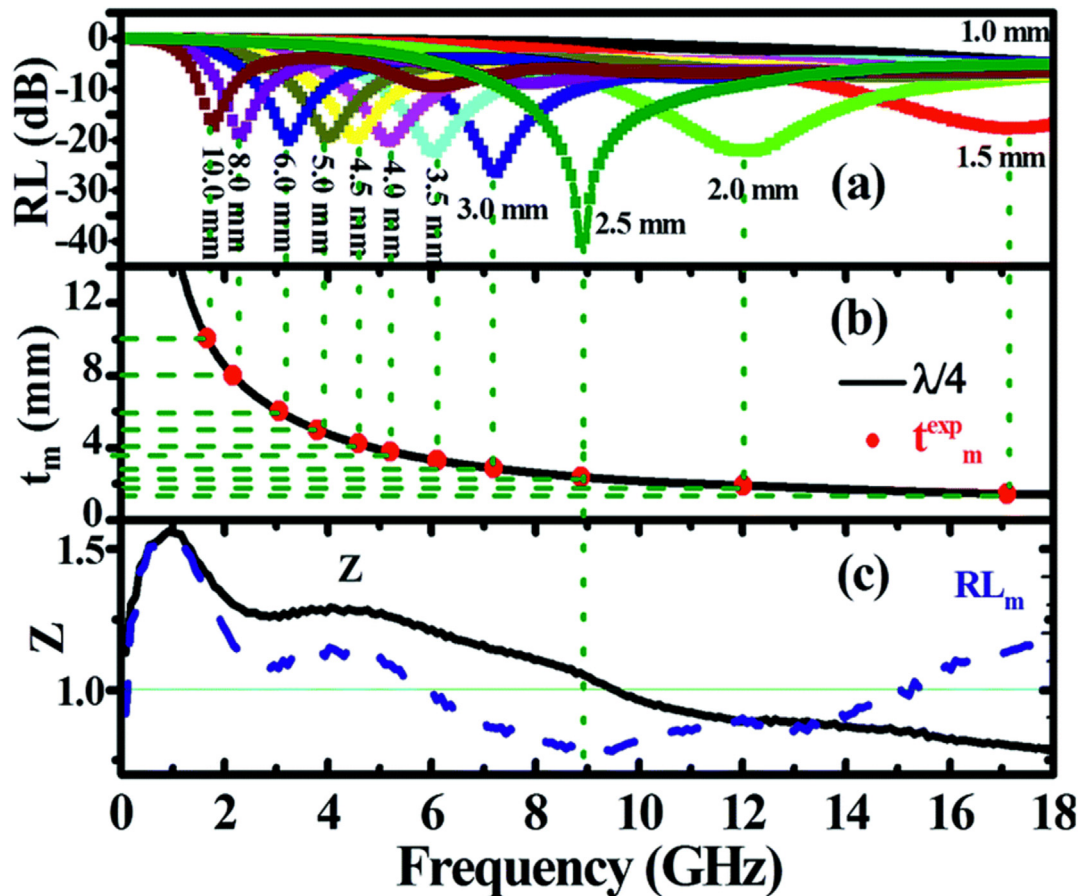


Fig. 31. (a) Frequency dependence of RL values for twelve different thicknesses; (b) simulations of the absorber thickness (t_m) versus peak frequency (f_m) under $\lambda/4$ conditions; and (c) modulus of the normalized input impedance ($|Z_{in}/Z_0|$) for 50 wt% of FeCo/GN hybrid loaded paraffin. Reproduced with permission from Ref. [149]. Copyright © The Royal Society of Chemistry 2015. (A colour version of this figure can be viewed online.)

Wang et al. prepared Fe_3O_4 clusters-nitrogen doped graphene and demonstrated a minimum RL of -53.6 dB at a thickness of 1.8. Further by varying the ratio of graphene in the composites, absorption covering $\sim 60\%$ of the investigated frequency range has been achieved [147]. Li et al. reported S-doped Fe@C nanocapsules synthesized by an arc-discharging approach, in which the graphitic shells were in-situ doped with substitutional sulfur atoms. Further, their electromagnetic performances were tuned by the sulfur substitutions. From the experimental and theoretical results, the sulfur substitutions in graphitic layers gave rise to a local structural asymmetry and resulted in the formation of a permanent electric dipole, which contributed to the high EMI SE [77].

From the above discussion, the combination of $\tan \delta_E$ and $\tan \delta_M$ contributed to the low reflection and high absorption in the carbon/magnetic material composites. The main reason for this phenomenon is a balance between ϵ_r and μ_r in the composites. The $\tan \delta_E$ and $\tan \delta_M$ along with the interfacial polarization that arises from the strong interface between magnetic and carbon material lead to the low reflection and high absorption of penetrated EM radiation. The incorporation/hybridization of magnetic material with the carbonaceous material reduced the ϵ'' and increased the μ'' of pure carbon materials, thereby improving the impedance matching. However, the increase in the amount of either magnetic or carbon material results in poor EMI performance due to the agglomeration of materials, impedance mismatch, etc. Tailoring the weight ratio between the carbon and magnetic materials in the composites could attribute to the advantages of relatively low

density, thin matching thickness, strong absorption performance, higher absorption bandwidth and anti-oxidation.

7.2. Carbon/Metal oxide nanostructures

The metal oxide/carbon composites could be a potential candidate in the field of EMI shielding due to their light weight, ability to perform in the harsh environment and their semiconducting properties. The immobilized metal oxides can contribute to the polarization arising from the carbon-metal oxide interface, metal oxide-metal oxide interface, and defect dipole at oxygen vacancies. Drakakis et al. prepared ZnO nanopowder/graphene nanoplatelets based composite layers with a thickness of around 900 nm deposited on 16 cm by 16 cm foam board by brushing paint-like dispersions in deionized water. The respective attenuation values are between -30 dBs (at 10 GHz) and -38 dB (at 20 GHz) [155]. Lu et al. analyzed the EMI performance of ZnO nanocrystals decorated MWCNT loaded in SiO_2 matrix [156]. The ZnO/MWCNT were prepared by mild solution process as illustrated in Fig. 36(left). The 2.5 mm thick ZnO/MWCNT- SiO_2 sample exhibited a minimum RL of -20.7 dB, which is 2.5 times higher than that of MWCNT- SiO_2 . The polarization of ZnO and capacitor-like structures formed at the interfaces between ZnO and MWCNT enhanced the EMI performance in addition to hopping and migrating electrons of MWCNT, as illustrated in Fig. 36(right).

Liu et al. investigated the influence of mass ratio between ZnO nanowhiskers and CNT on the EMI performance. It has been

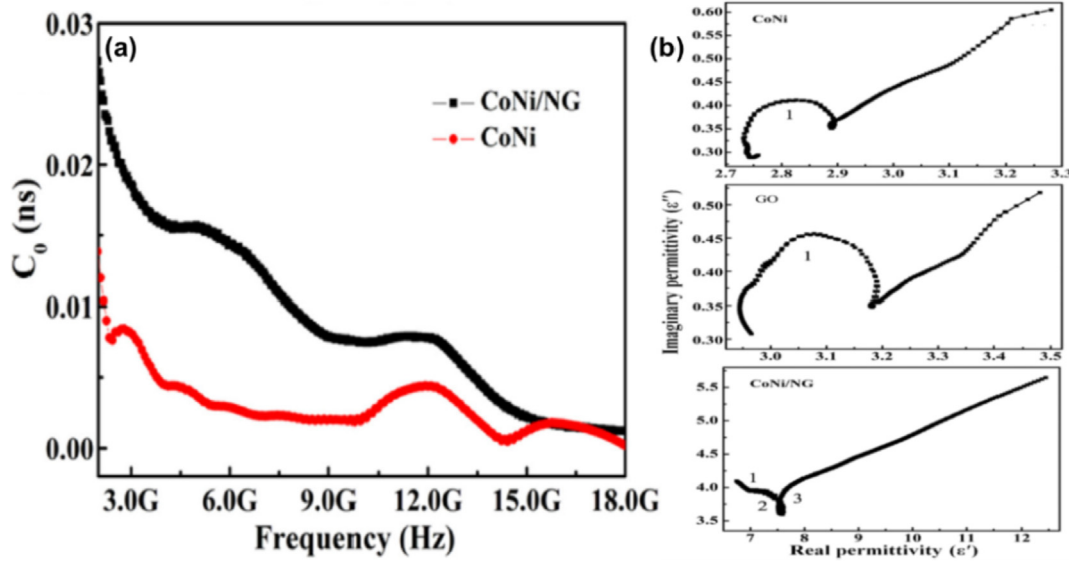


Fig. 32. (a) C_0 values as a function of frequency and (b) Cole-Cole plot (ϵ'' versus ϵ') for CoNi nanocrystals, GO and CoNi/NG hybrids. Reproduced with permission from Ref. [150]. Copyright © 2016 Elsevier Ltd. (A colour version of this figure can be viewed online.)

observed that CNT mixed with 10 wt% ZnO has the optimum reflection loss of -37.03 dB at a sample thickness of 2.0 mm, with the bandwidth more than 4.04 GHz for RL below -10 dB [157]. Qin et al. demonstrated that carbon black (CB)/tetrapod-like ZnO (T-ZnO)/epoxy resin (EP) composites containing 10% T-ZnO whiskers mixed with 7% CB exhibiting a minimum RL of -17.36 dB at 10.35 GHz, and the bandwidth under -10 dB of 4.25 GHz [158]. The ternary composite composed of RGO, Cu_2O and Cu quantum dots synthesized at room temperature by using NaBH_4 as reducing agent

under mild wet-chemical conditions achieved a maximum RL of -51.8 dB at 14.6 GHz and the bandwidth corresponding to RL at -10 dB reached 4.1 GHz (from 12.1 to 16.2 GHz) with a thickness of only 1.3 mm [159].

7.3. Carbon/metal chalcogenide (MC) nanostructures

A good absorber should have both excellent impedance matching at surface and favorable attenuation capabilities due to

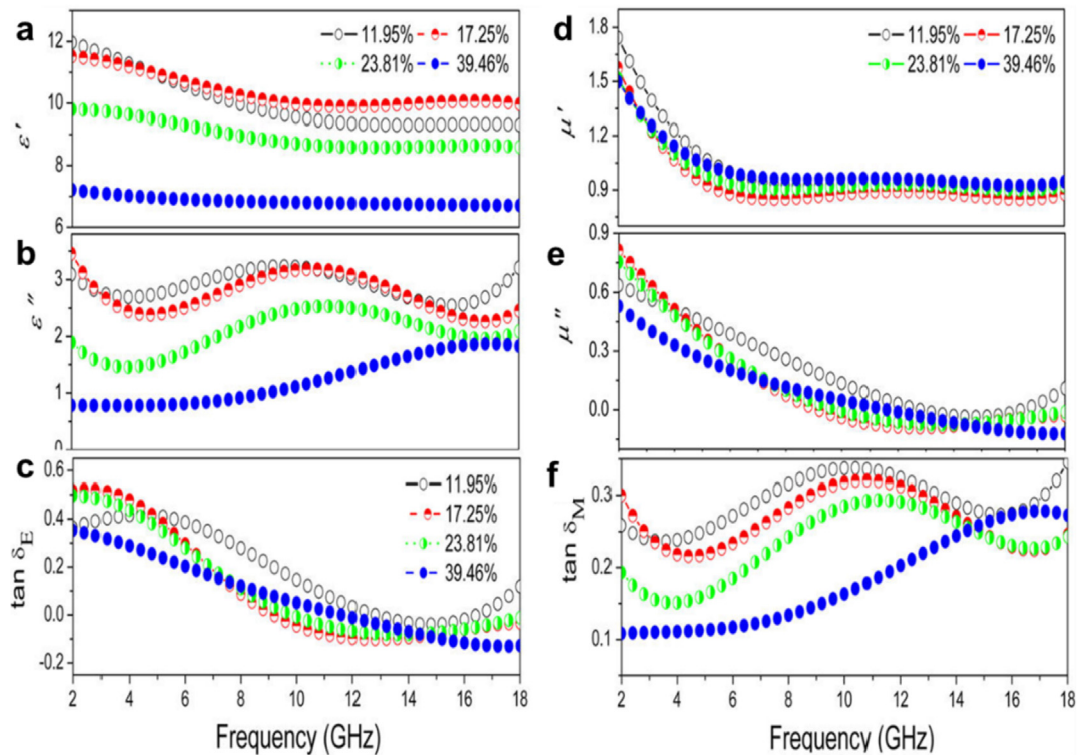


Fig. 33. Electromagnetic parameters (a) ϵ' (b) ϵ'' (c) $\tan \delta_E$ (d) μ' (e) μ'' and (f) $\tan \delta_M$ as a function of carbon content and frequency, for 60 wt% $\text{Fe}_3\text{O}_4/\text{C}$ NR loaded wax. Reproduced with permission from Ref. [73]. Copyright © 2016 American Chemical Society. (A colour version of this figure can be viewed online.)

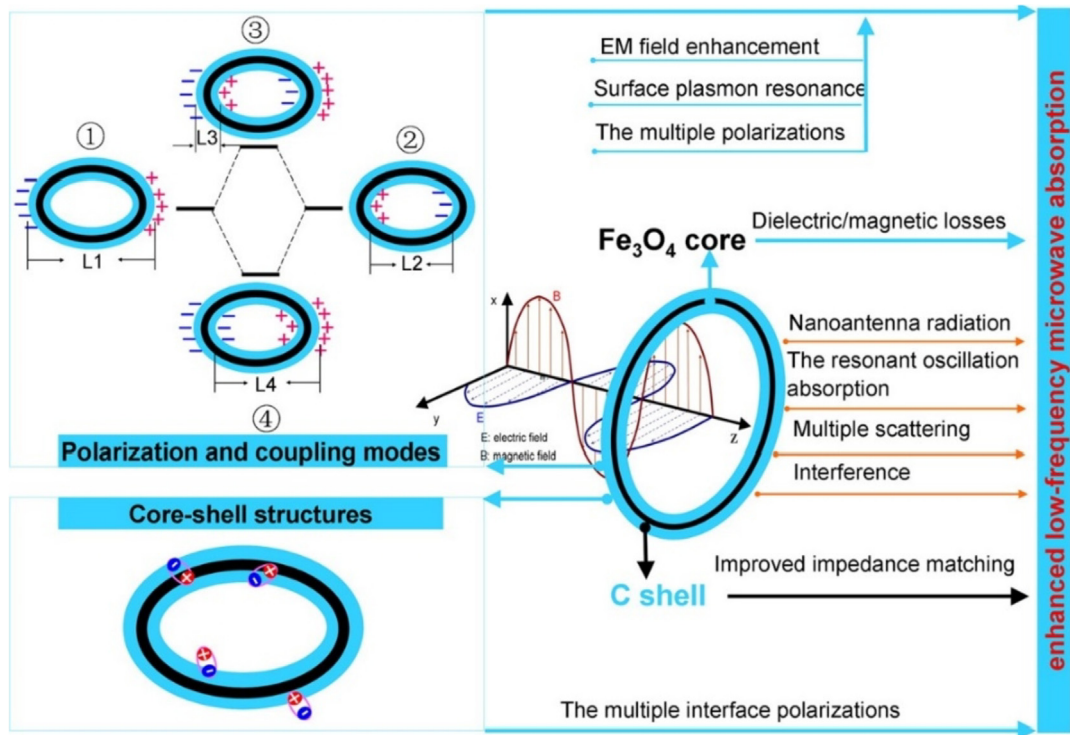


Fig. 34. Polarization, coupling, and absorbing mechanisms of $\text{Fe}_3\text{O}_4/\text{C}$ core-shell NR. Reproduced with permission from Ref. [73]. Copyright © 2016 American Chemical Society. (A colour version of this figure can be viewed online.)

the following reasons, (a) excellent impedance matching can decrease the reflection of an absorber at its surface, and if that material has poor attenuation ability, the EM waves entering the material will be reflected and transmitted out of the absorber. (b) Conversely, if the impedance matching at surface for an absorber is poor, its strong attenuation ability has no meaning for the rarely-entered electromagnetic waves. Carbon/MC composites have

received a great deal of attention to tune the impedance matching degree and attenuation capability because of their optical, electrical and mechanical properties, relatively lower ϵ'' (due to a decrease in σ upon addition of MC) and good structural carbon-TMCs interface that contributed to dielectric relaxations (interfacial polarization).

Zhang et al. prepared graphene-CdS (G-CdS) nanocomposites and investigated their EM wave absorption performance with

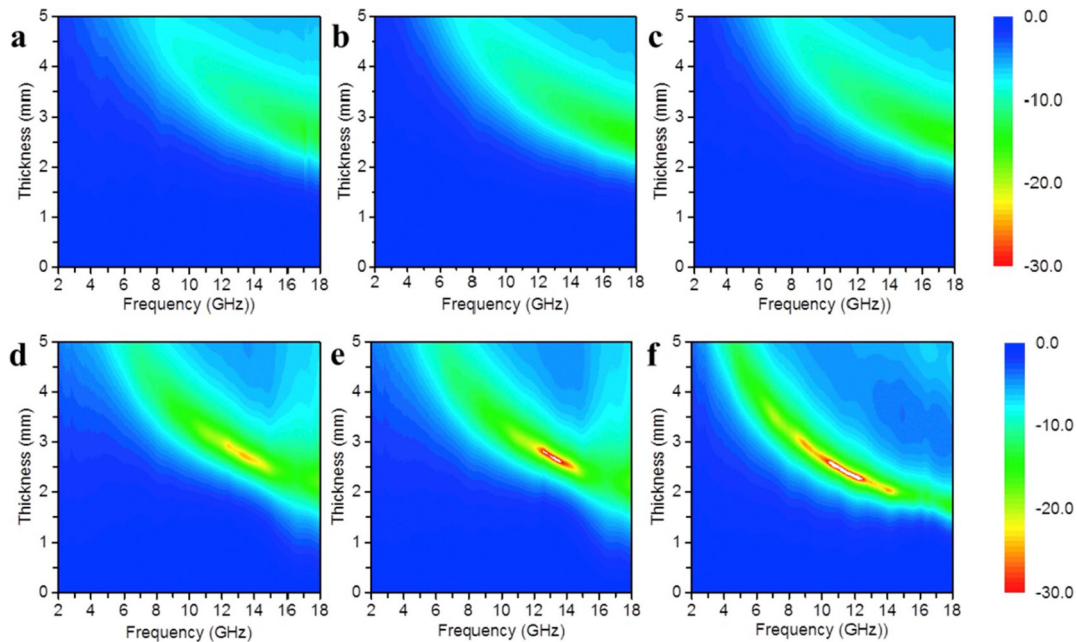


Fig. 35. (a) 3D plot of microwave absorption performance of paraffin and (b–f) the Co@C nanocapsules in paraffin based composites (10 wt%, 20 wt%, 30 wt%, 40 wt%, 50 wt%, respectively). Reproduced with permission from Ref. [153]. Copyright © 2017 Elsevier B.V.

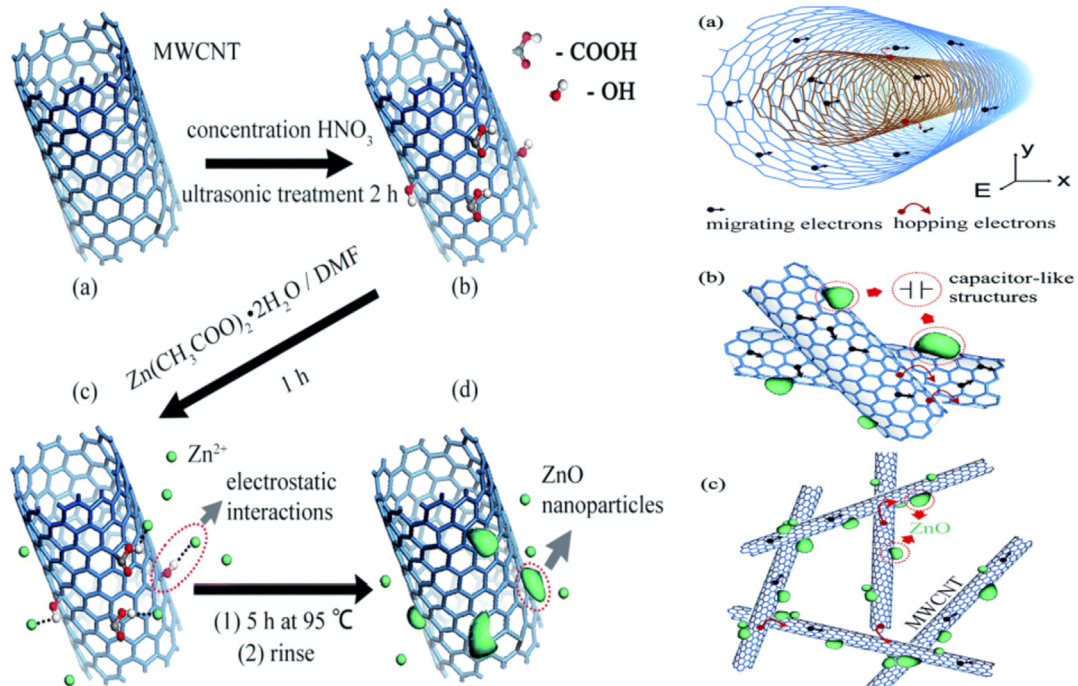


Fig. 36. Schematic illustration of the preparation of ZnO/MWCNT (left) and electronic transport in (a) an MWCNT; (b) two neighboring ZnO/MWCNT; (c) a conductive network of the ZnO/MWCNT in the SiO₂ matrix (right). Reproduced with permission from Ref. [156]. Copyright © The Royal Society of Chemistry 2014. (A colour version of this figure can be viewed online.)

respect to filler loading of G-CdS nanocomposite in paraffin with a weight ratio of 1:10. The $\tan \delta_M$ factors for the G-CdS nanocomposites are very low. Therefore, the microwave absorptions of the G-CdS nanocomposites result mainly from $\tan \delta_E$ rather than $\tan \delta_M$. The Cole-Cole plot of G-CdS nanocomposite presents a clear segment of three overlapped semicircles representing three triple dielectric relaxation processes. Each semicircle corresponds to a Debye dipolar relaxation. In addition to multiple scattering and electric polarization arising from defects and dangling bond of graphene, interfacial relaxation is present because of a good structural graphene-CdS interface. Therefore, the interfacial multipoles contribute to the enhanced absorption of the G-CdS/paraffin composites. The G-CdS nanocomposites achieved a RL below -10 dB in the frequency range of 5.2–18 GHz when adjusting the thicknesses from 2 to 5 mm, which was mainly ascribed to the proper electromagnetic matching of the CdS nanoparticles and graphene sheets, and the triple dielectric relaxations [160]. The Cole-Cole curve of hollow α -MnS spheres-RGO hybrid (MHS-RGO)/wax exhibited two semicircles which represent the contribution of the Debye relaxation process to the enhanced dielectric properties of MHS-RGO composite. MHS-RGO composite not only exhibits a larger RL (-52.2 dB at 10.72 GHz) but also a wider absorption band (less than -10 dB from 7.6 to 18 GHz) in a frequency range of 2–18 GHz [72]. Wang et al. prepared MoS₂/RGO hybrids and investigated their EM wave absorption performance for the first time [161]. Fig. 37 shows the Cole-Cole plot of the MoS₂/RGO-wax with many distinct semicircles representing their multi-relaxations dielectric properties. The polarizations arose from the defect of MoS₂ and RGO, the oxygen functional groups and electrons accumulated at the interface (as illustrated in Fig. 38) led to this multi-relaxation dielectric property. 10 wt% of MoS₂/RGO hybrid loaded in a wax matrix exhibited an effective absorption bandwidth of 5.72 GHz at thicknesses of 1.9 and 2 mm.

Dang et al. prepared 3-D RGO-MoS₂ nanosheets and demonstrated that the electromagnetic wave absorption varied with

varying the mass ratio between the RGO and MoS₂ [162]. At the mass ratio of 1:3, RGO/MoS₂ hybrids with 10 wt% filler loading in paraffin matrix exhibited a RL of -31.57 dB with an effective absorption bandwidth (RL < -10 dB) of 5.92 GHz at a thickness of 2.5 mm. 20 wt% of Ni₁₇S₁₈/Fe₇S₈ encapsulated CNT loaded in paraffin exhibited a RL of -29.58 dB at the matching thickness of 2.0 mm, and the effective bandwidth corresponding to the RL < -10 dB is 5.58 GHz [78]. Quan et al. prepared flower like MoS₂ and MoS₂/RGO composites with different combination ratios to obtain an optimal EM wave absorbing property. Three typical MoS₂/RGO composites were prepared with 4, 6, and 8 mL GO, which are represented as M₁, M₂, and M₃, respectively. The impedance matching ratio value of the prepared samples shows decreasing trend with increasing the RGO content ($Z_{M1} > Z_{M2} > Z_{M3}$), while the attenuation constant follows an increasing trend ($\alpha_{M3} > \alpha_{M2} > \alpha_{M1}$) in all frequency ranges as shown in Fig. 39a. As discussed earlier in this section, M₂ could serve as a good absorber since it possesses an optimal impedance matching as well as favorable attenuation ability. M₂ exhibits a RL of -67.1 dB at 14.8 GHz with a small thickness of 1.95 mm and effective bandwidth of about 5.92 GHz. Fig. 39b shows that the experimental thickness is consistent with the simulated thickness [163].

8. Carbon-based multi-layered nanostructures

By judicious choice of various material design parameters, such as the chemical nature of the matrix, the nature and thickness of the core and skin, and the ratio of core to interlayer thickness, there is sufficient versatility for making multilayer structures. The GN, polymers, carbon fiber fabrics, materials with $\tan \delta_E$ and $\tan \delta_M$, and very fine aluminum and copper meshes have been used as sandwich components. Multilayer material for graded σ is expected to decrease the RL [164].

Song and co-workers fabricated GN based sandwich structure using the poly (ethylene-vinyl acetate) polymeric dielectric spacers

(D) [165]. The inset of Fig. 40a shows the transportation of electromagnetic wave at the graphene/air interface. It is observed that the electrically conductive graphene reflected the incident electromagnetic waves partially. The D-GN-D sandwich structure comprising single layer of graphene (Fig. 40a) exhibited lower EMI performance (Fig. 40d) than that of two and three layered structures, i.e., GN-D-GN (Fig. 40b) and GN-D-GN-D-GN (Fig. 40c), respectively. The two/three-layer sandwich structures exhibited a higher EMI SE at around 11 GHz (Fig. 40d). It implies that the frequency selective EMI shielding can be achieved by two/three-layer structures. Fig. 40f&g depicts that absorption is dominant in overall shielding mechanism. However, GN-D-GN-D-GN exhibited a reduced EMI SE peak than the GN-D-GN. The reduced SE observed for GN-D-GN-D-GN is due to the altered impedance condition and the interruption in resonance formation by inserted GN layer.

Four different sandwich structures, i.e., GO-D-GO (Fig. 41a), GN-D-GN (Fig. 41b), GO-D-GN (Fig. 41c), GN-D-GO (Fig. 41d) were fabricated to demonstrate the frequency selectivity of the fabricated sandwich structures. It can be observed that the effective absorption bandwidth is different for each sandwich structure, indicating their frequency selectivity based performance for electromagnetic radiation (Fig. 41e–g). This difference in the EMI performance is due to impedance mismatching and frequency selectivity at GN-air interfaces.

Further, the effects of different spacers on the EMI shielding performance were investigated by comparing the EMI SE of GN-D-GN sandwich structures with the sandwich structures consisting of different spacer materials such as spacer with dielectric loss (RGO coated polymeric textile-RGO (1)D & RGO (2)D) and spacer with magnetic loss ($\text{Fe}_3\text{O}_4(1)\text{D}$ & $\text{Fe}_3\text{O}_4(2)\text{D}$). The sandwich structure consisting of magnetic loss material (Fe_3O_4) as spacers exhibited higher EMI SE than that consisting of dielectric loss material (RGO coated polymeric textile) as spacer (Fig. 42a&b). The shift in the

peak frequency (Fig. 42a&b) is observed between the sandwich structures which should be attributed to the deviations in wavelength and velocity and the solid-air interfaces.

They also reported hydro-sensitive smart sandwich structures with self-adaptable EMI shielding ability by constructing non-woven (NW) polypropylene polymer, RGO/NW and RGO/MWCNT/NW based spacers into highly conductive pyrolytic graphite papers (G) [166]. Fig. 43a illustrates the wetting and re-drying of the sandwich structures. It can be observed from Fig. 43b&c, that the EMI SE is improved for both G-rGO/NW-G and G-rGO/MWCNT/NW-G sandwich structures upon wetting. Also, the re-dried structures maintained the same EMI SE as that of the initial structures. When wetted with water, the polar functional groups in water create hydrogen bonding with functional groups in the spacer, leading to strong and enhanced electromagnetic loss. It depicts the structural and functional stability of prepared sandwich structures. The G-RGO/NW-G exhibited higher EMI SE than the G-RGO/MWCNT/NW-G. Hence, function switchable and function enhanced EMI shielding smart structures are realized.

Singh et al. demonstrated an SE of 37 dB in the frequency range of 12.4–18 GHz for the sandwich structures composed of iron oxide decorated MWCNT in between RGO sheets [167]. Song et al. prepared flexible ethylene-vinyl acetate (EVA) copolymer films embedded with nano-thin multilayer graphene nanosheets (MLG) in a sandwich structure and demonstrated optimized SE up to 27 dB [168]. Song et al. achieved an EMI SE of ~46.3 dB for two-layer graphene paper with wax sandwiched between them at a thickness of ~0.3 mm [169].

It is inferred from the above-reported studies that the multilayer sandwich nanostructures could exhibit frequency selective EMI shielding performance because of the employment of resonance features. The resonance features can be tailored by changing the spacer between conductive layers. The spacer with different

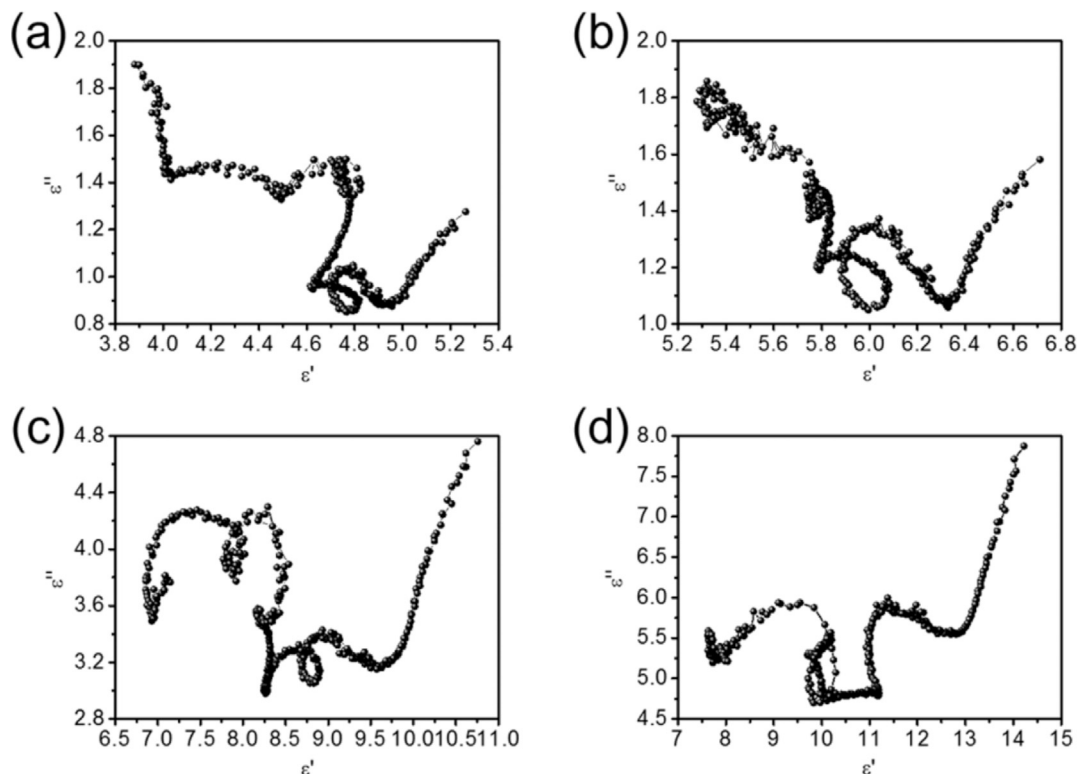


Fig. 37. Cole-Cole plots for (a) 3 wt %, (b) 5 wt %, (c) 10 wt %, and (d) 15 wt % of MoS_2/RGO loaded wax composites. Reproduced with permission from Ref. [161]. Copyright © 2015 American Chemical Society.

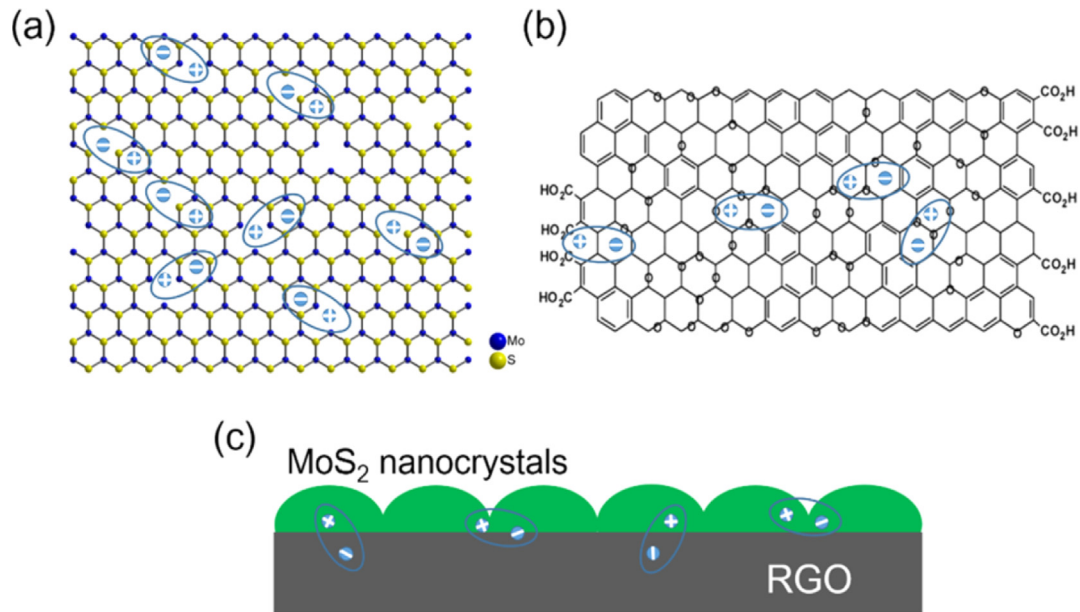


Fig. 38. Illustrations of multi-relaxations dielectric properties in the MoS₂/RGO Hybrid: (a) Defect Dipole Polarization of MoS₂; (b) Defect Dipole Polarization of RGO; (c) Multiple Interfacial Polarizations in the MoS₂/RGO Hybrid. Reproduced with permission from Ref. [161]. Copyright © 2015 American Chemical Society. (A colour version of this figure can be viewed online.)

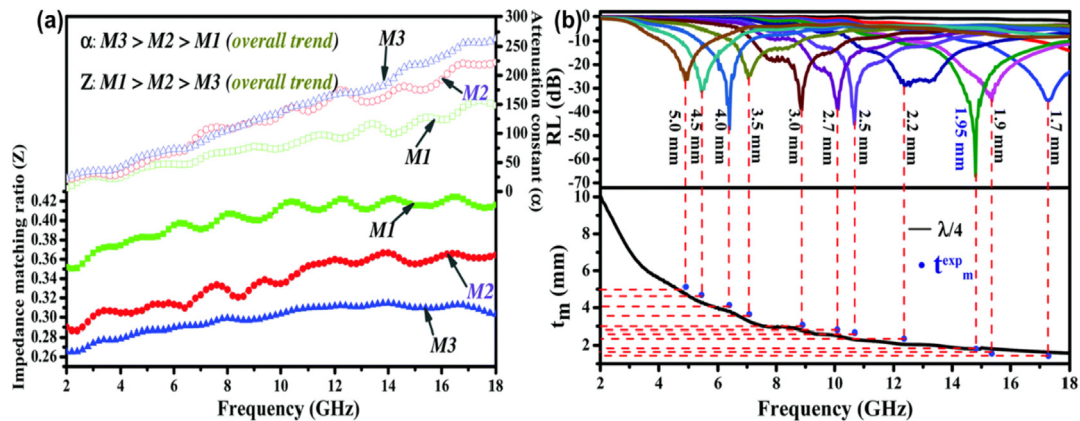


Fig. 39. (a) Frequency dependence of the impedance matching ratio (Z_r) and attenuation constant (α) of MoS₂/RGO composites. (b) Comparison of various absorber thicknesses (t_m) for sample M₂ with the simulated thickness under $\lambda/4$ conditions at the frequency of maximum RL values (f_m). Reproduced with permission from Ref. [163]. Copyright © The Royal Society of Chemistry and the Centre National de la Recherche Scientifique 2017. (A colour version of this figure can be viewed online.)

properties such as dielectric loss or magnetic loss in place of the polymeric spacer (Fig. 42a&b) would substantially interrupt the resonance and thus multilayer carbon-based sandwich nanostructures could exhibit broad EMI SE by EM scattering. From these results, it can be inferred that the EMI SE of the multilayered structures can be varied by modifying the spacers with different properties as well as environmental conditions. This leads to the development of advanced nanostructures with self-tunable EMI shielding.

9. Carbon-based multicomponent nanostructures

The amalgamation convention has recently changed from simple to hybrid nanomaterials to accumulate every single fundamental property in a solitaire composite for better shielding efficiency. For example, Zhao et al. reported sandwich microstructured expanded graphite (EG)/BaFe₁₂O₁₉ (BF) nanocomposites

connected with CNT [170]. The maximum RL of the sandwich microstructured CNT/EG/BF composites with a thickness of 1 mm was up to -45.8 dB, and the frequency bandwidth below -10 dB could reach 4.2 GHz within the frequency range of 2–18 GHz. It is demonstrated that the maximum value of the RL shifts toward the low-frequency direction as the thickness increases because the travel path and time of the incident microwaves are different in the absorbers of different thicknesses and the synergy of microwave absorption. This indicates that the absorption bandwidth can be adjusted by altering the thickness of samples according to the requirement. Ding et al. prepared FeNi₃ decorated RGO/molybdenum disulfide (FeNi₃@RGO/MoS₂). The role of each component is as follows; (a) GO as a dielectric material with large specific surface area contributes to higher $\tan \delta_E$ and acts as an ideal substrate, (b) molybdenum disulfide with similar layer structure prevents the restacking of 2D nanosheets and (c) FeNi₃ nanoalloys as $\tan \delta_M$ absorbent improve the absorption property and the impedance

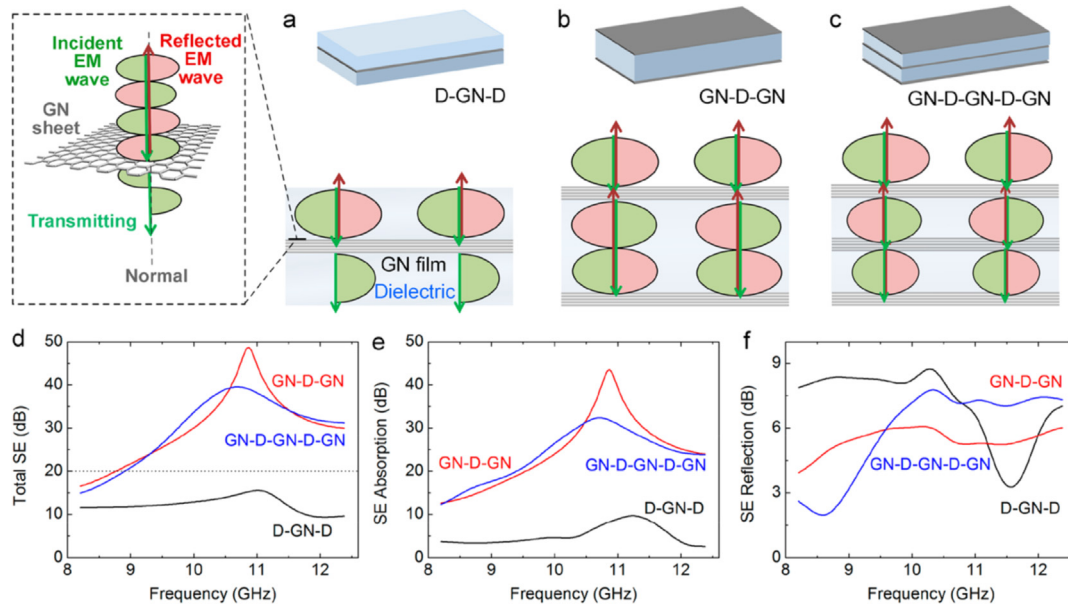


Fig. 40. Schematic cross-section views of (a) D-GN-D, (b) GN-D-GN, and (c) GN-D-GN-D-GN sandwich structures and their corresponding (d) SE_T , (e) SE_A and (f) SE_R reflection. (Green and Pink color represent the transmittance and reflected EM wave, respectively (Not to scale)). Reproduced with permission from Ref. [165]. Copyright © 2017 American Chemical Society. (A colour version of this figure can be viewed online.)

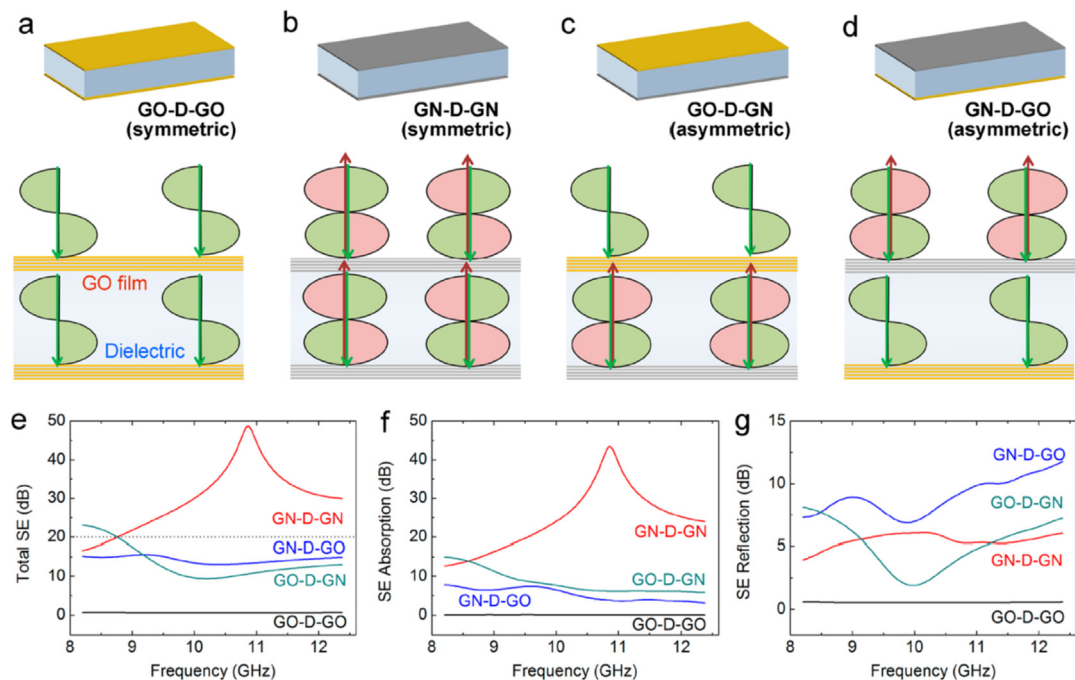


Fig. 41. Schematic cross-section view of (a) GO-D-GO, (b) GN-D-GN, (c) GO-D-GN, and (d) GN-D-GO sandwich structures and their corresponding (e) SE_T , (f) SE_A , and (g) SE_R . Reproduced with permission from Ref. [165]. Copyright © 2017 American Chemical Society. (A colour version of this figure can be viewed online.)

matching. The maximum absorption bandwidth of 4.72 GHz and RL value of -30.39 dB are achieved with a thickness of 2.0 mm for 40% $FeNi_3@RGO/MoS_2$ in a wax matrix [171]. Wang et al. prepared metal-organic framework (MOF-53(Fe))/RGO composites by hydrothermal method and investigated their EMI shielding performance. The interfaces between the pores in the MOF, the interfaces between MOF and rGO and their defects, high σ and large surface area of RGO enhanced the microwave attenuation with absorption as the dominating mechanism. For the prepared samples, the

maximum RL is -25.8 dB at 15.4 GHz and the absorption bandwidths exceeding -10 dB are 12.2 GHz (from 5.8 to 18 GHz) with a thickness in the range of 1.5–4 mm [172]. Yuan et al. obtained ZIF-67 from carbonaceous Co_3O_4/Co by combining Co-based MOF such as ZIF-67 and GO nanosheets and adjusting the pyrolyzing temperature. The maximum RL of the as-prepared composite is up to -52.8 dB at 13.12 GHz and the absorption bandwidth (RL less than -10 dB) can reach up to 10.72 GHz (from 4.88 to 15.6 GHz) with a thickness range of 2.0–4.0 mm [173].

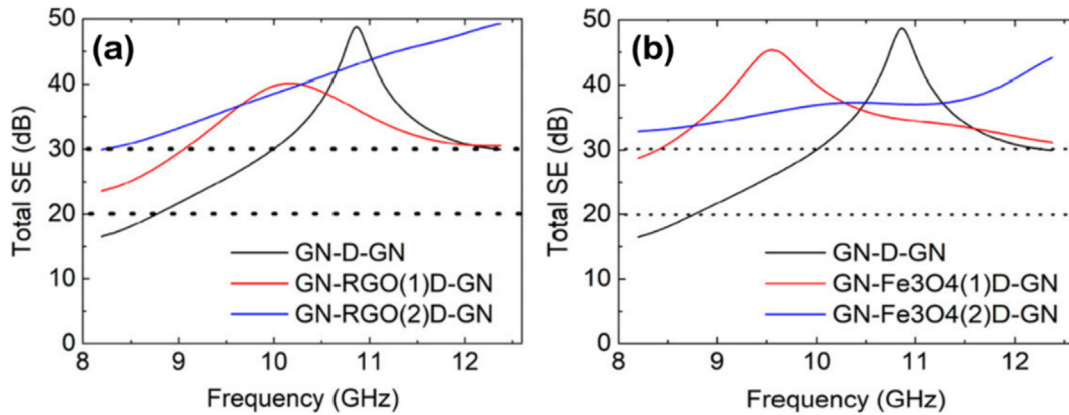


Fig. 42. Comparison of SE_T of sandwich structures with (a) dielectric loss spacer (RGO coated polymeric textile) and (b) magnetic loss spacer (Fe_3O_4). Reproduced with permission from Ref. [165]. Copyright © 2017 American Chemical Society. (A colour version of this figure can be viewed online.)

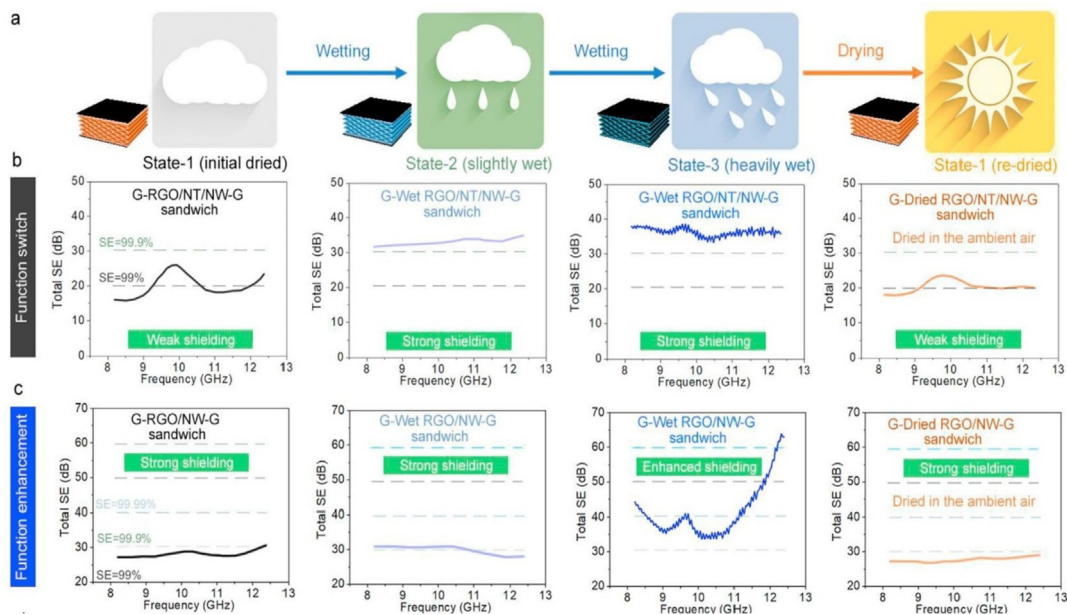


Fig. 43. Schematic explaining the self-tunability of carbon nanostructures based sandwich structures such as (b) function switch and (c) function enhancement for the G-RGO/NT/NW-G and G-RGO/NW-G with respect to (a) wetting conditions. Reproduced with permission from Ref. [166]. Copyright © 2018 Elsevier B.V. (A colour version of this figure can be viewed online.)

10. Conclusion and perspective

This review article comprehensively highlighted the most advanced carbon nanostructures and their corresponding nanocomposites as emerging EMI shielding materials. The fundamental concepts of EMI shielding are described. The effect of the morphology, functionalization and the ratio between the components in the carbon nanostructures and their nanostructured composites on dielectric, magnetic and EMI shielding properties along with the corresponding EMI shielding mechanisms are discussed. The composites of EMI shielding material and wax are non-isotropic, so it is difficult to relate them to pure EMI shielding materials. However, the properties of the wax matrix in combination with the EMI shielding material can be tuned by adjusting the distribution and weight percentage of the EMI shielding material in the wax matrix and improving the interfacial properties between them. The attractive features of carbon nanostructures and their nanostructured composites such as lightweight (compared with

metals or ceramics) [236–256], easy processability, small matching thickness, broad bandwidth, high absorption, etc. demonstrated their potential in future EMI shielding applications.

Besides their advantages as effective conductive fillers in an insulating matrix, increasing filler contents increases the reflection (which is not desirable) while having high SE_T . As the fundamental principle for attaining high EMI performance and high adsorption, the balance between the values of permittivity, frequency, and conductivity is commonly needed. Another factor is the effective absorption bandwidth and material thickness. Many reported materials possess small effective absorption bandwidth and large thickness. Nanostructured composites and multi-component nanostructures are expected to exhibit absorption dominant mechanism with considerable absorption bandwidth. Therefore, the general trend is to develop novel, multifunctional nanocomposites that utilize the nanofiller properties. Tailoring the surface morphology, mass ratio, size and the localization of fillers ensures the tuning of EMI performance.

Still, there is no clear understanding of the factors that determine the effective bandwidth and thickness of the particular material. Efforts should be taken to understand these factors. In fact, excellent absorbers not only combine different materials but also take into account of impedance matching and energy savings. In most cases, the materials reported are tested at the laboratory level. The work on the synthesis mechanism is very important, it can be scaled up and can be practically used for commercial purposes. Recently, lightweight multilayered nanostructure and three-dimensional architectures such as foams, hydrogel, and aerogel have attracted the researcher attention to achieve EMI absorption at low thickness. However, efficient methods to control the formation of lightweight materials and proper utilization of the existing pores and interfaces are still unclear. In case of the multilayer structure, they suffer from cracks and mechanical failures. Thus, more research is needed to achieve a lighter and thinner material with excellent EM absorption as well as dimensional and thermal stability. With the rapid development and breakthroughs in interdisciplinary science and technology, it is possible to integrate all the requirements into our future EMI shielding materials. However, we envisage that with the advancement of multi-component nanostructures and their multi-layer and three-dimensional architecture, novel ultra-efficient EMI shielding material can be realized. We believe that this review throws light on current trend in this interesting area of research and innovative ideas for achieving considerable progress towards efficient shielding materials for different high-end applications.

Acknowledgments

Mr. MV grateful to the Indo-US Science and Technology Forum (IUSSTF), Department of Science and Technology (DST), New Delhi for providing a fellowship under BASE program (IUSSTF BASE Internships 2018/12/Vignesh M, dt. 09/04/2018). The work is partially funded by the National Natural Science Foundation of China (Project No. 51503187, 21504037, and 51603194); the National key R&D Project (Project No. 2016YFE0102700); the Shanxi provincial foundation for science and technology research (Project No. 201601D021058, 201701D221050). Partial support is also from the NIMHD-RCMI grant number 5G12MD007595 from the National Institute of Minority Health, Health Disparities and the NIGMS-BUILD grant number 8UL1GM118967 and National Science Foundation (Grant 1700429).

References

- [1] P.A. Chatterton, M.A. Houlden, *EMC: Electromagnetic Theory to Practical Design*, Wiley, 1991.
- [2] C. Christopoulos, *Principles and Techniques of Electromagnetic Compatibility*, second ed., CRC Press, Boca Raton, 2007.
- [3] D.D.L. Chung, Electromagnetic interference shielding effectiveness of carbon materials, *Carbon* 39 (2) (2001) 279–285.
- [4] Q. Liu, H. Liu, M. Han, J. Zhu, Y. Liang, Z. Xu, Y. Song, Nanometer-sized nickel hollow spheres, *Adv. Mater.* 17 (16) (2005) 1995–1999.
- [5] J.L. Wallace, Broadband magnetic microwave absorbers: fundamental limitations, *IEEE Trans. Magn.* 29 (6) (1993) 4209–4214.
- [6] R. Ramasubramaniam, J. Chen, H. Liu, Homogeneous carbon nanotube/polymer composites for electrical applications, *Appl. Phys. Lett.* 83 (14) (2003) 2928–2930.
- [7] Y. Yonglai, C.G. Mool, L.D. Kenneth, W.L. Roland, The fabrication and electrical properties of carbon nanofibre-polystyrene composites, *Nanotechnology* 15 (11) (2004) 1545.
- [8] H.J. Barraza, F. Pompeo, E.A. O'Rea, D.E. Resasco, SWNT-filled thermoplastic and elastomeric composites prepared by miniemulsion polymerization, *Nano Lett.* 2 (8) (2002) 797–802.
- [9] S. Ramirez, D. Ferreira, V. Gottberg, M. Labady, A. Albornoz, J. Laine, Adding a micropore framework to a parent activated carbon by carbon deposition from methane or ethylene, *Carbon* 41 (13) (2003) 2653–2655.
- [10] Z.P. Wu, D.M. Cheng, W.J. Ma, J.W. Hu, Y.H. Yin, Y.Y. Hu, Y.S. Li, J.G. Yang, Q.F. Xu, Electromagnetic interference shielding effectiveness of composite carbon nanotube macro-film at a high frequency range of 40 GHz to 60 GHz, *AIP Adv.* 5 (6) (2015) 067130.
- [11] J.L. Snoek, Dispersion and absorption in magnetic ferrites at frequencies above one Mc/s, *Physica* 14 (4) (1948) 207–217.
- [12] X. Li, H. Yi, J. Zhang, J. Feng, F. Li, D. Xue, H. Zhang, Y. Peng, N.J. Mellors, Fe₃O₄-graphene hybrids: nanoscale characterization and their enhanced electromagnetic wave absorption in gigahertz range, *J. Nanoparticle Res.* 15 (3) (2013) 1472.
- [13] J.-H. Oh, K.-S. Oh, C.-G. Kim, C.-S. Hong, Design of radar absorbing structures using glass/epoxy composite containing carbon black in X-band frequency ranges, *Compos. B Eng.* 35 (1) (2004) 49–56.
- [14] K.H. Wu, T.H. Ting, G.P. Wang, W.D. Ho, C.C. Shih, Effect of carbon black content on electrical and microwave absorbing properties of polyaniline/carbon black nanocomposites, *Polym. Degrad. Stabil.* 93 (2) (2008) 483–488.
- [15] S.H. Kim, Y.G. Park, S.S. Kim, Double-layered microwave absorbers composed of ferrite and carbon fiber composite laminates, *Phys. Status Solidi C* 4 (12) (2007) 4602–4605.
- [16] F. Nanni, P. Travaglia, M. Valentini, Effect of carbon nanofibres dispersion on the microwave absorbing properties of CNF/epoxy composites, *Compos. Sci. Technol.* 69 (3) (2009) 485–490.
- [17] Z. Zheng, B. Xu, L. Huang, L. He, X. Ni, Novel composite of Co/carbon nanotubes: synthesis, magnetism and microwave absorption properties, *Solid State Sci.* 10 (3) (2008) 316–320.
- [18] C. Renchao, L. Chongyun, S. Honglong, Z. Xingui, Y. Xinan, Electron energy-loss spectroscopy characterization and microwave absorption of iron-filled carbon-nitrogen nanotubes, *Nanotechnology* 18 (35) (2007) 355705.
- [19] L. Kong, X. Yin, Y. Zhang, X. Yuan, Q. Li, F. Ye, L. Cheng, L. Zhang, Electromagnetic wave absorption properties of reduced graphene oxide modified by maghemite colloidal nanoparticle clusters, *J. Phys. Chem. C* 117 (38) (2013) 19701–19711.
- [20] N.V. Machmerieen, French Patent No. 802728, 1936.
- [21] W. Emerson, Electromagnetic wave absorbers and anechoic chambers through the years, *IEEE Trans. Antenn. Propag.* 21 (4) (1973) 484–490.
- [22] A. Wadhawan, D. Garrett, J.M. Perez, Nanoparticle-assisted microwave absorption by single-wall carbon nanotubes, *Appl. Phys. Lett.* 83 (13) (2003) 2683–2685.
- [23] H. Keqiang, Y. Liming, S. Leimei, A. Kang, A. Yoshinori, Z. Xinluo, Doping effect of single-wall carbon nanotubes on the microwave absorption properties of nanocrystalline barium ferrite, *Jpn. J. Appl. Phys.* 49 (12R) (2010) 125101.
- [24] X. Gui, K. Wang, J. Wei, R. Lü, Q. Shu, Y. Jia, C. Wang, H. Zhu, D. Wu, Microwave absorbing properties and magnetic properties of different carbon nanotubes, *Sci. China, Ser. A: Technol. Sci.* 52 (1) (2009) 227–231.
- [25] P.C.P. Watts, W.K. Hsu, A. Barnes, B. Chambers, High permittivity from defective multiwalled carbon nanotubes in the X-band, *Adv. Mater.* 15 (7–8) (2003) 600–603.
- [26] J.D. Joannopoulos, P.R. Villeneuve, S. Fan, Photonic crystals: putting a new twist on light, *Nature* 386 (1997) 143.
- [27] H. Bai, C. Li, X. Wang, G. Shi, On the gelation of graphene oxide, *J. Phys. Chem. C* 115 (13) (2011) 5545–5551.
- [28] H.-B. Zhang, Q. Yan, W.-G. Zheng, Z. He, Z.-Z. Yu, Tough Graphene–Polymer microcellular foams for electromagnetic interference shielding, *ACS Appl. Mater. Interfaces* 3 (3) (2011) 918–924.
- [29] L.S.-F. FANG Jian-Jun, Z.H.A. Wen-Ke, C.O.N.G. Hong-Yun, C.H.E.N. Jun-Fang, C.H.E.N. Zong-Zhang, Microwave absorbing properties of nickel-coated graphene, *J. Inorg. Mater.* 26 (5) (2011) 467–471.
- [30] J.-S. Li, H. Huang, Y.-J. Zhou, C.-Y. Zhang, Z.-T. Li, Research progress of graphene-based microwave absorbing materials in the last decade, *J. Mater. Res.* 32 (7) (2017) 1213–1230.
- [31] S. Biswas, S.S. Panja, S. Bose, Tailored distribution of nanoparticles in biphasic polymeric blends as emerging materials for suppressing electromagnetic radiation: challenges and prospects, *J. Mater. Chem. C* 6 (13) (2018) 3120–3142.
- [32] F. Qin, C. Brosseau, A review and analysis of microwave absorption in polymer composites filled with carbonaceous particles, *J. Appl. Phys.* 111 (6) (2012) 061301.
- [33] M.-S. Cao, X.-X. Wang, W.-Q. Cao, J. Yuan, Ultrathin graphene: electrical properties and highly efficient electromagnetic interference shielding, *J. Mater. Chem. C* 3 (26) (2015) 6589–6599.
- [34] L. Lv, J. Liu, H. Liu, C. Liu, Y. Lu, K. Sun, R. Fan, N. Wang, N. Lu, Z. Guo, E.K. Wujcik, An overview of electrically conductive polymer nanocomposites toward electromagnetic interference shielding, *Eng. Sci.* 2 (2018) 26–42. www.doi.org/10.30919/es8d615.
- [35] Y. Ando, X. Zhao, K. Hirahara, K. Suenaga, S. Bandow, S. Iijima, Mass production of single-wall carbon nanotubes by the arc plasma jet method, *Chem. Phys. Lett.* 323 (5) (2000) 580–585.
- [36] X. Fang, A. Shashurin, G. Teel, M. Keidar, Determining synthesis region of the single wall carbon nanotubes in arc plasma volume, *Carbon* 107 (2016) 273–280.
- [37] S. Yatomi, J. Bak, A. Khrabryi, Y. Raitses, Detection of nanoparticles in carbon arc discharge with laser-induced incandescence, *Carbon* 117 (2017) 154–162.
- [38] P.C. Eklund, B.K. Pradhan, U.J. Kim, Q. Xiong, J.E. Fischer, A.D. Friedman, B.C. Holloway, K. Jordan, M.W. Smith, Large-scale production of single-walled carbon nanotubes using ultrafast pulses from a free electron laser,

- Nano Lett. 2 (6) (2002) 561–566.
- [39] W.K. Hsu, M. Terrones, J.P. Hare, H. Terrones, H.W. Kroto, D.R.M. Walton, Electrolytic formation of carbon nanostructures, *Chem. Phys. Lett.* 262 (1) (1996) 161–166.
- [40] K.A. Shah, B.A. Tali, Synthesis of carbon nanotubes by catalytic chemical vapour deposition: a review on carbon sources, catalysts and substrates, *Mater. Sci. Semicond. Process.* 41 (2016) 67–82.
- [41] D. Laplaze, P. Bernier, W.K. Maser, G. Flamant, T. Guillard, A. Loiseau, Carbon nanotubes: the solar approach, *Carbon* 36 (5) (1998) 685–688.
- [42] L. Alvarez, T. Guillard, J.L. Sauvajol, G. Flamant, D. Laplaze, Solar production of single-wall carbon nanotubes: growth mechanisms studied by electron microscopy and Raman spectroscopy, *Appl. Phys. A* 70 (2) (2000) 169–173.
- [43] C. Mattevi, G. Eda, S. Agnoli, S. Miller, A.K. Mkhoyan, O. Celik, D. Mastrogiovanni, G. Granozzi, E. Garfunkel, M. Chhowalla, Evolution of electrical, chemical, and structural properties of transparent and conducting chemically derived graphene thin films, *Adv. Funct. Mater.* 19 (16) (2009) 2577–2583.
- [44] K.S. Novoselov, A.K. Geim, S.V. Morozov, D. Jiang, Y. Zhang, S.V. Dubonos, I.V. Grigorieva, A.A. Firsov, Electric field in atomically thin carbon films, *Sciences* 306 (5696) (2004) 666–669.
- [45] S.M. Notley, Highly concentrated aqueous suspensions of graphene through ultrasonic exfoliation with continuous surfactant addition, *Langmuir* 28 (40) (2012) 14110–14113.
- [46] J. Lin, Y. Huang, S. Wang, G. Chen, Microwave-assisted rapid exfoliation of graphite into graphene by using ammonium bicarbonate as the intercalation agent, *Ind. Eng. Chem. Res.* 56 (33) (2017) 9341–9346.
- [47] S. Stankovich, D.A. Dikin, R.D. Piner, K.A. Kohlhaas, A. Kleinhammes, Y. Jia, Y. Wu, S.T. Nguyen, R.S. Ruoff, Synthesis of graphene-based nanosheets via chemical reduction of exfoliated graphite oxide, *Carbon* 45 (7) (2007) 1558–1565.
- [48] K.S. Subrahmanyam, L.S. Panchakarla, A. Govindaraj, C.N.R. Rao, Simple method of preparing graphene flakes by an arc-discharge method, *J. Phys. Chem. C* 113 (11) (2009) 4257–4259.
- [49] X. Wang, H. You, F. Liu, M. Li, L. Wan, S. Li, Q. Li, Y. Xu, R. Tian, Z. Yu, D. Xiang, J. Cheng, Large-scale synthesis of few-layered graphene using CVD, *Chem. Vap. Depos.* 15 (1–3) (2009) 53–56.
- [50] C.D. Simpson, G. Matteredsteig, K. Martin, L. Gherghel, R.E. Bauer, H.J. Räder, K. Müllen, Nanosized molecular propellers by cyclodehydrogenation of polyphenylene dendrimers, *J. Am. Chem. Soc.* 126 (10) (2004) 3139–3147.
- [51] W. Choi, I. Lahiri, R. Seelaboyina, Y.S. Kang, Synthesis of graphene and its applications: a review, *Crit. Rev. Solid State Mater. Sci.* 35 (1) (2010) 52–71.
- [52] B.C. Brodie XIII, On the atomic weight of graphite, *Phil. Trans. Roy. Soc. Lond.* 149 (1859) 249–259.
- [53] L. Staudenmaier, Verfahren zur Darstellung der Graphitsäure, *Ber. Dtsch. Chem. Ges.* 31 (2) (1898) 1481–1487.
- [54] H.C. Schniepp, J.-L. Li, M.J. McAllister, H. Sai, M. Herrera-Alonso, D.H. Adamson, R.K. Prud'homme, R. Car, D.A. Saville, I.A. Aksay, Functionalized single graphene sheets derived from splitting graphite oxide, *J. Phys. Chem. B* 110 (17) (2006) 8535–8539.
- [55] W.S. Hummers, R.E. Offeman, Preparation of graphitic oxide, *J. Am. Chem. Soc.* 80 (6) (1958), 1339–1339.
- [56] B. Wen, X.X. Wang, W.Q. Cao, H.L. Shi, M.M. Lu, G. Wang, H.B. Jin, W.Z. Wang, J. Yuan, M.S. Cao, Reduced graphene oxides: the thinnest and most lightweight materials with highly efficient microwave attenuation performances of the carbon world, *Nanoscale* 6 (11) (2014) 5754–5761.
- [57] M. Khan, M.N. Tahir, S.F. Adil, H.U. Khan, M.R.H. Siddiqui, A.A. Al-warthan, W. Tremel, Graphene based metal and metal oxide nanocomposites: synthesis, properties and their applications, *J. Mater. Chem. A* 3 (37) (2015) 18753–18808.
- [58] S.F. Kiew, L.V. Kiew, H.B. Lee, T. Imae, L.Y. Chung, Assessing biocompatibility of graphene oxide-based nanocarriers: a review, *J. Contr. Release* 226 (2016) 217–228.
- [59] P. Kuzhir, S. Maksimenko, D. Bychanok, V. Kuznetsov, S. Moseenkov, I. Mazov, O. Shenderova, P. Lambin, Nano-scaled onion-like carbon: prospective material for microwave coatings, *Metamaterials* 3 (3) (2009) 148–156.
- [60] X. Su, J. Zhang, Y. Jia, Y. Liu, J. Xu, J. Wang, Preparation and microwave absorption property of nano onion-like carbon in the frequency range of 8.2–12.4 GHz, *J. Alloys Compd* 695 (2017) 1420–1425.
- [61] L. Jiang, Z. Wang, D. Geng, Y. Lin, Y. Wang, J. An, J. He, D. Li, W. Liu, Z. Zhang, Structure and electromagnetic properties of both regular and defective onion-like carbon nanoparticles, *Carbon* 95 (2015) 910–918.
- [62] H. Bi, K.-C. Kou, K. Ostrikov, L.-K. Yan, Z.-C. Wang, Microstructure and electromagnetic characteristics of Ni nanoparticle film coated carbon microcoils, *J. Alloy. Comp.* 478 (1) (2009) 796–800.
- [63] M. Arjmand, K. Chizari, B. Krause, P. Pötschke, U. Sundararaj, Effect of synthesis catalyst on structure of nitrogen-doped carbon nanotubes and electrical conductivity and electromagnetic interference shielding of their polymeric nanocomposites, *Carbon* 98 (2016) 358–372.
- [64] E. Zhou, J. Xi, Y. Guo, Y. Liu, Z. Xu, L. Peng, W. Gao, J. Ying, Z. Chen, C. Gao, Synergistic effect of graphene and carbon nanotube for high-performance electromagnetic interference shielding films, *Carbon* 133 (2018) 316–322.
- [65] J. Liu, Y. Liu, H.-B. Zhang, Y. Dai, Z. Liu, Z.-Z. Yu, Superelastic and multi-functional graphene-based aerogels by interfacial reinforcement with graphitized carbon at high temperatures, *Carbon* 132 (2018) 95–103.
- [66] Z. Fang, C. Li, J. Sun, H. Zhang, J. Zhang, The electromagnetic characteristics of carbon foams, *Carbon* 45 (15) (2007) 2873–2879.
- [67] F. Shahzad, P. Kumar, S. Yu, S. Lee, Y.-H. Kim, S.M. Hong, C.M. Koo, Sulfur-doped graphene laminates for EMI shielding applications, *J. Mater. Chem. C* 3 (38) (2015) 9802–9810.
- [68] V. Murugadoss, N. Wang, S. Tadakamalla, B. Wang, Z. Guo, S. Angaiah, In situ grown cobalt selenide/graphene nanocomposite counter electrodes for enhanced dye-sensitized solar cell performance, *J. Mater. Chem. A* 5 (2017) 14583–14594.
- [69] B. Song, T. Wang, H. Sun, Q. Shao, J. Zhao, K. Song, L. Hao, L. Wang, Z. Guo, Two-step hydrothermally synthesized carbon nanodots/WO₃ photocatalysts with enhanced photocatalytic performance, *Dalton Trans.* 46 (45) (2017) 15769–15777.
- [70] C. Lin, H. Hu, C. Cheng, et al., Nano-TiNb₂O₇/carbon nanotubes composite anode for enhanced lithium-ion storage, *Electrochim. Acta* 260 (2018) 65–72.
- [71] X. Zheng, J. Feng, Y. Zong, H. Miao, X. Hu, J. Bai, X. Li, Hydrophobic graphene nanosheets decorated by monodispersed superparamagnetic Fe₃O₄ nanocrystals as synergistic electromagnetic wave absorbers, *J. Mater. Chem. C* 3 (17) (2015) 4452–4463.
- [72] D. Chen, H. Quan, G.S. Wang, L. Guo, Hollow α -MnS. Spheres, Their Hybrids, With reduced graphene oxide: synthesis, microwave absorption, and lithium storage properties, *ChemPlusChem* 8 (8) (2013) 843–851.
- [73] T. Wu, Y. Liu, X. Zeng, T. Cui, Y. Zhao, Y. Li, G. Tong, Facile hydrothermal synthesis of Fe₃O₄/C core-shell nanorings for efficient low-frequency microwave absorption, *ACS Appl. Mater. Interfaces* 8 (11) (2016) 7370–7380.
- [74] D. Ding, Y. Wang, X. Li, et al., Rational design of core-shell Co/C microspheres for high-performance microwave absorption, *Carbon* 111 (2017) 722–732.
- [75] S. Wei, X. Wang, B. Zhang, M. Yu, Y. Zheng, Y. Wang, J. Liu, Preparation of hierarchical core-shell C@NiCo₂O₄@Fe₃O₄ composites for enhanced microwave absorption performance, *Chem. Eng. J.* 314 (2017) 477–487.
- [76] Q. Song, F. Ye, X. Yin, W. Li, H. Li, Y. Liu, K. Li, K. Xie, X. Li, Q. Fu, L. Cheng, L. Zhang, B. Wei, Carbon nanotube-multilayered graphene edge plane core-shell hybrid foams for ultrahigh-performance electromagnetic-interference shielding, *Adv. Mater.* 29 (31) (2017) 1701583.
- [77] Y. Li, R. Liu, X. Pang, X. Zhao, Y. Zhang, G. Qin, X. Zhang, Fe@C nanocapsules with substitutional sulfur heteroatoms in graphitic shells for improving microwave absorption at gigahertz frequencies, *Carbon* 126 (2018) 372–381.
- [78] Q. Su, J. Li, G. Zhong, G. Du, B. Xu, Situ synthesis of iron/nickel sulfide nanostructures-filled carbon nanotubes and their electromagnetic and microwave-absorbing properties, *J. Phys. Chem. C* 115 (5) (2011) 1838–1842.
- [79] G.K. Deb, *Electromagnetic Interference and Electromagnetic Compatibility*, Tata McGraw-Hill, 1995.
- [80] S. Geetha, K.K. Satheesh Kumar, R.K. Rao Chepuri, M. Vijayan, D.C. Trivedi, EMI shielding: methods and materials-A review, *J. Appl. Polym. Sci.* 112 (4) (2009) 2073–2086.
- [81] P. Saini, M. Arora, Microwave absorption and EMI shielding behavior of nanocomposites based on intrinsically conducting polymers, graphene and carbon nanotubes, new polymers for special applications alton de souza gomes, *Intech* (2012), <https://doi.org/10.5772/48779>.
- [82] Y. Wang, X. Jing, Intrinsically conducting polymers for electromagnetic interference shielding, *Polym. Adv. Technol.* 16 (4) (2005) 344–351.
- [83] J. Joo, C.Y. Lee, High frequency electromagnetic interference shielding response of mixtures and multilayer films based on conducting polymers, *J. Appl. Phys.* 88 (1) (2000) 513–518.
- [84] N.F. Colaneri, L.W. Schacklette, EMI shielding measurements of conductive polymer blends, *IEEE Trans. Instrum. Meas* 41 (2) (1992) 291–297.
- [85] Y. Naito, K. Suetake, Application of ferrite to electromagnetic wave absorber and its characteristics, *IEEE Trans. Microw. Techn. Theor.* 19 (1) (1971) 65–72.
- [86] A.N. Yusoff, M.H. Abdullah, S.H. Ahmad, S.F. Jusoh, A.A. Mansor, S.A.A. Hamid, Electromagnetic and absorption properties of some microwave absorbers, *J. Appl. Phys.* 92 (2) (2002) 876–882.
- [87] W.-L. Song, M.-S. Cao, L.-Z. Fan, M.-M. Lu, Y. Li, C.-Y. Wang, H.-F. Ju, Highly ordered porous carbon/wax composites for effective electromagnetic attenuation and shielding, *Carbon* 77 (2014) 130–142.
- [88] P. Xu, X. Han, C. Wang, D. Zhou, Z. Lv, A. Wen, X. Wang, B. Zhang, Synthesis of electromagnetic functionalized nickel/polypyrrole core/shell composites, *J. Phys. Chem. B* 112 (34) (2008) 10443–10448.
- [89] W. Zhu, L. Wang, R. Zhao, J. Ren, G. Lu, Y. Wang, Electromagnetic and microwave-absorbing properties of magnetic nickel ferrite nanocrystals, *Nanoscale* 3 (7) (2011) 2862–2864.
- [90] T. Philippe, V. Guillaume, A. Olivier, F.-V. Francoise, F. Fernand, Monodisperse ferromagnetic particles for microwave applications, *Adv. Mater.* 10 (13) (1998) 1032–1035.
- [91] R. Arias, P. Chu, D.L. Mills, Dipole exchange spin waves and microwave response of ferromagnetic spheres, *Phys. Rev. B* 71 (22) (2005) 224410.
- [92] C. Kittel, On the theory of ferromagnetic resonance absorption, *Phys. Rev.* 73 (2) (1948) 155–161.
- [93] S. Pei, J. Zhao, J. Du, W. Ren, H.-M. Cheng, Direct reduction of graphene oxide films into highly conductive and flexible graphene films by hydrohalic acids, *Carbon* 48 (15) (2010) 4466–4474.
- [94] P.N. Nirmalraj, T. Lutz, S. Kumar, G.S. Duesberg, J.J. Boland, *Nanoscale*

- mapping of electrical resistivity and connectivity in graphene strips and networks, *Nano Lett.* 11 (1) (2011) 16–22.
- [95] X. Zhao, C.M. Hayner, M.C. Kung, H.H. Kung, Flexible holey graphene paper electrodes with enhanced rate capability for energy storage applications, *ACS Nano* 5 (11) (2011) 8739–8749.
- [96] H. Chen, B. Müller Marc, J. Gilmore Kerry, G. Wallace Gordon, D. Li, Mechanically strong, electrically conductive, and biocompatible graphene paper, *Adv. Mater.* 20 (18) (2008) 3557–3561.
- [97] W.-L. Song, M.-S. Cao, M.-M. Lu, J. Liu, J. Yuan, L.-Z. Fan, Improved dielectric properties and highly efficient and broadened bandwidth electromagnetic attenuation of thickness-decreased carbon nanosheet/wax composites, *J. Mater. Chem. C* 1 (9) (2013) 1846–1854.
- [98] K. Dai, X.-B. Xu, Z.-M. Li, Electrically conductive carbon black (CB) filled in situ microfibrillar poly(ethylene terephthalate) (PET)/polyethylene (PE) composite with a selective CB distribution, *Polymer* 48 (3) (2007) 849–859.
- [99] J. Wu, D.D.L. Chung, Increasing the electromagnetic interference shielding effectiveness of carbon fiber polymer–matrix composite by using activated carbon fibers, *Carbon* 40 (3) (2002) 445–447.
- [100] M.A. Nahil, P.T. Williams, Recycling of carbon fibre reinforced polymeric waste for the production of activated carbon fibres, *J. Anal. Appl. Pyrolysis* 91 (1) (2011) 67–75.
- [101] Y. Yang, M.C. Gupta, K.L. Dudley, R.W. Lawrence, Novel Carbon Nanotube–Polystyrene foam composites for electromagnetic interference shielding, *Nano Lett.* 5 (11) (2005) 2131–2134.
- [102] A. Javey, J. Guo, Q. Wang, M. Lundstrom, H. Dai, Ballistic carbon nanotube field-effect transistors, *Nature* 424 (2003) 654.
- [103] R. Martel, T. Schmidt, H.R. Shea, T. Hertel, P. Avouris, Single- and multi-wall carbon nanotube field-effect transistors, *Appl. Phys. Lett.* 73 (17) (1998) 2447–2449.
- [104] J.P. Gogoi, N.S. Bhattacharyya, K.C. James Raju, Synthesis and microwave characterization of expanded graphite/novolac phenolic resin composite for microwave absorber applications, *Composites, Part B* 42 (5) (2011) 1291–1297.
- [105] Y. Liu, J. Zeng, D. Han, K. Wu, B. Yu, S. Chai, F. Chen, Q. Fu, Graphene enhanced flexible expanded graphite film with high electric, thermal conductivities and EMI shielding at low content, *Carbon* 133 (2018) 435–445.
- [106] D.-L. Zhao, Z.-M. Shen, Preparation and microwave absorption properties of carbon nanocoils, *Mater. Lett.* 62 (21) (2008) 3704–3706.
- [107] J.-H. Du, C. Sun, S. Bai, G. Su, Z. Ying, H.-M. Cheng, Microwave electromagnetic characteristics of a microcoiled carbon fibers/paraffin wax composite in Ku band, *J. Mater. Res.* 17 (5) (2002) 1232–1236.
- [108] S.A. Maksimenko, V.N. Rodionova, G.Y. Slepyan, V.A. Karpovich, O. Shenderova, J. Walsh, V.L. Kuznetsov, I.N. Mazov, S.I. Moseenkov, A.V. Okotrub, P. Lambin, Attenuation of electromagnetic waves in onion-like carbon composites, *Diam. Relat. Mater.* 16 (4) (2007) 1231–1235.
- [109] Y. Sun, S. Luo, H. Sun, W. Zeng, C. Ling, D. Chen, V. Chan, K. Liao, Engineering closed-cell structure in lightweight and flexible carbon foam composite for high-efficient electromagnetic interference shielding, *Carbon* 136 (2018) 299–308.
- [110] J. Xi, Y. Li, E. Zhou, Y. Liu, W. Gao, Y. Guo, J. Ying, Z. Chen, G. Chen, C. Gao, Graphene aerogel films with expansion enhancement effect of high-performance electromagnetic interference shielding, *Carbon* 135 (2018) 44–51.
- [111] S. Lu, J. Shao, K. Ma, D. Chen, X. Wang, L. Zhang, Q. Meng, J. Ma, Flexible, mechanically resilient carbon nanotube composite films for high-efficiency electromagnetic interference shielding, *Carbon* 136 (2018) 387–394.
- [112] X. Hong, D.D.L. Chung, Carbon nanofiber mats for electromagnetic interference shielding, *Carbon* 111 (2017) 529–537.
- [113] Z. Wang, R. Wei, J. Gu, H. Liu, C. Liu, C. Luo, J. Kong, Q. Shao, N. Wang, Z. Guo, X. Liu, Ultralight, highly compressible and fire-retardant graphene aerogel with self-adjustable electromagnetic wave absorption, *Carbon* 139 (2018) 1126–1135.
- [114] Y. Zhang, Y. Huang, T. Zhang, H. Chang, P. Xiao, H. Chen, Z. Huang, Y. Chen, Broadband and tunable high-performance microwave absorption of an ultralight and highly compressible graphene foam, *Adv. Mater.* 27 (12) (2015) 2049–2053.
- [115] H. Zhang, J. Zhang, H. Zhang, Computation of radar absorbing silicon carbide foams and their silica matrix composites, *Comput. Mater. Sci.* 38 (4) (2007) 857–864.
- [116] B. Shen, Y. Li, D. Yi, W. Zhai, X. Wei, W. Zheng, Microcellular graphene foam for improved broadband electromagnetic interference shielding, *Carbon* 102 (2016) 154–160.
- [117] Y. Li, B. Shen, X. Pei, Y. Zhang, D. Yi, W. Zhai, L. Zhang, X. Wei, W. Zheng, Ultrathin carbon foams for effective electromagnetic interference shielding, *Carbon* 100 (2016) 375–385.
- [118] C. Wan, J. Li, Graphene oxide/cellulose aerogels nanocomposite: preparation, pyrolysis, and application for electromagnetic interference shielding, *Carbohydr. Polym.* 150 (2016) 172–179.
- [119] Z. Zeng, C. Wang, Y. Zhang, P. Wang, S.I. Seyed Shahabadi, Y. Pei, M. Chen, X. Lu, Ultralight and highly elastic graphene/lignin-derived carbon nanocomposite aerogels with ultrahigh electromagnetic interference shielding performance, *ACS Appl. Mater. Interfaces* 10 (9) (2018) 8205–8213.
- [120] Y.G. Zhou, X.T. Zu, F. Gao, H.Y. Xiao, H.F. Lv, Electronic and magnetic properties of graphene absorbed with S atom: a first-principles study, *J. Appl. Phys.* 105 (10) (2009) 104311.
- [121] A. Denis Pablo, R. Faccio, W. Mombru Alvaro, Is it possible to dope single-walled carbon nanotubes and graphene with sulfur? *ChemPhysChem* 10 (4) (2009) 715–722.
- [122] T. Zhang, B. Zhong, J.Q. Yang, X.X. Huang, G. Wen, Boron and nitrogen doped carbon nanotubes/Fe₃O₄ composite architectures with microwave absorption property, *Ceram. Int.* 41 (6) (2015) 8163–8170.
- [123] M.-S. Cao, W.-L. Song, Z.-L. Hou, B. Wen, J. Yuan, The effects of temperature and frequency on the dielectric properties, electromagnetic interference shielding and microwave-absorption of short carbon fiber/silica composites, *Carbon* 48 (3) (2010) 788–796.
- [124] B. Reznik, D. Gerthsen, K.J. Hutter, Micro- and nanostructure of the carbon matrix of infiltrated carbon fiber felts, *Carbon* 39 (2) (2001) 215–229.
- [125] G. Zheng, H. Sano, K. Suzuki, K. Kobayashi, Y. Uchiyama, H.-M. Cheng, A TEM study of microstructure of carbon fiber/polycarbosilane-derived SiC composites, *Carbon* 37 (12) (1999) 2057–2062.
- [126] K.A. B. Systematic conductivity behavior in conducting polymers: effects of heterogeneous disorder, *Adv. Mater.* 13 (12–13) (2001) 927–941.
- [127] A.B. Kaiser, C.J. Liu, P.W. Gilber, B. Chapman, N.T. Kemp, B. Wessling, A.C. Partridge, W.T. Smith, J.S. Shapiro, Comparison of electronic transport in polyaniline blends, polyaniline and polypyrrole, *Synth. Met.* 84 (1) (1997) 699–702.
- [128] B. Wen, M.-S. Cao, Z.-L. Hou, W.-L. Song, L. Zhang, M.-M. Lu, H.-B. Jin, X.-Y. Fang, W.-Z. Wang, J. Yuan, Temperature dependent microwave attenuation behavior for carbon-nanotube/silica composites, *Carbon* 65 (2013) 124–139.
- [129] E.-T. Farid, A.-G.A. A. A.N. Abdel, New PTCR thermistors, switching current, and electromagnetic shielding effectiveness from nanosized vanadium sesquioxides ceramic reinforced epoxy resin nanocomposites, *J. Appl. Polym. Sci.* 115 (2) (2010) 817–825.
- [130] H.-T. Liu, H.-F. Cheng, Z.-Y. Chu, D.-Y. Zhang, Absorbing properties of frequency selective surface absorbers with cross-shaped resistive patches, *Mater. Des.* 28 (7) (2007) 2166–2171.
- [131] V. Skakalova, A.B. Kaiser, Y.S. Woo, S. Roth, Electronic transport in carbon nanotubes: from individual nanotubes to thin and thick networks, *Phys. Rev. B* 74 (8) (2006) 085403.
- [132] W.P. C.P. H. W.-K. B. A. C. B. High permittivity from defective multiwalled carbon nanotubes in the X-band, *Adv. Mater.* 15 (78) (2003) 600–603.
- [133] S. Kirkpatrick, Classical transport in disordered media: scaling and effective-medium theories, *Phys. Rev. Lett.* 27 (25) (1971) 1722–1725.
- [134] A.B. Kaiser, V. Skakalova, Electronic conduction in polymers, carbon nanotubes and graphene, *Chem. Soc. Rev.* 40 (7) (2011) 3786–3801.
- [135] H.-L. Zhang, J.-F. Li, B.-P. Zhang, K.-F. Yao, W.-S. Liu, H. Wang, Electrical and thermal properties of carbon nanotube bulk materials: experimental studies for the 328–958 K temperature range, *Phys. Rev. B* 75 (20) (2007) 205407.
- [136] B. Wen, M. Cao, M. Lu, W. Cao, H. Shi, J. Liu, X. Wang, H. Jin, X. Fang, W. Wang, J. Yuan, Reduced graphene oxides: light-weight and high-efficiency electromagnetic interference shielding at elevated temperatures, *Adv. Mater.* 26 (21) (2014) 3484–3489.
- [137] L. Kong, X. Yin, X. Yuan, Y. Zhang, X. Liu, L. Cheng, L. Zhang, Electromagnetic wave absorption properties of graphene modified with carbon nanotube/poly(dimethyl siloxane) composites, *Carbon* 73 (2014) 185–193.
- [138] L. Wang, Y. Huang, X. Sun, H. Huang, P. Liu, M. Zong, Y. Wang, Synthesis and microwave absorption enhancement of graphene@Fe₃O₄@SiO₂@NiO nanosheet hierarchical structures, *Nanoscale* 6 (6) (2014) 3157–3164.
- [139] Y.-L. Ren, H.-Y. Wu, M.-M. Lu, Y.-J. Chen, C.-L. Zhu, P. Gao, M.-S. Cao, C.-Y. Li, Q.-Y. Ouyang, Quaternary nanocomposites consisting of graphene, Fe₃O₄@Fe Core@Shell, and ZnO nanoparticles: synthesis and excellent electromagnetic absorption properties, *ACS Appl. Mater. Interfaces* 4 (12) (2012) 6436–6442.
- [140] X.-J. Zhang, G.-S. Wang, W.-Q. Cao, Y.-Z. Wei, J.-F. Liang, L. Guo, M.-S. Cao, Enhanced microwave absorption property of reduced graphene oxide (RGO)-MnFe₂O₄ nanocomposites and polyvinylidene fluoride, *ACS Appl. Mater. Interfaces* 6 (10) (2014) 7471–7478.
- [141] V.K. Singh, A. Shukla, M.K. Patra, L. Saini, R.K. Jani, S.R. Vadera, N. Kumar, Microwave absorbing properties of a thermally reduced graphene oxide/nitrile butadiene rubber composite, *Carbon* 50 (6) (2012) 2202–2208.
- [142] C. R.-C, P. L.-M, D. X.-F, C. Q. L. X.-L, Microwave absorption enhancement and complex permittivity and permeability of Fe encapsulated within carbon nanotubes, *Adv. Mater.* 16 (5) (2004) 401–405.
- [143] N. Wu, C. Liu, D. Xu, J. Liu, W. Liu, Q. Shao, Z. Guo, Enhanced electromagnetic wave absorption of three-dimensional porous Fe₃O₄/C composite flowers, *ACS Sustain. Chem. Eng.* 6 (2018) 12471–12480.
- [144] P. Xie, H. Li, B. He, F. Dang, J. Lin, R. Fan, C. Hou, H. Liu, J. Zhang, Y. Ma, Z. Guo, Bio-gel derived nickel/carbon nanocomposites with enhanced microwave absorption, *J. Mater. Chem. C* 6 (32) (2018) 8812–8822.
- [145] L. Wang, X. Jia, Y. Li, F. Yang, L. Zhang, L. Liu, X. Ren, H. Yang, Synthesis and microwave absorption property of flexible magnetic film based on graphene oxide/carbon nanotubes and Fe₃O₄ nanoparticles, *J. Mater. Chem. A* 2 (36) (2014) 14940–14946.
- [146] M. Cao, R. Qin, C. Qiu, J. Zhu, Matching design and mismatching analysis towards radar absorbing coatings based on conducting plate, *Mater. Des.* 24 (5) (2003) 391–396.
- [147] Y. Zhang, X. Wang, M. Cao, Confinedly implanted NiFe₂O₄-rGO: cluster tailoring and highly tunable electromagnetic properties for selective-frequency microwave absorption, *Nano Res.* 11 (3) (2018) 1426–1436.
- [148] J.-Z. He, X.-X. Wang, Y.-L. Zhang, M.-S. Cao, Small magnetic nanoparticles

- decorating reduced graphene oxides to tune the electromagnetic attenuation capacity, *J. Mater. Chem. C* 4 (29) (2016) 7130–7140.
- [149] X. Li, J. Feng, Y. Du, J. Bai, H. Fan, H. Zhang, Y. Peng, F. Li, One-pot synthesis of CoFe_2O_4 /graphene oxide hybrids and their conversion into FeCo /graphene hybrids for lightweight and highly efficient microwave absorber, *J. Mater. Chem. A* 3 (10) (2015) 5535–5546.
- [150] J. Feng, F. Pu, Z. Li, X. Li, X. Hu, J. Bai, Interfacial interactions and synergistic effect of CoNi nanocrystals and nitrogen-doped graphene in a composite microwave absorber, *Carbon* 104 (2016) 214–225.
- [151] Y. Du, W. Liu, R. Qiang, Y. Wang, X. Han, J. Ma, P. Xu, Shell thickness-dependent microwave absorption of core-shell Fe_3O_4 @C composites, *ACS Appl. Mater. Interfaces* 6 (15) (2014) 12997–13006.
- [152] X. Liu, X. Cui, Y. Chen, X.-J. Zhang, R. Yu, G.-S. Wang, H. Ma, Modulation of electromagnetic wave absorption by carbon shell thickness in carbon encapsulated magnetite nanospindles-poly(vinylidene fluoride) composites, *Carbon* 95 (2015) 870–878.
- [153] Y. Li, J. Wang, R. Liu, X. Zhao, X. Wang, X. Zhang, G. Qin, Dependence of gigahertz microwave absorption on the mass fraction of Co @C nanocapsules in composite, *J. Alloy. Comp.* 724 (2017) 1023–1029.
- [154] Y. Zhan, Z. Long, X. Wan, J. Zhang, S. He, Y. He, 3D carbon fiber mats/nano- Fe_3O_4 hybrid material with high electromagnetic shielding performance, *Appl. Surf. Sci.* 444 (2018) 710–720.
- [155] E. Drakakis, M. Suche, V. Tudose, G. Kenanakis, D. Stratakis, K. Dangakis, A. Miaoudakis, D. Vernardou, E. Koudoumas, Zinc oxide-graphene based composite layers for electromagnetic interference shielding in the GHz frequency range, *Thin Solid Films* 651 (2018) 152–157.
- [156] M.-M. Lu, W.-Q. Cao, H.-L. Shi, X.-Y. Fang, J. Yang, Z.-L. Hou, H.-B. Jin, W.-Z. Wang, J. Yuan, M.-S. Cao, Multi-wall carbon nanotubes decorated with ZnO nanocrystals: mild solution-process synthesis and highly efficient microwave absorption properties at elevated temperature, *J. Mater. Chem. A* 2 (27) (2014) 10540–10547.
- [157] G. Liu, L. Wang, G. Chen, S. Hua, C. Ge, H. Zhang, R. Wu, Enhanced electromagnetic absorption properties of carbon nanotubes and zinc oxide whisker microwave absorber, *J. Alloy. Comp.* 514 (2012) 183–188.
- [158] H. Qin, Q. Liao, G. Zhang, Y. Huang, Y. Zhang, Microwave absorption properties of carbon black and tetrapod-like ZnO whiskers composites, *Appl. Surf. Sci.* 286 (2013) 7–11.
- [159] M. Zong, Y. Huang, H. Wu, Y. Zhao, P. Liu, L. Wang, Facile preparation of $\text{RGO}/\text{Cu}_2\text{O}/\text{Cu}$ composite and its excellent microwave absorption properties, *Mater. Lett.* 109 (2013) 112–115.
- [160] D.-D. Zhang, D.-L. Zhao, J.-M. Zhang, L.-Z. Bai, Microwave absorbing property and complex permittivity and permeability of graphene- CdS nanocomposite, *J. Alloy. Comp.* 589 (2014) 378–383.
- [161] Y. Wang, D. Chen, X. Yin, P. Xu, F. Wu, M. He, Hybrid of MoS_2 and reduced graphene oxide: a lightweight and broadband electromagnetic wave absorber, *ACS Appl. Mater. Interfaces* 7 (47) (2015) 26226–26234.
- [162] X. Ding, Y. Huang, S. Li, N. Zhang, J. Wang, 3D architecture reduced graphene oxide- MoS_2 composite: preparation and excellent electromagnetic wave absorption performance, *Composites, Part A* 90 (2016) 424–432.
- [163] B. Quan, X. Liang, G. Xu, Y. Cheng, Y. Zhang, W. Liu, G. Ji, Y. Du, A permittivity regulating strategy to achieve high-performance electromagnetic wave absorbers with compatibility of impedance matching and energy conservation, *New J. Inside Chem.* 41 (3) (2017) 1259–1266.
- [164] M. Albano, D. Micheli, G. Gradoni, R.B. Morles, M. Marchetti, F. Moglie, V. Mariani Primiani, Electromagnetic shielding of thermal protection system for hypersonic vehicles, *Acta Astronaut.* 87 (2013) 30–39.
- [165] W.-L. Song, C. Gong, H. Li, X.-D. Cheng, M. Chen, X. Yuan, H. Chen, Y. Yang, D. Fang, Graphene-based sandwich structures for frequency selectable electromagnetic shielding, *ACS Appl. Mater. Interfaces* 9 (41) (2017) 36119–36129.
- [166] Y. Wang, X.-D. Cheng, W.-L. Song, C.-J. Ma, X.-M. Bian, M. Chen, Hydro-sensitive sandwich structures for self-tunable smart electromagnetic shielding, *Chem. Eng. J.* 344 (2018) 342–352.
- [167] A.P. Singh, M. Mishra, D.P. Hashim, T.N. Narayanan, M.G. Hahm, P. Kumar, J. Dwivedi, G. Kedawat, A. Gupta, B.P. Singh, A. Chandra, R. Vajtai, S.K. Dhawan, P.M. Ajayan, B.K. Gupta, Probing the engineered sandwich network of vertically aligned carbon nanotube-reduced graphene oxide composites for high performance electromagnetic interference shielding applications, *Carbon* 85 (2015) 79–88.
- [168] W.-L. Song, M.-S. Cao, M.-M. Lu, S. Bi, C.-Y. Wang, J. Liu, J. Yuan, L.-Z. Fan, Flexible graphene/polymer composite films in sandwich structures for effective electromagnetic interference shielding, *Carbon* 66 (2014) 67–76.
- [169] W.-L. Song, L.-Z. Fan, M.-S. Cao, M.-M. Lu, C.-Y. Wang, J. Wang, T.-T. Chen, Y. Li, Z.-L. Hou, J. Liu, Y.-P. Sun, Facile fabrication of ultrathin graphene papers for effective electromagnetic shielding, *J. Mater. Chem. C* 2 (25) (2014) 5057–5064.
- [170] T. Zhao, W. Jin, X. Ji, H. Yan, Y. Jiang, Y. Dong, Y. Yang, A. Dang, H. Li, T. Li, S. Shang, Z. Zhou, Synthesis of sandwich microstructured expanded graphite/barium ferrite connected with carbon nanotube composite and its electromagnetic wave absorbing properties, *J. Alloy. Comp.* 712 (2017) 59–68.
- [171] X. Ding, Y. Huang, S. Li, N. Zhang, J. Wang, FeNi_3 nanoalloy decorated on 3D architecture composite of reduced graphene oxide/molybdenum disulfide giving excellent electromagnetic wave absorption properties, *J. Alloy. Comp.* 689 (2016) 208–217.
- [172] Y. Wang, W. Zhang, X. Wu, C. Luo, T. Liang, G. Yan, Metal-organic framework nanoparticles decorated with graphene: a high-performance electromagnetic wave absorber, *J. Magn. Magn. Mater.* 416 (2016) 226–230.
- [173] J. Yuan, Q. Liu, S. Li, Y. Lu, S. Jin, K. Li, H. Chen, H. Zhang, Metal organic framework (MOF)-derived carbonaceous Co_3O_4 /Co microframes anchored on RGO with enhanced electromagnetic wave absorption performances, *Synth. Met.* 228 (2017) 32–40.
- [174] Y. Zhan, J. Wang, K. Zhang, Y. Li, Y. Meng, N. Yan, W. Wei, F. Peng, H. Xia, Fabrication of a flexible electromagnetic interference shielding Fe_3O_4 @reduced graphene oxide/natural rubber composite with segregated network, *Chem. Eng. J.* 344 (2018) 184–193.
- [175] D. Lu, Z. Mo, B. Liang, L. Yang, Z. He, H. Zhu, Z. Tang, X. Gui, Flexible, lightweight carbon nanotube sponges and composites for high-performance electromagnetic interference shielding, *Carbon* 133 (2018) 457–463.
- [176] J. Liu, H.-B. Zhang, Y. Liu, Q. Wang, Z. Liu, Y.-W. Mai, Z.-Z. Yu, Magnetic, electrically conductive and lightweight graphene/iron pentacarbonyl porous films enhanced with chitosan for highly efficient broadband electromagnetic interference shielding, *Compos. Sci. Technol.* 151 (2017) 71–78.
- [177] Y.-J. Wan, P.-L. Zhu, S.-H. Yu, R. Sun, C.-P. Wong, W.-H. Liao, Ultralight, super-elastic and volume-preserving cellulose fiber/graphene aerogel for high-performance electromagnetic interference shielding, *Carbon* 115 (2017) 629–639.
- [178] H. Yang, Z. Yu, P. Wu, H. Zou, P. Liu, Electromagnetic interference shielding effectiveness of microcellular polyimide/in situ thermally reduced graphene oxide/carbon nanotubes nanocomposites, *Appl. Surf. Sci.* 434 (2018) 318–325.
- [179] D. Baokang, C. Yipeng, Y. Ning, C. Bo, S. Qingfeng, Effect of carbon fiber acrylation on the electromagnetic shielding properties of carbon fiber/polyacrylamide/wood based fiberboards, *Nanotechnology* 29 (19) (2018) 195605.
- [180] R. Dou, Y. Shao, S. Li, B. Yin, M. Yang, Structuring tri-continuous structure multiphase composites with ultralow conductive percolation threshold and excellent electromagnetic shielding effectiveness using simple melt mixing, *Polymers* 83 (2016) 34–39.
- [181] S. Ashwani Kumar, K. Ajit, H. Krishna Kamal, G. Vinay, S. Kedar, Lightweight reduced graphene oxide- Fe_3O_4 nanoparticle composite in the quest for an excellent electromagnetic interference shielding material, *Nanotechnology* 29 (24) (2018) 245203.
- [182] W.-L. Song, X.-T. Guan, L.-Z. Fan, W.-Q. Cao, C.-Y. Wang, M.-S. Cao, Tuning three-dimensional textures with graphene aerogels for ultra-light flexible graphene/texture composites of effective electromagnetic shielding, *Carbon* 93 (2015) 151–160.
- [183] T.K. Gupta, B.P. Singh, S.R. Dhakate, V.N. Singh, R.B. Mathur, Improved nanoindentation and microwave shielding properties of modified MWCNT reinforced polyurethane composites, *J. Mater. Chem. A* 1 (32) (2013) 9138–9149.
- [184] M. Mishra, A.P. Singh, B.P. Singh, V.N. Singh, S.K. Dhawan, Conducting ferrofluid: a high-performance microwave shielding material, *J. Mater. Chem. A* 2 (32) (2014) 13159–13168.
- [185] K. Singh, A. Ohlan, V.H. Pham, B.R.S. Varshney, J. Jang, S.H. Hur, W.M. Choi, M. Kumar, S.K. Dhawan, B.-S. Kong, J.S. Chung, Nanostructured graphene/ Fe_3O_4 incorporated polyaniline as a high performance shield against electromagnetic pollution, *Nanoscale* 5 (6) (2013) 2411–2420.
- [186] P. Verma, P. Saini, R.S. Malik, V. Choudhary, Excellent electromagnetic interference shielding and mechanical properties of high loading carbon-nanotubes/polymer composites designed using melt recirculation equipped twin-screw extruder, *Carbon* 89 (2015) 308–317.
- [187] S.P. Pawar, S. Stephen, S. Bose, V. Mittal, Tailored electrical conductivity, electromagnetic shielding and thermal transport in polymeric blends with graphene sheets decorated with nickel nanoparticles, *Phys. Chem. Chem. Phys.* 17 (22) (2015) 14922–14930.
- [188] W. Jiacheng, X. Changshu, L. Qian, P. Yubai, G. Jingkun, Ordered mesoporous carbon/fused silica composites, *Adv. Funct. Mater.* 18 (19) (2008) 2995–3002.
- [189] Y. Lan, X. Li, Y. Zong, Z. Li, Y. Sun, G. Tan, J. Feng, Z. Ren, X. Zheng, In-situ synthesis of carbon nanotubes decorated by magnetite nanoclusters and their applications as highly efficient and enhanced microwave absorber, *Ceram. Int.* 42 (16) (2016) 19110–19118.
- [190] Y. Wang, Y. Chen, X. Wu, W. Zhang, C. Luo, J. Li, Fabrication of MoS_2 -graphene modified with Fe_3O_4 particles and its enhanced microwave absorption performance, *Adv. Powder Technol.* 29 (3) (2018) 744–750.
- [191] W. Zhang, X. Zhang, Y. Qiao, H. Yan, S. Qi, Covalently bonded GNPs-NH-PANI nanorod arrays modified by Fe_3O_4 nanoparticles as high-performance electromagnetic wave absorption materials, *Mater. Lett.* 216 (2018) 101–105.
- [192] D. Sun, Q. Zou, Y. Wang, Y. Wang, W. Jiang, F. Li, Controllable synthesis of porous Fe_3O_4 @ ZnO sphere decorated graphene for extraordinary electromagnetic wave absorption, *Nanoscale* 6 (12) (2014) 6557–6562.
- [193] C.-I. Hou, T.-h. Li, T.-k. Zhao, H.-g. Liu, L.-h. Liu, W.-j. Zhang, Electromagnetic wave absorbing properties of multi-wall carbon nanotube/ Fe_3O_4 hybrid materials, *N. Carbon Mater.* 28 (3) (2013) 184–190.
- [194] R. Qiang, Y. Du, Y. Wang, N. Wang, C. Tian, J. Ma, P. Xu, X. Han, Rational design of yolk-shell C@C microspheres for the effective enhancement in microwave absorption, *Carbon* 98 (2016) 599–606.
- [195] Z. Li, X. Li, Y. Zong, G. Tan, Y. Sun, Y. Lan, M. He, Z. Ren, X. Zheng, Solvothermal synthesis of nitrogen-doped graphene decorated by superparamagnetic Fe_3O_4 nanoparticles and their applications as enhanced synergistic microwave absorbers, *Carbon* 115 (2017) 493–502.

- [196] P. Liu, Y. Huang, X. Zhang, Superparamagnetic Fe₃O₄ nanoparticles on graphene-polyaniline: synthesis, characterization and their excellent electromagnetic absorption properties, *J. Alloy. Comp.* 596 (2014) 25–31.
- [197] P. Liu, Y. Huang, L. Wang, M. Zong, W. Zhang, Hydrothermal synthesis of reduced graphene oxide-Co₃O₄ composites and the excellent microwave electromagnetic properties, *Mater. Lett.* 107 (2013) 166–169.
- [198] M. Zong, Y. Huang, N. Zhang, Reduced graphene oxide-Ni_{0.5}Zn_{0.5}Fe₂O₄ composite: synthesis and electromagnetic absorption properties, *Mater. Lett.* 145 (2015) 115–119.
- [199] Z. Yang, Y. Wan, G. Xiong, D. Li, Q. Li, C. Ma, R. Guo, H. Luo, Facile synthesis of ZnFe₂O₄/reduced graphene oxide nanohybrids for enhanced microwave absorption properties, *Mater. Res. Bull.* 61 (2015) 292–297.
- [200] Y. Wang, X. Wu, W. Zhang, S. Huang, Facile synthesis of Ni/PANI/RGO composites and their excellent electromagnetic wave absorption properties, *Synth. Met.* 210 (2015) 165–170.
- [201] P. Liu, Y. Huang, L. Wang, W. Zhang, Preparation and excellent microwave absorption property of three component nanocomposites: polyaniline-reduced graphene oxide-Co₃O₄ nanoparticles, *Synth. Met.* 177 (2013) 89–93.
- [202] P. Liu, Y. Huang, L. Wang, W. Zhang, Synthesis and excellent electromagnetic absorption properties of polypyrrole-reduced graphene oxide-Co₃O₄ nanocomposites, *J. Alloy. Comp.* 573 (2013) 151–156.
- [203] Y. Wang, Y. Huang, J. Ding, Synthesis and enhanced electromagnetic absorption properties of polypyrrole-BaFe₁₂O₁₉/Ni_{0.8}Zn_{0.2}Fe₂O₄ on graphene nanosheet, *Synth. Met.* 196 (2014) 125–130.
- [204] Y. Wang, Y. Huang, Q. Wang, M. Zong, Preparation and electromagnetic properties of graphene-supported Ni_{0.8}Zn_{0.2}Ce_{0.06}Fe_{1.94}O₄ nanocomposite, *Powder Technol.* 249 (2013) 304–308.
- [205] X. Ding, Y. Huang, J. Wang, H. Wu, P. Liu, Excellent electromagnetic wave absorption property of quaternary composites consisting of reduced graphene oxide, polyaniline and FeNi₃@SiO₂ nanoparticles, *Appl. Surf. Sci.* 357 (2015) 908–914.
- [206] Y. Wang, W. Zhang, C. Luo, X. Wu, G. Yan, Superparamagnetic FeCo@SnO₂ nanoparticles on graphene-polyaniline: synthesis and enhanced electromagnetic wave absorption properties, *Ceram. Int.* 42 (10) (2016) 12496–12502.
- [207] K. Zhang, X. Gao, Q. Zhang, T. Li, H. Chen, X. Chen, Preparation and microwave absorption properties of asphalt carbon coated reduced graphene oxide/magnetic CoFe₂O₄ hollow particles modified multi-wall carbon nanotube composites, *J. Alloy. Comp.* 723 (2017) 912–921.
- [208] L. Wang, Y. Huang, C. Li, J. Chen, X. Sun, Hierarchical composites of polyaniline nanorod arrays covalently-grafted on the surfaces of graphene@Fe₃O₄@C with high microwave absorption performance, *Compos. Sci. Technol.* 108 (2015) 1–8.
- [209] L. Wang, Y. Huang, H. Huang, N-doped graphene@polyaniline nanorod arrays hierarchical structures: synthesis and enhanced electromagnetic absorption properties, *Mater. Lett.* 124 (2014) 89–92.
- [210] H. Zhang, M. Hong, P. Chen, A. Xie, Y. Shen, 3D and ternary rGO/MCNTs/Fe₃O₄ composite hydrogels: synthesis, characterization and their electromagnetic wave absorption properties, *J. Alloy. Comp.* 665 (2016) 381–387.
- [211] P. Liu, Y. Huang, Y. Yang, J. Yan, X. Zhang, Sandwich structures of graphene@Fe₃O₄@PANI decorated with TiO₂ nanosheets for enhanced electromagnetic wave absorption properties, *J. Alloy. Comp.* 662 (2016) 63–68.
- [212] Y. Wang, X. Wu, W. Zhang, C. Luo, J. Li, Synthesis of ferromagnetic sandwich FeCo@graphene@PPy and enhanced electromagnetic wave absorption properties, *J. Magn. Magn. Mater.* 443 (2017) 358–365.
- [213] W. Feng, Y. Wang, J. Chen, L. Wang, L. Guo, J. Ouyang, D. Jia, Y. Zhou, Reduced graphene oxide decorated with in-situ growing ZnO nanocrystals: facile synthesis and enhanced microwave absorption properties, *Carbon* 108 (2016) 52–60.
- [214] L. Shi, Y. Zhao, Y. Li, X. Han, T. Zhang, Octahedron Fe₃O₄ particles supported on 3D MWCNT/graphene foam: in-situ method and application as a comprehensive microwave absorption material, *Appl. Surf. Sci.* 416 (2017) 329–337.
- [215] C. Wang, T. Xu, C.-A. Wang, Microwave absorption properties of C/(CoFe) hierarchical core-shell spheres synthesized by using colloidal carbon spheres as templates, *Ceram. Int.* 42 (7) (2016) 9178–9182.
- [216] P.M. Sudeep, S. Vinayasee, P. Mohanan, P.M. Ajayan, T.N. Narayanan, M.R. Anantharaman, Fluorinated graphene oxide for enhanced S and X-band microwave absorption, *Appl. Phys. Lett.* 106 (22) (2015) 221603.
- [217] Z. Su, J. Tao, J. Xiang, Y. Zhang, C. Su, F. Wen, Structure evolution and microwave absorption properties of nickel nanoparticles incorporated carbon spheres, *Mater. Res. Bull.* 84 (2016) 445–448.
- [218] M. Zong, Y. Huang, N. Zhang, Reduced graphene oxide-Ni_{0.5}Zn_{0.5}Fe₂O₄ composite: synthesis and electromagnetic absorption properties, *Mater. Lett.* 145 (2015) 115–119.
- [219] X. Wang, B. Li, Y. Zhang, X. Lv, G. Gu, Synthesis of flake shaped carbonyl iron/reduced graphene oxide/polyvinyl pyrrolidone ternary nanocomposites and their microwave absorbing properties, *J. Alloy. Comp.* 695 (2017) 508–519.
- [220] Y. Xu, J. Luo, W. Yao, J. Xu, T. Li, Preparation of reduced graphene oxide/flake carbonyl iron powders/polyaniline composites and their enhanced microwave absorption properties, *J. Alloy. Comp.* 636 (2015) 310–316.
- [221] P. Liu, Y. Huang, X. Zhang, Preparation and excellent microwave absorption properties of ferromagnetic graphene/poly(3, 4-ethylenedioxythiophene)/CoFe₂O₄ nanocomposites, *Powder Technol.* 276 (2015) 112–117.
- [222] F. Wu, A. Xie, M. Sun, Y. Wang, M. Wang, Reduced graphene oxide (RGO) modified spongelike polypyrrole (PPy) aerogel for excellent electromagnetic absorption, *J. Mater. Chem. A* 3 (27) (2015) 14358–14369.
- [223] C. Song, X. Yin, M. Han, X. Li, Z. Hou, L. Zhang, L. Cheng, Three-dimensional reduced graphene oxide foam modified with ZnO nanowires for enhanced microwave absorption properties, *Carbon* 116 (2017) 50–58.
- [224] Y. Wang, H. Guan, S. Du, Y. Wang, A facile hydrothermal synthesis of MnO₂ nanorod-reduced graphene oxide nanocomposites possessing excellent microwave absorption properties, *RSC Adv.* 5 (108) (2015) 88979–88988.
- [225] R.-B. Yang, P.M. Reddy, C.-J. Chang, P.-A. Chen, J.-K. Chen, C.-C. Chang, Synthesis and characterization of Fe₃O₄/polypyrrole/carbon nanotube composites with tunable microwave absorption properties: role of carbon nanotube and polypyrrole content, *Chem. Eng. J.* 285 (2016) 497–507.
- [226] J. Luo, Y. Xu, W. Yao, C. Jiang, J. Xu, Synthesis and microwave absorption properties of reduced graphene oxide-magnetic porous nanospheres-polyaniline composites, *Compos. Sci. Technol.* 117 (2015) 315–321.
- [227] P. Liu, Y. Huang, X. Zhang, Cubic NiFe₂O₄ particles on graphene-polyaniline and their enhanced microwave absorption properties, *Compos. Sci. Technol.* 107 (2015) 54–60.
- [228] P. Liu, Y. Huang, X. Zhang, Synthesis, characterization and excellent electromagnetic wave absorption properties of graphene@CoFe₂O₄@polyaniline nanocomposites, *Synth. Met.* 201 (2015) 76–81.
- [229] C. Zhu, S. Zhang, Y. Sun, Y. Chen, Incorporation of Co@Co yolk-shell nanoparticles and ZnO nanoparticles with graphene sheets as lightweight and high-performance electromagnetic wave absorbing material, *J. Alloy. Comp.* 711 (2017) 552–559.
- [230] J. Wu, Z. Ye, W. Liu, Z. Liu, J. Chen, The effect of GO loading on electromagnetic wave absorption properties of Fe₃O₄/reduced graphene oxide hybrids, *Ceram. Int.* 43 (16) (2017) 13146–13153.
- [231] G. Liu, W. Jiang, D. Sun, Y. Wang, F. Li, One-pot synthesis of urchinlike Ni nanoparticles/RGO composites with extraordinary electromagnetic absorption properties, *Appl. Surf. Sci.* 314 (2014) 523–529.
- [232] G. Wang, Z. Gao, G. Wan, S. Lin, P. Yang, Y. Qin, High densities of magnetic nanoparticles supported on graphene fabricated by atomic layer deposition and their use as efficient synergistic microwave absorbers, *Nano Res.* 7 (5) (2014) 704–716.
- [233] X.F. Zhang, X.L. Dong, H. Huang, et al., Microwave absorption properties of the carbon-coated nickel nanocapsules, *Appl. Phys. Lett.* 89 (5) (2006) 053115.
- [234] L. Zhu, X. Zeng, M. Chen, R. Yu, Controllable permittivity in 3D Fe₃O₄/CNTs network for remarkable microwave absorption performances, *RSC Adv.* 7 (43) (2017) 26801–26808.
- [235] L. Zhang, X. Zhang, G. Zhang, Z. Zhang, S. Liu, P. Li, Q. Liao, Y. Zhao, Y. Zhang, Investigation on the optimization, design and microwave absorption properties of reduced graphene oxide/tetrapod-like ZnO composites, *RSC Adv.* 5 (14) (2015) 10197–10203.
- [236] Z. Zhao, P. Bai¹, R. Guan, V. Murugadoss, H. Liu, X. Wang, Z. Guo, Microstructural evolution and mechanical strengthening mechanism of Mg-35Sn-1Mn-1La alloy after heat treatments, *Mater. Sci. Eng. A* 734 (2018) 200–209.
- [237] Z. Sun, et al., Experimental and simulation understanding of morphology controlled barium titanate nanoparticles under co-adsorption of surfactants, *CrystEngComm* 19 (2017) 3288–3298.
- [238] L. Zhang, W. Yu, C. Han, J. Guo, Q. Zhang, H. Xie, Q. Shao, Z. Sun, Z. Guo, Large scaled synthesis of heterostructured electrospun TiO₂/SnO₂ nanofibers with an enhanced photocatalytic activity, *J. Electrochem. Soc.* 164 (2017) H651–H656.
- [239] L. Zhang, M. Qin, W. Yu, et al., Heterostructured TiO₂/WO₃ nanocomposites for photocatalytic degradation of toluene under visible light, *J. Electrochem. Soc.* 164 (2017) H1086–H1090.
- [240] T. Su, Q. Shao, Z. Qin, Z. Guo, Z. Wu, Role of interfaces in two-dimensional photocatalyst for water splitting, *ACS Catal.* 8 (2018) 2253–2276.
- [241] Z. Zhao, R. Guan, J. Zhang, Z. Zhao, P. Bai, Effects of process parameters of semisolid stirring on microstructure of Mg-35Sn-1Mn-3SiC (wt%) strip processed by rheo-rolling, *Acta Metall. Sin. (Engl. Lett.)* 30 (2017) 66–72.
- [242] F. Liu, Z. Xu, Z. Wang, et al., Structures and mechanical properties of Nb-Mo-Co(Ru) solid solutions for hydrogen permeation, *J. Alloy. Comp.* 756 (2018) 26–32.
- [243] Y. Zhao, S. Deng, H. Liu, et al., First-principle investigation of pressure and temperature influence on structural, mechanical and thermodynamic properties of Ti₃AC₂ (A=Al and Si), *Comput. Mater. Sci.* 154 (2018) 365–370.
- [244] W. Deng, T. Kang, H. Liu, et al., Potassium hydroxide activated and nitrogen doped graphene with enhanced supercapacitive behavior, *Sci. Adv. Mater.* 10 (2018) 937–949.
- [245] Y. Zhang, L. Qian, W. Zhao, et al., Highly efficient Fe-N-C nanoparticles modified porous graphene composites for oxygen reduction reaction, *J. Electrochem. Soc.* 165 (2018) H510–H516.
- [246] Q. Hou, J. Ren, H. Chen, et al., Synergistic hematite-fullerene electron extracting layers for improved efficiency and stability in perovskite solar cells, *ChemElectroChem* 5 (2018) 726–731.
- [247] X. Lou, C. Lin, Q. Luo, et al., Crystal-structure modification enhanced FeNb₁₀O₂₉ anodes for lithium-ion batteries, *ChemElectroChem* 4 (2017) 3171–3180.
- [248] C. Wang, M. Zhao, J. Li, et al., Silver nanoparticles/graphene oxide decorated carbon fiber synergistic reinforcement in epoxy-based composites, *Polymer* 131 (2017) 263–271.

- [249] J. Zhao, L. Wu, C. Zhan, Q. Shao, Z. Guo, L. Zhang, Overview of polymer nanocomposites: computer simulation understanding of physical properties, *Polymer* 133 (2017) 272–287.
- [250] Z. Hu, D. Zhang, F. Lu, et al., Multistimuli-responsive intrinsic self-healing epoxy resin constructed by host–guest interactions, *Macromolecules* 51 (2018) 5294–5303.
- [251] Y. Zhang, M. Zhao, J. Zhang, Q. Shao, J. Li, H. Li, B. Lin, M. Yu, S. Chen, Z. Guo, Excellent corrosion protection performance of epoxy composite coatings filled with silane functionalized silicon nitride, *J. Polym. Res.* 25 (2018) 130.
- [252] Y. Wang, P. Zhou, S. Luo, et al., Controllable synthesis of monolayer poly(-acrylic acid) on channel surface of mesoporous alumina for Pb(II) adsorption, *Langmuir* 34 (2018) 7859–7868.
- [253] K. Gong, Q. Hu1, L. Yao, et al., Ultrasonic pretreated sludge derived stable magnetic active carbon for Cr(VI) removal from wastewater, *ACS Sustain. Chem. Eng.* 6 (2018) 7283–7291.
- [254] J. Huang, Y. Cao, Q. Shao, X. Peng, Z. Guo, Magnetic nanocarbon adsorbents with enhanced hexavalent chromium removal: morphology dependence of fibrillar vs particulate structures, *Ind. Eng. Chem. Res.* 56 (2017) 10689–10701.
- [255] Z. Yang, X. Hao, S. Chen, et al., Long-term antibacterial stable reduced graphene oxide nanocomposites loaded with cuprous oxide Nanoparticles, *J. Colloid Interface Sci.* 533 (2018) 13–23.
- [256] J. Tian, Q. Shao, X. Dong, et al., Bio-template synthesized NiO/C hollow microspheres with enhanced Li-ion battery electrochemical performance, *Electrochim. Acta* 261 (2018) 236–245.